DEVELOPMENT OF NANOPOROUS ANODIC ALUMINA TECHNOLOGIES FOR DRUG DELIVERY

Maria Porta Batalla

UNIVERSITAT ROVIRA i VIRGILI

Development of Nanoporous Anodic Alumina Technologies for Drug Delivery

Maria Porta i Batalla

DOCTORAL THESIS
2017

UNIVERSITAT ROVIRA I VIRGILI
DEVELOPMENT OF NANOPOROUS ANODIC ALUMINA TECHNOLOGIES FOR DRUG DELIVERY
Maria Porta Batalla

UNIVERSITAT ROVIRA I VIRGILI
DEVELOPMENT OF NANOPOROUS ANODIC ALUMINA TECHNOLOGIES FOR DRUG DELIVERY
Maria Porta Batalla

UNIVERSITAT ROVIRA I VIRGILI
DEVELOPMENT OF NANOPOROUS ANODIC ALUMINA TECHNOLOGIES FOR DRUG DELIVERY
Maria Porta Batalla

Maria Porta i Batalla

Development of Nanoporous Anodic Alumina Technologies for Drug Delivery

Ph. D. Thesis

Supervised by

Dr. Lluís Francesc Marsal Garví

Department of Electronic, Electrical and Automatic Control Engineering

Nano-Electronic and Photonic Systems (NePhoS)

UNIVERSITAT ROVIRA I VIRGILI

Tarragona

2017

UNIVERSITAT ROVIRA I VIRGILI
DEVELOPMENT OF NANOPOROUS ANODIC ALUMINA TECHNOLOGIES FOR DRUG DELIVERY
Maria Porta Batalla

UNIVERSITAT ROVIRA I VIRGILI

Departament d'Enginyeria Electrònica, Elèctrica i Automàtica
Escola Tècnica Superior D'Enginyeria
Campus Sescelades
Avinguda dels Països Catalans, 26
43007 Tarragona
Espanya
Tel.: + 34 977 559 610 / 559 728
Fax: + 34 977 559 605

I, Lluís Francesc Marsal Garví, full professor of the Departament of Electronic, Electrical and Automatic Control Engineering of the Universitat Rovira i Virgili,

CERTIFY:

That the present study, entitled "Development of Nanoporous Anodic Alumina Technologies for Drug Delivery", presented by Maria Porta Batalla for the award of the degree of Doctor, has been carried out under our supervision at the Department of Electronic, Electrical and Automatic Control Engineering of this university, and that it fulfils all the requirements to be eligible for the International Doctorate Award.

Tarragona, 2nd July 2017

Doctoral Thesis Supervisor

Lluís Francesc Marsal Garví

UNIVERSITAT ROVIRA I VIRGILI
DEVELOPMENT OF NANOPOROUS ANODIC ALUMINA TECHNOLOGIES FOR DRUG DELIVERY
Maria Porta Batalla

Acknowledgements

This Ph.D. thesis would have never been possible without the collaboration and support of a number of people that have helped me over the course of this trip. Hereby, I would like to acknowledge and thank all of them.

First I would like to express my gratitude an appreciation to my supervisor, Prof. Lluís Marsal, for his support, and guidance throughout this work, and for providing me the opportunity to complete my Ph.D. thesis.

I am particularly grateful for the assistance given by Dr. Josep Ferré-Borrull for his encouragement, valuable advice, corrections and moral support.

To my past colleagues and exmembers of Nephos group: Dr. Peilin Han, Dr. Maria Alba, Dr. Víctor Samuel Valderrama, Dr. Pedro Granero, Dr. Agustín Mihi, Dr. Edith Osorio and an special thanks to Agatha Slota and Dr. Gerard Macias for instructing me into the nanoporous anodic alumina world.

I would like to thank the present colleagues and former members of the Nephos group: Dr. Aurelien Viterisi, Dr. Pilar Formentín, and particularly to Dr. Elisabet Xifré for the support and collaboration.

Acknowledgements

To my contemporary Ph.D. students: José Guadalupe Sánchez for being an example of constancy, Caterina Stenta for her kindness and spreadable good mood, Francesc Bertó for his contagious enthusiasm and motivation, and Chris Eckstein for the help, encouragement and english corrections. Also thanks to Laura Pol and Karen Acosta, although they have only been present in the very last months of my Ph.D., they have boost the writing process with fresh air.

To the people of the Servei de Recursos Científics i Tècnics (SRCiT): Dr. Mercé Montcusí, Dr. Mariana Stankova, Dr. Rita Marimón and Dr. Lukas Vojkuvka, for the assistance and teaching in numerous characterization sessions.

I am also grateful to Prof. Michael Sailor for offering me the opportunity to work and learn in his research group in the UCSD, for his master classes in the Summer School for Silicon Nanothecnology, and for his kindness and hospitality. I must also thank all the members of Sailor Research Group, especially to Dr. Tushar Kurmeria, Joanna Wang and B.J. Kim for their patience teaching me and for general assistance during my stage. And I am also grateful to my contemporary visitors in the Summer School, especially to Dr. Giovanni Polito, Pedro Perdigón and Paul Clarkson to make my stay in San Diego such an enjoyable experience.

I would also like to thank all the people who have been part of the "VIP lunch group": Elena, Luís, Vero, Míriam, Alejandro, François, Pili and especially to Dr. Carlos Olalla and Dr. Mª Carmen Portillo for all the good moments shared, for the comprehension they showed and for the courage they beam.

Finally I would like to express my gratitude to my family for being by my side, and to Xavier for believing in me more than what I do and for being my main support and cloth of tears during this Ph.D.

UNIVERSITAT ROVIRA I VIRGILI
DEVELOPMENT OF NANOPOROUS ANODIC ALUMINA TECHNOLOGIES FOR DRUG DELIVERY
Maria Porta Batalla

List of Abbreviations

3D – Three Dimensional

AL – Aluminum

AL_2O_3 – Aluminum Oxide

DDS - Drug Delivery System

D_{int} – Interpore Distance

DOX – Doxorubicin Hydrochloride

D_p – Pore Diameter

EG – Ethylenglycol

EPR – Enhanced Permeation and retention

ESEM – Environmental Scaning Electron Microscope

FDA – Food and Drug Administration

GRAS – Generally Recognized as Safe

HA – Hard Anodization

$H_2C_2O_4$ – Oxalic Acid

H_2SO_4 – Sulphuric Acid

H_3PO_4 – Phosphoric Acid

HF – Hydrofluoric Acid

HMSN – Hollow Mesoporous Silica Nanoparticles

IF – Inverted Funnel

IUPAC – International Union of Pure and Applied Chemistry

J – Current Dendity

Ja – Anion Current Density

Jc – Cation Current Density

Je – Electron Current Density

L – Layer Thickness

LIL – Laser Interference Lithography

MSN – Mesoporous Silica Nanoparticles

NA – Mild Anodization

NAA – Nanoporous Anodic Alumina

NF – Normal Funnel

NIL – Nanoimprint Lithography

P – Porosity

PEG – Polyethilenglycol

Q – Total Current Charge

Rp – Pore Growth Rate

SDA – Structure Directing Agent

SiO2 – Silicon Dioxide

T – Temperature

t – Time

T_b – Barrier Layer Thickness

TEA - Triethanolamine

TEM – Transmission Electron Microscopy

TEOS – Tetraethoxysilane

TTAB – Tetradecyltrimethyl-ammonium

T_w – Pore wall Thickness

U – Anodization Voltage

ρ_p – Pore Density

υ–Viscosity

List of Figures

UNIVERSITAT ROVIRA I VIRGILI
DEVELOPMENT OF NANOPOROUS ANODIC ALUMINA TECHNOLOGIES FOR DRUG DELIVERY
Maria Porta Batalla

List of Tables

“Live as if you were to die tomorrow.
Learn as if you were to live forever. “

- Mahatma Gandhi -

UNIVERSITAT ROVIRA I VIRGILI
DEVELOPMENT OF NANOPOROUS ANODIC ALUMINA TECHNOLOGIES FOR DRUG DELIVERY
Maria Porta Batalla

Contents

Chapter 1

Introduction

UNIVERSITAT ROVIRA I VIRGILI
DEVELOPMENT OF NANOPOROUS ANODIC ALUMINA TECHNOLOGIES FOR DRUG DELIVERY
Maria Porta Batalla

Drug Delivery Systems (DDS) are engineered technologies for the targeted delivery and controlled release of therapeutic agents. This way DDS can control the rate and location in where the drug is released in the body in order to avoid side effects.

In this chapter a general introduction to drug delivery systems will be presented. Historical approaches to drug delivery using different administration routes are explained with the goal of guiding the reader across the nanotechnology possibilities, and more concretely to nanotechnology applied to drug delivery systems.

1.1. Motivation and Background

Tracing the evolution of controlled drug delivery, we can see that it had its origins in the 1960s when numerous macroscopic "controlled" drug delivery devices and implants were designed for delivery as mucosal inserts (in the eye), as implants (sub-cutaneous or intramuscular), as ingestible capsules (using the gastrointestinal tract), as topical patches (on the skin), and were approved for clinical use. In 1980s the microscopic degradable polymer era started and nowadays we are immersed in the very active and exiting nanoscopic era [1].

The latest growth of scientific methods for structuring materials at the nanoscale has attracted much interest in the scientific community. The capability to transform matter at the nanometer level has unlocked the chance to develop and study materials that, due to their nanostructural features, display new and exotic effects [2]. Biomaterials are being increasingly required for a huge variety of applications. They can be used for short time purposes such as surgical operations, or implanted for days to decades in long-term applications. In the pharmaceutical industry there is also a raising interest in developing drug delivery systems that are efficient for treatments of multiple diseases with minor side effects. To be able to understand correctly how drug administration is working it is needed to comprehend the procedures that are leading the evolution of the drugs in the body after being administered under determinate conditions and using an specific administration route [3].

First we are exposing the different administration routes that can be used with their advantages and drawbacks. One method of classifying the administration routes is first discerning between **enteral** and **parenteral** [4]. The enteral routes are those ones that involve the gastrointestinal tract and have a systemic effect. Includes: oral, buccal, sublingual, rectal… Parenteral means not enteral and includes any route that is not using oral or rectal intake. The parenteral routes are injections that includes subcutaneous, intramuscular, intravenous or intraperitoneal and can also include topical intake and inhalation [5].

We can also differentiate the intravenous route from the others, as it is the only one in which any body membrane should be crossed to achieve the blood circulation. Consequently any absorption process is not involved.

There are five different processes or stages that the drug has to pass through [6]. The acronym LADME is formed by the initials of this five stages that are usually characterizing the temporal and spatial evolution of a drug after being administered to an organism in a determined conditions and specific administration route. Those stages are: Liberation (Drug release), Absorption, Distribution, Metabolism and Excretion. In this work we are going to focus the studies in the first stage: liberation, since we are doing in vitro studies and we are interested on the release differences using diverse materials and singular structures [7].

The new drug administration systems are hunting the objective of making the drug reach a concrete part of the body in a desired velocity. It is also needed to keep the right concentration for a desired time in the right site. This site can be inside a tissue (intratisular), it can even be inside a cell (intracellular), or it can be outside a tissue (extratisular) like the intestinal lumen.

We can distinguish between two drug delivery possibilities: The ones that control the drug release in terms of velocity, and the ones that facilitate the distribution in a concrete area of the organism.

The systems that control the release has a fundamental objective to improve the drug administration, reducing side effects and extending the therapeutic effect maintaining the plasmatic concentrations in the organism between the maximum safe and the minimum effective. It is possible to maintain the drug concentration between those two limits for a long period of time with one only dose using controlled release systems. In this work we are going to focus most of our efforts in this type of controlled release system.

The other option is vectorization, that means that the drug will be distributed specifically in the organ or area where it should act, maintaining it isolated from the rest of the organism. This option is related with the distribution stage. It has to be taken into account that to be able to accomplish its action, drugs have to pass through several membranes and hostile environments, some times it develops on inefficient molecules or toxicity. Those vectors have improved this trip

inside the organism due to protection of the effective molecule (encapsulation) using carriers and by the increased affinity for the target tissues. This increased affinity can be achieved using active targeting by conjugating cell membrane receptor antibodies, peptides or small molecule cell ligands to the carrier, or passive targeting, in the case of cancer, using the enhanced permeation and retention effect (EPR) [8, 9]. The EPR effect was discovered by Hiroshi Maeda [10]. In this effect nano-scale carriers are entrapped within solid tumors due to leaky vasculature of the fast-growing tumor. As tumors grow and begin to outstrip the available supply of oxygen and nutrients, they release cytokines and other signaling molecules that recruit new blood vessels to the tumor, in a process called angiogenesis. Angiogenic blood vessels, unlike the tight blood vessels in most normal tissues, have gaps as large as 600 to 800 nm between adjacent endothelial cells. Carriers can extravasate though these gaps into the tumor interstitial space, in a size-dependent manner. Because tumors have weakened lymphatic drainage, the carriers (drug formulation) can concentrate in the tumor, and large increases of drug concentrations can be achieved relative to administration of the same dose of free drug [11, 12].

It is also important to mention that nanotechnology has driven the development of Nanosystems that are able to circulate easily all over the body. Some of them can act in smart way, being stimully-responsive systems [13–15]. They can react to the environment signals like pH, temperature, radiofrequency or other indicators.

In sum, using this systems we can improve the drug usage in several ways: pharmacokinetic aspects (protecting the drug from the

presystemic and systemic degradation, metabolization or unnecessary elimination, selective and massive release of the drug, absorption velocity control, obtaining sustained and therapeutic plasmatic and tissular levels, selective distribution), pharmacodynamics (dose decrease, constant tissular levels), therapeutic (better control of the dosage in narrow therapeutic range, less side effects) and others related to the patient (better comfort due to the decrease of the drug administrations). The already mentioned benefits have a special importance in the treatment diseases, especially to those that require continuous treatment.

1.2. Systems that Modulates the Drug Release

In this part we are going to explain the different strategies and systems for drug delivery that already exist, classified by the administration route.

1.2.1. Enteral Administration

Those systems pretend to release the active substance in a concrete area of absorption inside the gastric tract with an already known and predetermined velocity. The main troubles to achieve this purpose are the difficulty to place and maintain the drug in the desired gastrointestinal area, the damage that the gastric fluid and other digestive liquids can produce to the active form of the drug, and the incapability to control the interpersonal variability of the process of the gastric emptying. Even that there are some existing strategies and devices; some of them already patented, that allow controlling the drug release:

Matrix Systems: are made by a mixture of the active ingredient and the excipient, both compressed.

Systems with Release Controlled by Layers: in this case the drug release is done when the coverture (layer) is dissolved or become permeable in contact with the medium. This layer/coverture can be applied on drug particles or on a complete dosage form like a pill.

Osmotic Systems: in this case the drug release is controlled by the osmotic pressure that is originated inside the device. These systems are composed by a nucleus formed by the active substance and the osmotic agent both covered by a semipermeable membrane that allows only the passage of water and presents an orifice. When the system is in contact with the biologic fluids, those can penetrate inside the membrane and the active substance is released by means of the hole due to the inside increasing presure.

Chemical Controlled Systems: the release of the active ingredient is controlled by a chemical reaction that produces the erosion of the encapsulating material.

Floating Systems: those systems have a lower density that the gastric fluids, for this reason they are maintained in the stomach during all over the gastric emptying.

Bioadhesive Systems: those systems contain the drug interposed in a polymer. After the administration this polymer is fixed in a determined area which leads to the active ingredient release there.

Systems for Colon Release: The colon is a less hostile medium compared with the small intestine and stomach due to its enzymatic activity and pH. In addition, the administration device, like the food bolus, will remain in the colon for a longer time. Those administration systems can use specific signals that allow them to recognize that they

have reach the colon, like the change in pH or the enzymatic activity of the colonic bacteria [16].

1.2.2. Parenteral Administration

Those systems using the parenteral routes are looking for effective plasmatic drug levels during long time periods. This route is involving all the non-enteral routes, like intravenous, subcutaneous, intramuscular, intraperitoneal, intraspine, between others. For this reason both implants and particles can be used.

1.2.2.1.Implants

Generally they can be defined as systems that are inserted by surgery. They need to have basic features like biocompatibility. Besides the components have to be inert, non carcinogenic, hypoallergenic and stable in the implanted area, and should not cause inflammatory response. We can distinguish between biodegradable, non-biodegradable implants.

Biodegradable Systems: they are eliminated by the organism, it is not necessary to remove them from the body once the treatment is finished. Silicon implants can be included in this section since they present degradation in contact with body fluids.

Non-biodegradable Systems: they are not eliminate by the organism in a natural way, that mean that they have to be removed from the body otherwise they will remain in it. Alumina implants can be included in this section since they degradation in contact with body fluids is negligible.

1.2.2.2. Intravenous Administration

Using this route of administration the drug formulation does not need to cross any membrane in the body since it is reaching the systemic circulation immediately. Even that, it requires trained personnel, it is uncomfortable for the patient, and sterility is needed. Using this route we can take advantage of the already mentioned EPR effect, so nanoparticles are good candidates for this administration route.

1.2.2.3. Transdermic Administration

This route is used to administrate active ingredients to the systemic distribution across the skin. Transdermal patches are devices formed by several layers that allow the release of the active substance in variable periods of time.

The fundamental principle that this system requires is that the velocity of the release has to be lower than the velocity of the penetration across the skin. This way the release is the limiting factor of the drug administration.

But more related to nanotechnology, Microneedles are constructing the base for a new thechnique for delivering little amounts of drug across the skin without any pain. They are composed by a great amount of structures with a smaller diameter than a human hair. The microneedles do not cause any pain to the patient because they are penetrating the external layer of the skin (epidermis) where there are no nerve endings. Once the drug is released it can reach the systemic circulation using small capillaries.

1.2.2.4. Ophthalmic Administration

Frequently it is impossible to obtain effective levels of the active ingredient in the eye using the systemic administration. For this reason a local administration is needed. In order to avoid frequent dosage a drug delivery system is really helpful. In addition, microparticles and nanoparticles are presenting a good size to be administered by a needle without surgery [17, 18].

1.4. Objectives and Structure of this PhD Thesis

The objectives of this PhD thesis are the following:

Design and fabricate different nanoporous anodic alumina structures.

Design drug delivery systems using nanoporous anodic alumina structures by different strategies.

Measure and optimize the drug release for every alumina structure.

Optimize the porosity and the size of silicon nanoparticles for drug delivery systems.

After a brief introduction about drug delivery systems, the motivation of this PhD thesis is explained in chapter 1. In chapter 2 the fundamentals of nanostructured anodic alumina are described, including the history of nanostructured Anodic Alumina and the basis of the alumina formation. Chapter 3 deals with the fabrication of Nanoporous Anodic Alumina detailing the electrochemical cells that have been used. Chapter 4 focuses on Nanoporous Anodic Alumina for stimuli-responsive drug release. Drug release profiles using different pore architectures are

presented in chapter 5. Chapter 6 is presenting some background, fabrication and particle size optimization for drug delivery using porous silicon. Chapter 7 summarizes and presents the conclusions obtained in this PhD dissertation.

1.5. References

1. Hoffman AS (2008) The origins and evolution of "controlled" drug delivery systems. J Control Release 132:153–63. doi: 10.1016/j.jconrel.2008.08.012
2. Yezhelyev M V., Gao X, Xing Y, et al. (2006) Emerging use of nanoparticles in diagnosis and treatment of breast cancer. Lancet Oncol 7:657–667. doi: 10.1016/S1470-2045(06)70793-8
3. Shan Tang O, Schweer H, Seyberth HW, et al. (2002) Pharmacokinetics of different routes of administration of misoprostol. Hum Reprod 17:332–336. doi: 10.1093/humrep/17.2.332
4. Hernández Herrero G (2010) Tratado de medicina farmacéutica. Médica Panamericana, Madrid :
5. Shargel L, Wu-Pong S, Yu ABC (2012) Applied Biopharmaceutics & Pharmacokinetics, Sixth Edit. Mc Graw Hill Medical
6. Juarez-Olguín H, Sandoval-ramirez E, Guillé-Pérez A (2009) Comportamiento del proceso LADME de los medicamentos en niños. Acta Pediatr Mex 30:23–30.
7. Lin CC, Metters AT (2006) Hydrogels in controlled release formulations: Network design and mathematical modeling. Adv Drug Deliv Rev 58:1379–1408. doi: 10.1016/j.addr.2006.09.004

8. Fang J, Nakamura H, Maeda H (2011) The EPR effect : Unique features of tumor blood vessels for drug delivery , factors involved , and limitations and augmentation of the effect ☆. Adv Drug Deliv Rev 63:136–151. doi: 10.1016/j.addr.2010.04.009
9. Maeda H, Wu J, Sawa T, et al. (2000) Tumor vascular permeability and the EPR effect in macromolecular therapeutics : a review. 65:271–284.
10. Matsumura Y, Maeda H (1986) A New Concept for Macromolecular Therapeutics in Cancer Chemotherapy : Mechanism of Tumoritropic Accumulation of Proteins and the Antitumor Agent Smancs1. Cancer Res 46:6387–6392.
11. Northfelt DW, Martin FJ, Working P, et al. (1996) Doxorubicin Encapsulated in Liposomes Containing Polyethylene Glycol : Tumor and Safety in Patients with Kaposi ' s Sarcoma. J Clin Pharmacol 36:55–63.
12. Leunig M, Yuan F, Menger MD, et al. (1992) Angiogenesis , Microvascular Architecture , Microhemodynamics , and Interstitial Fluid Pressure during Early Growth of Human Adenocarcinoma LSI74T in SCID Mice 1. Cancer Res 52:6553–6560.
13. Porta-i-Batalla M, Eckstein C, Xifré-Pérez E, et al. (2016) Sustained, Controlled and Stimuli-Responsive Drug Release Systems Based on Nanoporous Anodic Alumina with Layer-by-Layer Polyelectrolyte. Nanoscale Res Lett 11:372. doi: 10.1186/s11671-016-1585-4
14. Wang YJ, Caruso F (2006) Template synthesis of stimuli-responsive nanoporous polymer-based spheres via sequential assembly. Chem Mater 18:4089–4100. doi: Doi 10.1021/Cm060866p
15. Cho Y, Lim J, Char K (2012) Layer-by-layer assembled stimuli-responsive nanoporous membranes. Soft Matter 8:10271. doi: 10.1039/c2sm26562a

16. Minko T (2004) Drug targeting to the colon with lectins and neoglycoconjugates. Adv Drug Deliv Rev 56:491–509. doi: 10.1016/j.addr.2003.10.017
17. Low SP, Voelcker NH, Canham LT, Williams KA (2009) The biocompatibility of porous silicon in tissues of the eye. Biomaterials 30:2873–2880. doi: 10.1016/j.biomaterials.2009.02.008
18. Cheng L, Anglin E, Cunin F, et al. (2008) Intravitreal properties of porous silicon photonic crystals : a potential self-reporting intraocular drug- delivery vehicle. Br J Ophthalmol 92:705–711. doi: 10.1136/bjo.2007.133587

UNIVERSITAT ROVIRA I VIRGILI
DEVELOPMENT OF NANOPOROUS ANODIC ALUMINA TECHNOLOGIES FOR DRUG DELIVERY
Maria Porta Batalla

Chapter 2

Fundamentals of Nanoporous Anodic Alumina

UNIVERSITAT ROVIRA I VIRGILI
DEVELOPMENT OF NANOPOROUS ANODIC ALUMINA TECHNOLOGIES FOR DRUG DELIVERY
Maria Porta Batalla

In this chapter the origins and state of the art of Nanoporous Anodic Alumina (NAA) are presented. Also the basis of NAA formation like the electrochemical reactions, pore ordering methods and anodization parameters are accurately explained. We have exposed the anodization parameters and the structural NAA characteristics separately although the NAA characteristics are caused by the anodizing parameters. They are deeply related as it can be seen in the last table in this chapter.

2.1. History of Nanostructured Anodic Alumina

The History of the electrochemical oxidation of the aluminium dates back in 1920. By those dates they were looking for techniques for producing protective or decorative layers in the metal for commercial purposes. Aluminium pieces exposed to the atmospheric air are creating a natural protective layer of aluminium oxide (alumina). This observation triggers some ideas to change the material properties. In 1923 Bengough-Stuart used chromic acid for the anodization to protect aluminium pieces used. They patented this procedure used for protecting the aluminium alloys from corrosion by means of this anodic procedure.

More recently, applications of porous alumina with huge surface area and relatively narrow pore size have been exploited. In 1927 Glower and O'Brien patented the first sulphuric acid anodization. Afterwards Carboni developed a coloring method consisting of anodization in sulphuric acid followed by the application of an alternating current in a metal salt solution in 1936.

Thanks to the electron microscopy development porous alumina structures could be better understood. Keller et al. published a great description of the porous alumina structure in 1953. They descrived the porous alumina as an hexagonally close-packed duplex structure consisting of pores and a barrier layer. They also demonstrated the relationship of an applied potential and the geometric qualities of the pores such as the interpore distance.

In 1969 Diggle et al. published a review about Anodic Oxide Aluminum [1]. In this paper structural topographies regarding water content and anion incorporation in the oxide and theoretical models of formation mechanisms of both the barrier-type oxide and the porous-type oxide were described. On late 80s and early 90s Thompson and Wood published an article about deep understanding in the growth mechanisms of alumina oxide layers and provide a better knowledge of the grown mechanism of the anion incorporation in the NAA structure. Masuda and Fukuda published an article about self-ordered porous alumina membrane based on a two-step replicating process on 1995 [2].

2.2. Basis of Nanoporous Anodic Alumina Formation

Anodic Aluminum oxide can be formed in two kind of typologies: without pores and with pores. The anodization in neutral electrolytes (pH 5-7), like borate or oxalate gives nonporous membranes. Meanwhile anodizations in acidic electrolytes as sulphuric, oxalic or phosphoric gives porous membranes. In these thesis we have centred our attention on the porous ones.

2.2.1. Electrochemistry of Nanoporous Anodic Alumina

2.2.1.1. Thermodynamics

Regarding thermodynamics, when aluminium is exposed to air or water, due to the presence of oxygen, they react spontaneously and a thin film of aluminium oxide is formed. This phenomenon is thermodynamically favoured by the big negative Gibb's free energy change. [3]

$$2Al + {}^{3}/_{2}\, O_2 = Al_2O_3 \quad \Delta G^{o}\text{=-1582kJ/mol} \qquad (2.1)$$

$$2Al + 3H_2O = AL_2O_3 + 3H_2 \quad \Delta G^{o}\text{=-871kJ/mol} \qquad (2.2)$$

In terms of the electrochemistry, the anodization process of the aluminium for fabricating Nanoporous Anodic Alumina is usually prepared using an electrolyte consisting of an aqueous solution of sulphuric, oxalic or phosphoric acid where the anode (aluminium) and cathode (platinum wire) are partly immerserd. Once the anoditzation voltage (U), that will be different for every electrolyte, is applied between the anode and the cathode, pores nucleate and grow deep into the aluminium surface. Under a constant U, the anodization current density (J) versus time (t) curve can be divided into four regions (**Figure 2.1**):

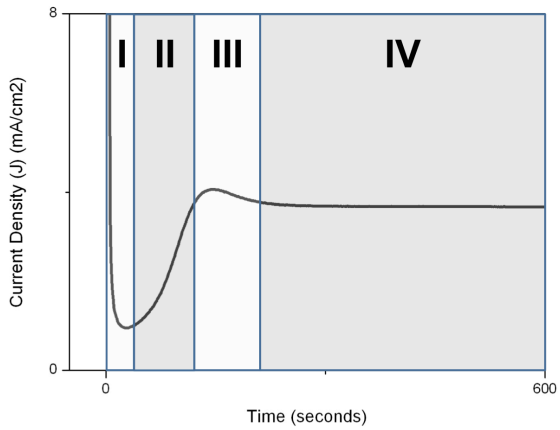

Figure 2.1. Current density vs. Time curve for the first 600 seconds during the anodization of a high-purity aluminium foil under potentiostatic conditions in 0.3M oxalic acid at 40V and 5ºC. Regions I, II, III and IV represent the different stages of the NAA formation.

In **region I**, current density (J) will reach a high value really quickly which can be attributed to the existence of electrolytic process of water. As the thin and compact barrier layer of aluminium oxide is being created onto the aluminium that is in contact with the electrolyte, the current density decreases abruptly. Is during this region when the barrier layer is growing faster, and the total resistance is rising consistently. Finally the current density (J) decrease sharply to reach the lowest value under the potentiostatic mode, when the barrier layer thickness increases [4–6].

At this point the **region II** begins. Parkhutik et al. proposed a theory in which localized paths can be created in the abovementioned oxide barrier layer to create real pores. This pore construction mechanism has been broadly discussed: O'Sullivan et al. have reported that the anodization current density (J) is concentrated on the weaknesses parts or defects of the barrier layer that gives differences on the layer settlement [7]. Moreover, according to the theory of Thomson et al. the pathways may be initiated from the cracking areas of the initial oxide barrier layer because of the cumulative tension stress [1, 8, 9].

Then some of the pores will continue growing creating real pores but some will stop. Thanks to this the J will increase to a regional maximum value because of the total decreasing resistance, now starts the **region III**.

During this **region III**, pores nucleate on the oxide thin film. Some pores will combine with others so the pore density will decrease. Then an equilibrium between the forming and the dissolving aluminium oxide is reached and the **region IV** starts [4, 6, 10].

The process can be explained by the following redox equations, and by **figure 2.2**:

At the anode:

Formation of the alumina (aluminium-alumina interface) where the oxide is growing:

$$2Al + 3H_2O = Al_2O_3 + 6H^+ + 6e^- \quad (2.3)$$

Dissolution of the alumina (alumina-electrolyte interface)

$$Al_2O_3 + 6H^+ = 2Al^{3+} + 3H_2O \quad (2.4)$$

Diffusion of aluminium cations (within oxide barrier layer)

$$2Al = 2Al^3 + 6e^- \quad (2.5)$$

At the cathode:

Hydrogen evolution (electrolyte-cathode interface):

$$6H^+ + 6e^- = 3H_2 \quad (2.6)$$

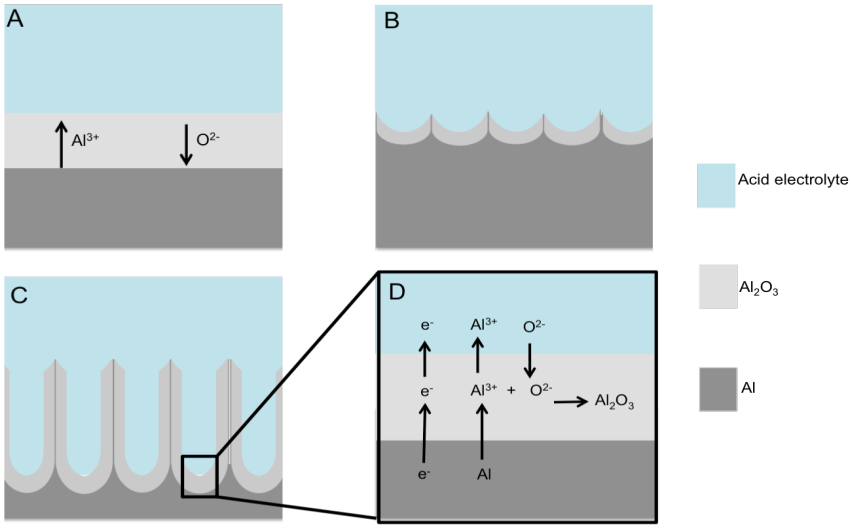

Figure 2.2. Schematics for the alumina pore formation. A) Formation of a thin compact layer of Al_2O_3 is formed corresponding to Region I in Figure 2.1. B) Instabilities in the electric field across the oxide film dissolve partially the oxide at certain sites; it corresponds to the Region II in Figure 2.1. C) Pore formation at the nucleation points corresponding to Region III and IV in Figure 2.1. D) Detail of the transport of the main ionic species though the oxide barrier layer.

2.2.1.2.Kinetics

At the same time the current density (J) of the anodization process under potentiostatic conditions is a result of combining the anion (Ja), cation (Jc) and electron (Je) current densities.

$$J = Ja + Jc + Je \tag{2.7}$$

But, as the electric conductivity of the aluminium oxide is really low (resistivity of alumina $\rho_{alumina}= 10^{14}\ \Omega/cm$), the current density of the electrons becomes negligible, and the current density expression stays like:

$$J \approx Ja + Jc \tag{2.8}$$

For this reason the anoditzaton procedure of aluminium is mainly limited by the ionic transport of the main ionic species (Al^{3+} and O^{2-}).

2.2.2. Pore Ordering

The pore ordering can be accomplished by two different methods: the Nano imprinting Lithography and the two-step anodization.

2.2.2.1. Nanoimprint Lithography (NIL)

This methodology produces a perfect pore ordering due to the fact that the pores nucleate at the defect sites in the aluminium substrate. Taking advantage of this above-mentioned process the Nanoimprint Lithography (NIL) is generating an ordered array of defects just to stimulate the pore nucleation at those specific locations (**figure 2.3**). This results in an ordered array of nanopores [11–13]. The major advantage of these process is the short time needed to fabricate the ordered NAA and the possibility of the fabrication of nanoporous anodic arrays of other lattices than hexagonal. Nevertheless this methodology is limited by the micro fabrication techniques available, as there is the need to create the master. An other methodology using laser interference lithography (LIL) has been also developed [14].

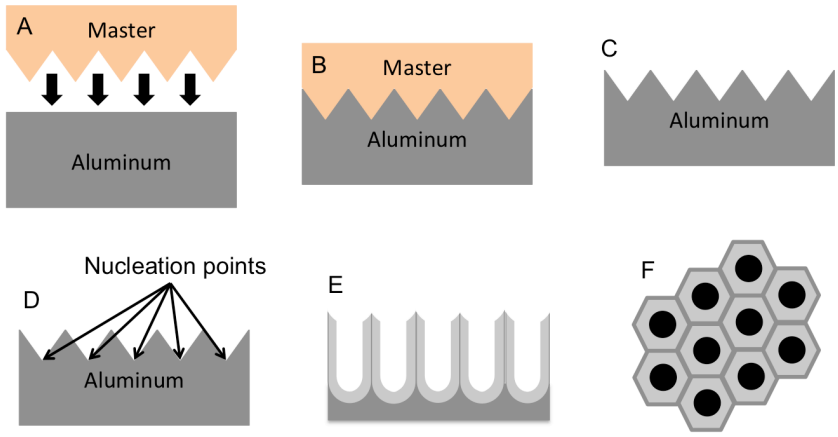

Figure 2.3. is showing the Nano imprinting Lithography method. A-B) using a master an specific pattern of defects are created on the aluminium substrate. C) The aluminium substrate is used for the electrochemical anodization. D) The defects in the aluminium will arise the nucleation points where the pores will grow. E-F) It results in a perfectly ordered nanoporous array.

2.2.2.2. Two Step Anodization

The two step anodization allow the self ordering fabrication of porous NAA membranes [7, 14–20]. These method for obtaining self-ordered NAA by means of two-step anodization was first published by Masuda and Fukuda back in 1995 [2]. They observed that after long anodization the pores at the bottom of the samples were ordered in hexagonal arrays, giving perfect ordered pores. This way, a first anodization can give an ordered pattern once the alumina is removed. Then a second anodization will provide ordered pores. It is represented in **figure 2.4.**

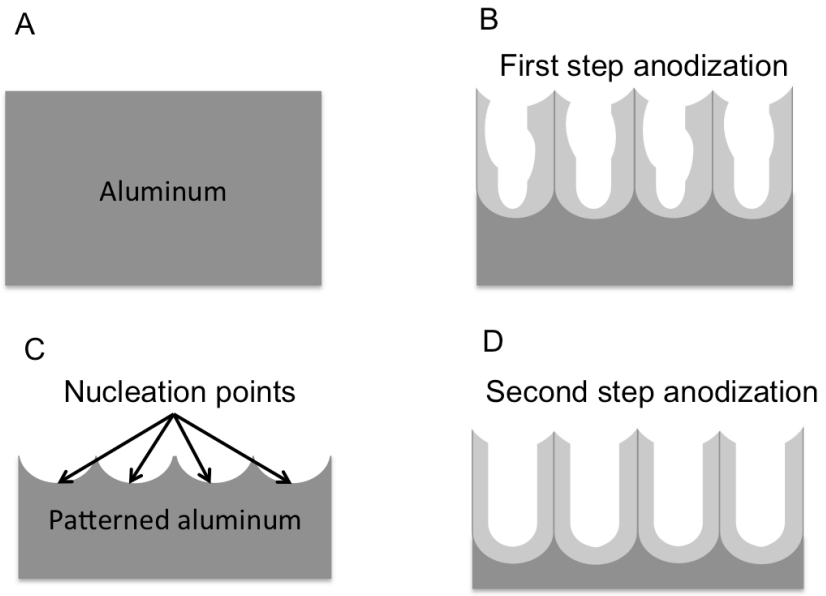

Figure 2.4. A) The two-step anodization starts with a flawless aluminium sheed. B) A first anodization (first step) is performed in which the pores are gaining order as they are growing deep in the aluminium bulk. C) The aluminium oxide is removed leaving a perfect ordered semi-spherical defects in the aluminium sheed. D) A second step is performed with perfectly ordered pores as a result.

2.2.2.3. The Mechanical Stress Model

The self-ordering phenomenon in NAA has been attributed to the mechanical stress at the metal/oxide interface. As the density of the Al_2O_3 is lower than the aluminium substrate, the volume of this Al_2O_3 expands twice the original volume of the aluminium substrate. This change in volume provokes repulsive forces that lead to pore ordering [17, 21].

2.2.3. NAA Pore Structure

2.2.3.1.The Unit Cell

Nanoporous Anodic Alumina (NAA) membranes are made of hexagonal unit cells. Each unit cell contains three different parts: The skeleton, an hexagonal inner layer which is made of the common internal walls between the unit cells, an outer layer between the central pore and the inner layer and an interstitial rod inside the inner layer at the triple cell junction.

The pore structural parameters are: interpore distance (D_{int}), pore diameter (D_p), barrier layer thickness (T_b), pore wall thickness (T_w), pore density (ρ_p) and porosity (P) as it can be checked in **figure 2.5.**

These parameters are dependent on the electrolyte type, anodization voltage, anodization current density and temperature as it is exposed afterwards [7, 16–18].

2.2.3.2.Chemical Composition

Chemically, two main areas can be recognised in the structure of the NAA. One that is an inner layer close to the aluminium-alumina interfaces that is basically composed of pure alumina. And the other is an outer layer located between the inner layer and the alumina-electrolyte interface, which is contaminated by anionic species from the acid electrolyte. Moreover it has been discovered by Han et al. [22] that there is a relationship between the anionic impurities incorporated and the anodization time.

It was also revealed that the decrease of the electrolyte concentration causes a decrease of the relative thickness of the anion contaminated outer pore wall to the pure inner pore wall. This way the contaminated area will be thicker to the top of the pore, meanwhile this outer contaminated zone is thinner at the bottom of the pore, as the electrolyte concentration is being reduced. It is schematically illustrated in **figure 2.6**.

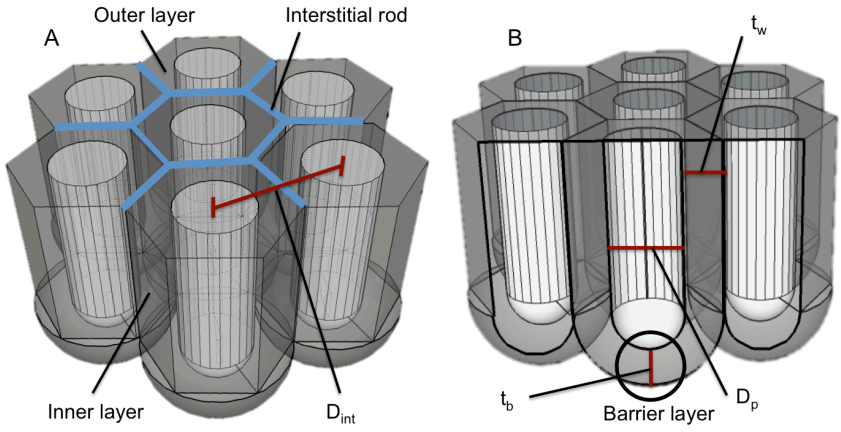

Figure 2.5. A) The unit cell is formed by pores equally distanced ones from others, this distance is named interpore distance (Dint). Other parts of the unit cell are: Interstitial rod, outer layer and inner layer. B) Other parameters are, the barrier layer thickness (T_b), the wall thickness (T_w) and the pore diameter (D_p).

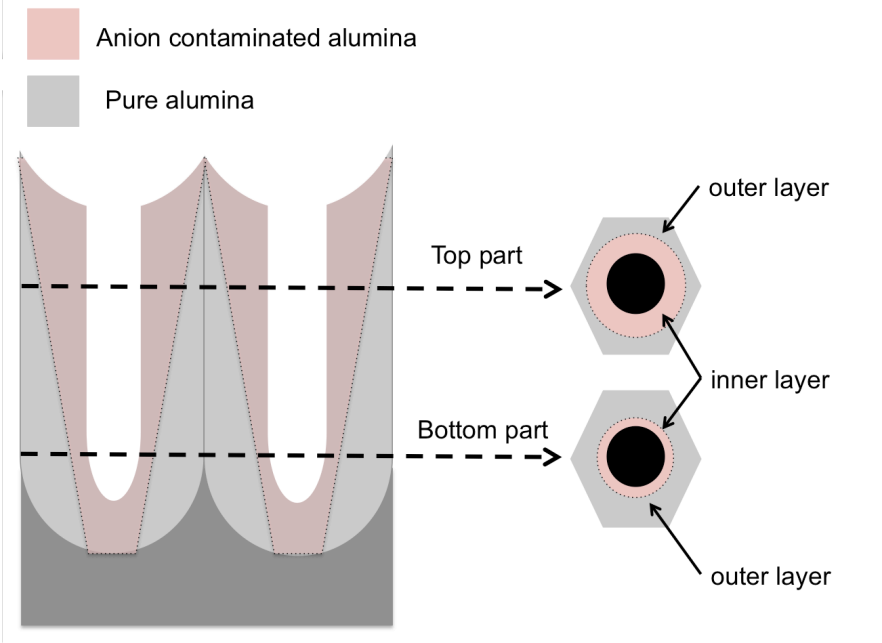

Figure 2.6. Cross section and top view schematics of nanoporous anodic alumina pores showing the anion contaminated area (in pink) inside the pore wall.

In addition those layer differences is that the outer layer (the contaminated one) is less resistant to the chemical etching than the inner one. This inner property prevents the structure from collapsing even at high porosity [19, 23, 24].

2.2.4. Anodization Parameters

The structural characteristics of the NAA can be controlled by the anodization parameters. Those parameters are: anodization type, anodization voltage, anodization time, electrolyte characteristics, and

aluminium substrate. Remember that the structural characteristics of the NAA are: pore diameter, interpore distance, porosity, degree of hexagonal pore arrangement, and barrier layer thickness. It has to be also taken in consideration that the acid electrolyte needs to be stirred at the same rate during all the etching procedure in order to ensure that the diffusion of the ionic species and temperature inside the pores is homogenous.

2.2.4.1. Anodization Type

Two kinds of Aluminum anodization can be produced: Mild Anodization and Hard Anodization.

2.2.4.1.1. Mild Anodization

Mild anodization (MA) is based on anodization of aluminium under potentiostatic conditions and small potentials. It is characterized by the slow linear growth of the NAA film. This anodization type is the one mainly used in academic research due to its uniform pore size (D_p) and interpore distance (D_{int}) that can be easily tuned by selection of appropriate anodization conditions [4].

2.2.4.1.2. Hard Anodization

Hard anodization (HA) appeared as an alternative to Mild Anodization (MA) to produce NAA films faster and with higher pore ordering. This anodization type is using voltages over the breakdown potentials (breakdown potentials are 27, 50 and 197 V for sulphuric, oxalic and phosphoric acids respectively) [4]. Contrarily to MA the growth of the NAA is not linear. A stable anodization in a given electrolyte is difficult to maintain over the breakdown potential due to

the occurrence of burning or breakdown of the growing anodic oxide film. For this reasons HA processes are not being employed for nanotechnology research.

2.2.4.2. Anodization Voltage

The anodization voltage (U) is limited for a given acid electrolyte and concentration. If the anodization voltage is too high the oxide barrier layer will breakdown (also known as "burning") and the pore growth will not be homogeneous. This phenomenon occurs due to the conductivity increase in the barrier layer at the pore bottom. That will produce a local heating, the ionitzation of the atoms that generates more electrons due to the energy from the electric field and the breakdown of the oxide barrier layer from the existing cracks.

The conductivity of the most typical acid electrolytes used for the aluminium anodization follows the sequence $H_2SO_4 > H_2C_2O_4 > H_3PO_4$. According to this, the values of the anodization voltages are written in **table 2.1**.

Table 2.1. Voltage values for every electrolyte typology and anodization type.

	Sulphuric Acid (H_2SO_4)	Oxalic Acid ($H_2C_2O_4$)	Phosphoric Acid (H_3PO_4)
Mild Anodization	20 V	40 V	195 V
Hard Anodization	Over 27 V	Over 50 V	Over 197 V

2.2.4.3. Anodization Time

Usually the NAA layer thickness (L) is controlled by the anodization time (t). Under galvanostatic conditions the relationship between layer thickness (L) and time (t) is linear. However under potentiostatic conditions, the template thickness does not grow linearly. So, to fabricate NAA with controlled thickness under such anodization conditions, it is more accurate to control the layer thickness (L) using the total current charge (Q) since the relationship between L and Q is linear under potentiostatic conditions [25, 26].

2.2.4.4. Acid Electrolyte

Electrolyte composition is fundamental for the fabrication of excellent NAA films. As we have already mentioned, the usual acid electrolytes used for fabricating NAA are sulphuric acid, oxalic acid and phosphoric acid. Even though several exotic acids such as tartaric and formic have been tried. The type, concentration, temperature, pH and viscosity of the acid electrolyte is strongly affecting the structural characteristics of the NAA.

2.2.4.4.1. Electrolyte Temperature

Temperature of the electrolyte is affecting the pore growth rate. An electrolyte temperature decrease will provoke a pore grow decrease. To avoid the nanoporous anodic alumina dissolving and oxide breakdown (commonly known as sample burning) during the anodizing process the temperature of the acid electrolyte must be kept colder than the room temperature. The used temperature for sulphuric and oxalic acids was 5ºC. For phosphoric acid we used temperatures between -3ºC

and -10ºC and a quantity of ethanol was added to the solution in order to avoid from freezing.

2.2.4.4.2. Electrolyte pH

The pH value is affecting basically the pore diameter. The pH value is given by the type and concentration of the acid electrolyte. Low pH values needs low anodization voltages. That implies a reduced field-assisted dissolution of Al_2O_3 and the pore diameter becomes smaller. This is the reason why the pores are wider when the electrolyte used is H_3PO_4 and narrower when the electrolyte is H_2SO_4.

2.2.4.4.3. Electrolyte Viscosity

Viscosity (υ) of the electrolyte has a direct effect on the resulting nanostructure. This effect is related with the reduction of the electrophoretic velocity of the ions as it is expressed in **equation 2.9**.

$$v = \frac{\varepsilon \xi E}{\pi \eta} \tag{2.9}$$

Where the υ is the electrolyte viscosity, ε is the dielectric coefficient, ξ is the zeta potential, E is the electric field and η is the viscosity coefficient.

This reduction of the viscosity (υ) decreases the current density developed during the anodization. This reduction of the current density diminishes the growth rate of NAA but also reduces Joule's effect and prevents localized heating at pore tips. This is the reason why increasing the viscosity of the electrolyte helps to avoid oxide breakdown, especially at high electric fields [27].

The common additives used for adjusting the electrolyte viscosity are Ethyleneglycol (EG), Polyethileneglycol (PEG) and glycerol. Those chemicals, apart from reducing the viscosity (υ), also prevent chemical dissolution of the porous structure by the electrolyte, thus reducing the porosity of the resulting NAA film[28]. Viscosity, a part from stabilizing the anodization at high potentials and reducing the porosity, has been proved to have a direct effect on the interpore distance (D_{int}).

Some research using 0.3M of oxalic acid electrolyte was performed in order to prove the relation between the glycerol concentration and the interpore distances. They found that this dependence was linear to the logarithm of the resulting viscosity. Additionally, they found that for a glycerol-based electrolyte no pores were generated and a barrier-type alumina was produced [29].

2.2.4.5. Aluminium Substrate

High purity aluminium foils (99.9%) are needed to be able to obtain high-quality NAA films. Otherwise the presence of impurities or contamination in the aluminium substrate provokes volume expansion and disturbances on the electric field that led to defects in the structure [30].

2.2.5. Structural Characteristics of NAA

2.2.5.1. Pore Diameter

Pore diameter (D_p) can vary from 10 to 400 nm and it has a direct proportional relation with voltage, temperature, time and electrolyte pH. That means that, the larger these parameters are, the

bigger the pore diameter will be. We can find the pore diameter (D_p) in the following equation:

$$D_{int} = D_p + 2t_w \quad (2.10)$$

Where, D_{int} is the interpore distance, D_p is the pore diameter and t_w is the wall thickness.

2.2.5.2. Interpore Distance

The interpore distance is the distance between the centres of two contiguous pores. It can be calculated by the mean value of several interpore measurements. According to **equation 2.11.** the interpore distance (D_{int}) is directly proportional to the anodization voltage, where K depends on the anodization regime, for the hard anodization its value is 2.0 nm/V, meanwhile for the mild anodization is 2,5-2,8 nm/V [18]. The interpore distance can also be calculated by the **equation 2.10**.

$$D_{int} = KV \quad (2.11)$$

Where D_{int} is the interpore distance, K is the proportionally constant and V is the applied voltage.

2.2.5.3. Porosity

The NAA porosity (P) can be estimated by the **equation 2.12.** Under mild anodization conditions porosity follows the 10% porosity rule [19]. However under hard anodization conditions, it's values are reduced to 3,3% [18].

$$P(\%) = \left(\frac{\pi}{2\sqrt{3}}\right)\left(\frac{D_p}{D_{int}}\right) x\ 100 \qquad (2.12)$$

Where P is porosity in %, D_p is the pore diameter in nanometers and Di_{nt} is the interpore distance in nanometers.

2.2.5.4. Pore Density

From the practical point of view, it is sometimes beneficial to give the porosity of the structure defined as a ratio of the surface occupied by the pores to the total surface of the sample. In this case the pore density (ρ_p), that is the number of pores that can be found on an specific area, can be useful. Pore density can be calculated by using **equation 2.13**.

$$\rho_P = \left(\frac{2}{\sqrt{3}D_{int}^2}\right)\ x\ 10^{14} \qquad (2.13)$$

Where ρ_p is the pore density and D_{int} is the interpore distance.

2.2.5.5. Hexagonal Pore Arrangement

The degree of the hexagonal pore arrangement can be disturbed for several reasons: the grain boundaries, the length of the anodization and the parallel trenches in the aluminium substrate caused by the industrial rolling. First, the grain boundaries are perturbing the pore arrangement, in order to reduce the number of grain boundaries and enlarge the polydomain areas (areas with the same pore lattice orientation) annealing processes at 400ºC under N2 atmosphere for 3 hours is recommended. Then as longer anodization times lead to ordering the deviations due to the changes on pH values inside the pores,

24h first step anodization are recommended. In addition electropolishing procedures are recommended to avoid the surface roughness (parallel trenches) in the purchased aluminium sheeds.

2.2.5.6. Barrier Layer Thickness

The oxide barrier layer thickness (T_b) at the pore bottom is directly proportional to the anodization voltage (**equation 2.14**). The proportionally constant (K) depends on the anodization regime and it takes 1,3 and 1,0 nm/V values for mild and hard anodization respectively. In accordance with the high field conductivity theory, barrier layer thickness (T_b) is inversely proportional to current density (J)[18].

$$T_b = KV \tag{2.14}$$

Where T*b* is the barrier layer thickness value, K is the proportionally constant and V is the voltage.

2.2.5.7. Pore Growth Rate

The pore growth rate (R_p) is affected by the acid electrolyte temperature (T). It is directly dependant, so R_p is decreasing as the temperature is reduced. In order to prevent the NAA from dissolving in the course of the anodization process, the temperature needs to be kept lower than room temperature, usually at 5ºC or even lower than 0ºC for some hard anodizations. Another parameter that has an effect on the R_p is the stirring rate of the acid electrolyte since this mixing is ensuring the diffusion of the ionic species and the homogeneity of the T inside the pores.

2.3. Summary

This chapter has introduced a general description of the history and the state of the art of the NAA. It also explained the fundamentals for NAA formation including the relation between anodization parameters and NAA structural characteristics, that are summarised in **table 2.2**.

Table 2.2. Qualitative relationship indicating the direct or inverse dependence between anodization parameters and structural characteristics of the resulting NAA.

	Structural Characteristics				
Anodization parameters	D_{int}	D_p	P	T_b	R_p
U	Directly proportional	Directly proportional	Inversely proportional	Directly proportional	Directly proportional
t		Directly proportional	Directly proportional		Inversely proportional
T		Directly proportional	Inversely proportional	Inversely proportional	Directly proportional
pH	Directly proportional	Directly proportional	Directly proportional	Directly proportional	Inversely proportional

2.4. References

1. Shimizu K, Kobayashi K, Thompson GE, Wood GC (1992) Development of porous anodic films on aluminium. Philos Mag A 66:643–652. doi: 10.1080/01418619208201581
2. Masuda H, Fukuda K (1995) Ordered Metal Nanohole Arrays Made by a Two-Step Replication of Honeycomb Structures of Anodic Alumina. Science (80-) 268:1466–1468. doi: 10.1126/science.268.5216.1466
3. Santos A, Kumeria T, Losic D (2014) Nanoporous anodic alumina: A

versatile platform for optical biosensors. Materials (Basel) 7:4297–4320. doi: 10.3390/ma7064297

4. Lee W, Park S-JSS (2014) Porous anodic aluminum oxide: anodization and templated synthesis of functional nanostructures. Chem Rev 114:7487–7556. doi: 10.1021/cr500002z
5. Parkhutik VP (1992) Modelling of low-temperature oxidation of materials in gaseous environments. J Phys D Appl Phys 25:256–261. doi: 10.1088/0022-3727/25/2/019
6. Yi L, Zhiyuan L, Xing H, et al. (2012) Investigation of intrinsic mechanisms of aluminium anodization processes by analyzing the current density. RSC Adv 2:5164. doi: 10.1039/c2ra01050j
7. O'Sullivan JP, Wood GC (1970) The morphology and mechanism of formation of porous anodic films on aluminium. Proc R Soc London 317:511–543. doi: 10.1098/rspa.1970.0129
8. Thompson G. E (1997) Porous anodic alumina: fabrication, characterization and applications. Thin Solid Films 297:192–201. doi: 10.1016/S0040-6090(96)09440-0
9. Thompson G, Xu Y, Skeldon P (1987) Anodic oxidation of aluminium. Philos Mag Part B 55:651–667. doi: 10.1080/13642818708218371
10. Li F, Zhang L, Metzger R (1998) On the growth of highly ordered pores in anodized aluminum oxide. Chem Mater 10:2470–2480. doi: 10.1021/cm980163a
11. Choi J, Wehrspohn RB, Gösele U (2005) Mechanism of guided self-organization producing quasi-monodomain porous alumina. Electrochim Acta 50:2591–2595. doi: 10.1016/j.electacta.2004.11.004
12. Kustandi TS, Loh WW, Gao H, Low HY (2010) Wafer-scale near-perfect ordered porous alumina on substrates by step and flash imprint lithography. ACS Nano 4:2561–2568. doi: 10.1021/nn1001744

13. Kwon N, Kim K, Heo J, Chung I (2009) Fabrication of ordered anodic aluminum oxide with matrix arrays of pores using nanoimprint. J Vac Sci Technol A 27:803–807. doi: 10.1116/1.3139884
14. Montero Moreno JM, Waleczek M, Martens S, et al. (2014) Constrained order in nanoporous alumina with high aspect ratio: Smart combination of interference lithography and hard Anodization. Adv Funct Mater 24:1857–1863. doi: 10.1002/adfm.201303268
15. Diggle JW, Downie TC, Goulding CW (1969) Anodic oxide films on aluminum. Chem Rev 69:365–405. doi: 10.1021/cr60259a005
16. Keller F, Hunter MS, Robinson DL (1953) Structural Features of Oxide Coatings on Aluminum. J Electrochem Soc 100:411. doi: 10.1149/1.2781142
17. Li AP, Müller F, Birner A, et al. (1998) Hexagonal pore arrays with a 50–420 nm interpore distance formed by self-organization in anodic alumina. J Appl Phys 84:6023–6026. doi: 10.1063/1.368911
18. Lee W, Ji R, Gösele U, Nielsch K (2006) Fast fabrication of long-range ordered porous alumina membranes by hard anodization. Nat Mater 5:741–747. doi: 10.1038/nmat1717
19. Nielsch K, Choi J, Schwirn K, et al. (2002) Self-ordering Regimes of Porous Alumina: The 10 Porosity Rule. Nano Lett 2:677–680. doi: 10.1021/nl025537k
20. Masuda H, Yamada H, Satoh M, et al. (1997) Highly ordered nanochannel-array architecture in anodic alumina. Appl Phys Lett 71:2770. doi: 10.1063/1.120128
21. Jessensky O (1998) Self-Organized Formation of Hexagonal Pore Structures in Anodic Alumina. J Electrochem Soc 145:3735. doi: 10.1149/1.1838867
22. Han H, Park SJ, Jang JS, et al. (2013) In situ determination of the pore opening point during wet-chemical etching of the barrier layer of porous anodic aluminum oxide: Nonuniform Impurity Distribution in

Anodic Oxide. ACS Appl Mater Interfaces 5:3441–3448. doi: 10.1021/am400520d

23. Lee J, Nigo S, Nakano Y, et al. (2010) Structural analysis of anodic porous alumina used for resistive random access memory. Sci Technol Adv Mater 11:25002. doi: 10.1088/1468-6996/11/2/025002
24. Le Coz F, Arurault L, Fontorbes S, et al. (2010) Chemical composition and structural changes of porous templates obtained by anodising aluminium in phosphoric acid electrolyte. Surf Interface Anal 42:227–233. doi: 10.1002/sia.3199
25. Takahashi H, Nagayama M (1978) The determination of the porosity of anodic oxide films on aluminium by the pore-filling method*. Corros Sci 18:911–925.
26. Eftekhari A (2008) Nanostructured Materials in Electrochemistry. Wiley-VCH Verlag GmbH
27. Chen W, Wu JS, Xia XH (2008) Porous anodic alumina with continuously manipulated pore/cell size. ACS Nano 2:959–965. doi: 10.1021/nn700389j
28. Manzano C V., Martín J, Martín-González MS (2014) Ultra-narrow 12 nm pore diameter self-ordered anodic alumina templates. Microporous Mesoporous Mater 184:177–183. doi: 10.1016/j.micromeso.2013.10.004
29. Stępniowski WJ, Forbot D, Norek M, et al. (2014) The impact of viscosity of the electrolyte on the formation of nanoporous anodic aluminum oxide. Electrochim Acta 133:57–64. doi: 10.1016/j.electacta.2014.04.039
30. Kim B, Lee JS (2014) Effect of Aluminum Purity on the Pore Formation of Porous Anodic Alumina. Bull Korean Chem Soc 35:349–352. doi: 10.5012/bkcs.2014.35.2.349

UNIVERSITAT ROVIRA I VIRGILI
DEVELOPMENT OF NANOPOROUS ANODIC ALUMINA TECHNOLOGIES FOR DRUG DELIVERY
Maria Porta Batalla

Chapter 3

Nanoporous Anodic Alumina Fabrication

UNIVERSITAT ROVIRA I VIRGILI
DEVELOPMENT OF NANOPOROUS ANODIC ALUMINA TECHNOLOGIES FOR DRUG DELIVERY
Maria Porta Batalla

In this chapter, the experimental methods for fabricating nanostructures based on nanoporous anodic alumina are defined in detail.

First the electrochemical cell in our facilities is presented and deeply described.

Secondly, the fabrication processes for typical Nanoporous Anodic Alumina (NAA) are presented for different electrolyte conditions.

Thirdly, the fabrication processes for funnel shaped Nanoporous Anodic Alumina and for inverted funnel shape Nanoporous Anodic Alumina are accurately explained.

3.1. Experimental Setup

The experimental setup available in our lab facilities consists in a power supply controlled with personal computer, another power supply for the electrolyte stirring and a cooling system to maintain the temperature of the anodization cell below room temperature.

Figure 3.1 shows the setup displacement in our facilities. Part of this set up is assembled into a laboratory hood.

Our lab has been dedicated to a continuous improvement of the electrochemical anodization cell system. The actual anodization cell is duplicated in order to acquire more productivity.

The anodization cell consists of a cupper plate in contact with the anode, where the aluminium sample will be displaced. The cathode consists in a platinum ring placed in a Teflon holder that will be immersed in the electrolyte. This Teflon holder also contains a stirrer in order to maintain the electrolyte perfectly homogenous during all the anodization process. A metal plate in contact with a thermal insulator is placed below the cupper plate in order to maintain the anodization temperature under room temperature.

The power supply used for the anodization process in our research facilities is controlled with a personal computer, there is another power supply for the stirring and a cooling system as it can be seen in **Figure 3.1**.

Figure 3.1. Experimental equipment required for the fabrication of NAA films. a) Personal Computer b) Power supply for anodization c) Power supply for the stirrer d) Cooling system e) Anodization cell

3.1.1. Electrochemical Cell

Fundamentally, an electrochemical cell needs the following parts:

1) Anode
2) Cathode
3) Electrolyte
4) Power supply

The anode and the cathode are in contact by means of the electrolyte solution, for these reason they have to be immersed in it. The electrolyte is the medium for transporting the ionic species between the anode and the cathode (H^+, Al^{3+}, O^{2-}). The power supply gives the energy necessary to ionize the aluminium at the aluminium-alumina interface (anode) that produces electrons (e^-). Once the anodization voltage is applied the pores start to nucleate and grow within the Aluminium substrate. An schematics for an electrochemical cell can be seen in **figure 3.2**.

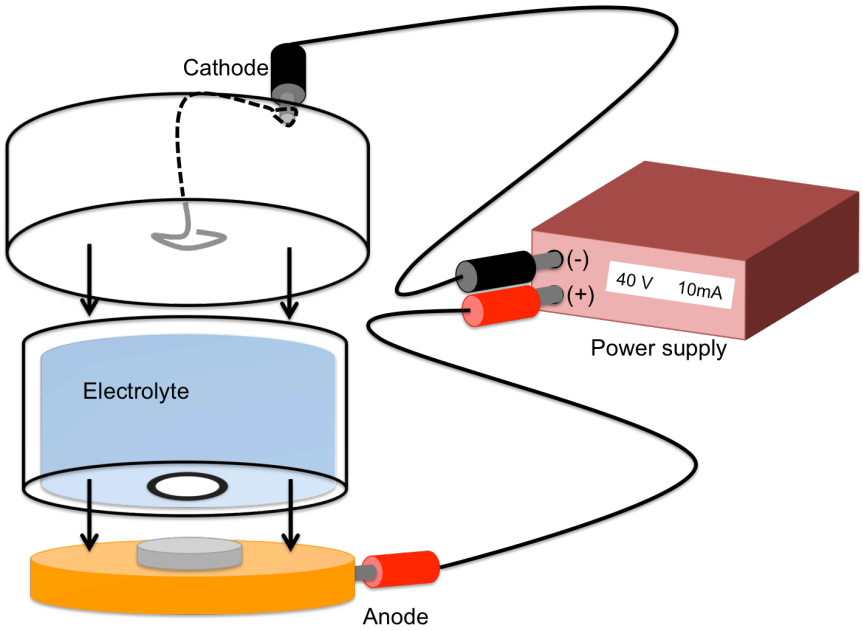

Figure 3.2. Schematics for the electrochemical anodization cell showing the anode, cathode and the power supply.

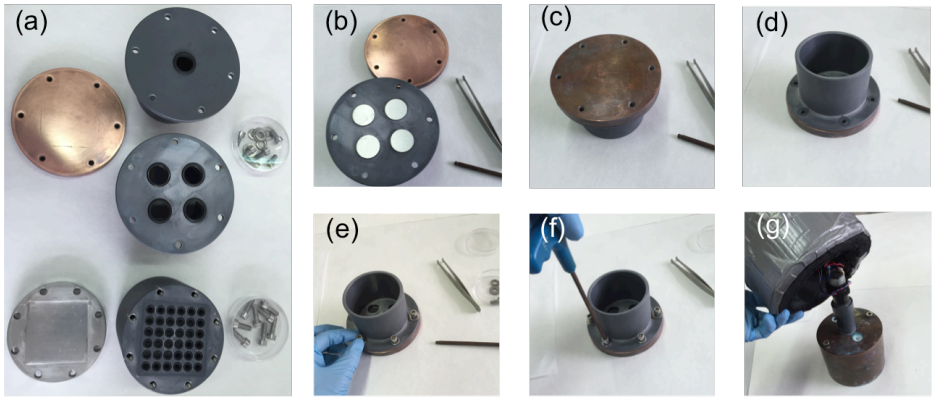

Figure 3.3. a) Different anodizing chambers available in our research facilities. b) Image showing the first step of the chamber assembling where the aluminium samples are displaced on the o-rings c) Image showing the second step of the chamber assembling where the cupper base is displaced covering the samples and directly in contact with them d) the chamber is turned upside-down to be able to see the holes where the screws will be placed. e-f) the screws are assembled screwing them in a cross shape in order to avoid to tight too much in one side. g) Finally the chamber is covered with the cathode and with an isolation hood.

Different electrochemical anodization chambers are presented on **Figure 3.3.** Depending on the dimension of the samples needed, different cell options are available in our research facilities. Images in **figure 3.3** also show the cell assembly procedure. All the chambers are armed with an o-ring that is a loop of elastomer with a round cross-section designed to be seated in the hole where the sample is placed. This o-ring will be compressed during the chamber assembly between the sample and the chamber in order to avoid the leaking of the electrolyte that will be held in the chamber.

The whole cell is thermo-isolated in order to keep the ideal temperature inside the chamber. A thermometer is held in contact with the electrolyte to ensure the right electrolyte temperature. (Figure 3.4)

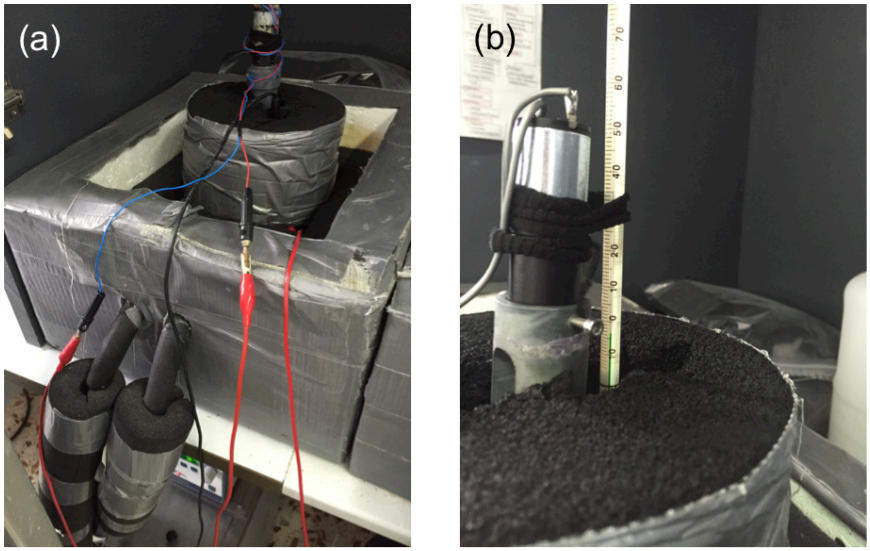

Figure 3.4. a) Image of the electrochemical cell insulator and the thermal cooling flux placed beneath the cell. b) Detail of the thermometer that report the electrolyte temperature.

3.1.2. Software

The control over the anodization of aluminium samples was performed with custom-made LabView-based programs. **Figure 3.5** shows a screen capture of a programme designed for the fabrication of Nanoporous Anodic Alumina samples. Accurate control of the sample characteristics can be achieved by adjusting the voltage and controlling either the anodization time or the total charge passing through the anodization cell.

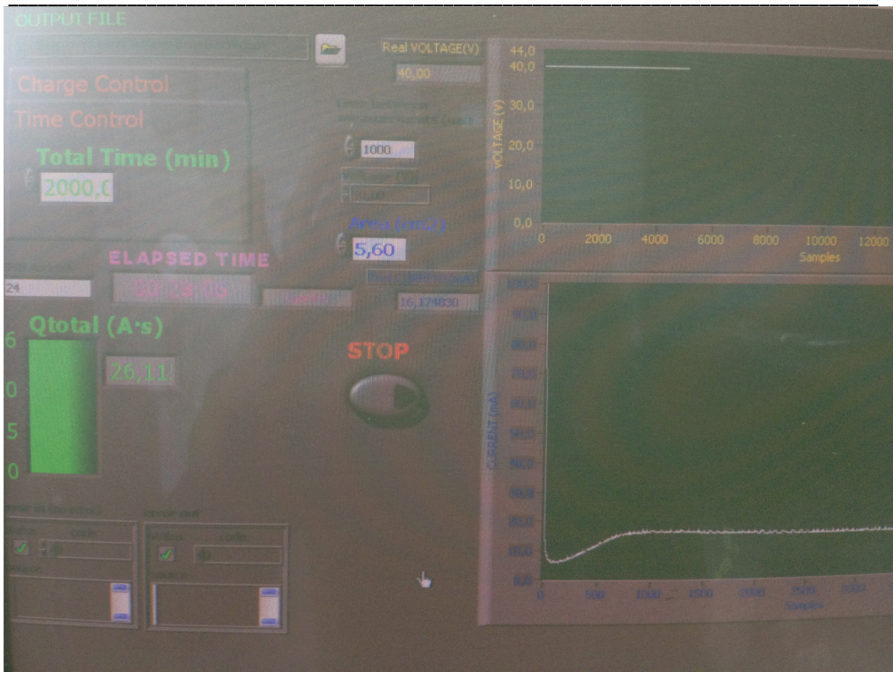

Figure 3.5. Screen capture of the Lab View based software used in our lab facilities

3.1.3.Aluminium Substrate

In order to obtain high-quality NAA, high purity aluminium sheets are needed, since the presence of impurities in the aluminium substrate leads to defects in the NAA, as it was already mentioned in chapter 2. For this reason, high purity Aluminium is generally used. Substrates used in our research had a purity of 99,9% and thickness of 0,5 millimeters and were obtained from Goodfellow Cambridge Ltd.

3.2. Pretreatments

To begin with, the aluminium substrate will have a pre-existing oxide layer over its surface, which is usuallly produced by the oxygen in

the atmosphere. In addition, the substrate could also have a pre-existing surface structure produced by a mechanical, thermal, chemical and electrochemical process. All of these surface treatments have an impact on the self-ordering of the pores that will be formed on the surface of the substrate during the anodization process. This is because the pore nucleation mechanism is a combination of both random nucleation and nucleation produced by the surface defects, such as scratches, pits, impurities and grain boundaries.

For this reason a typical pre-treatment of an Aluminium band is needed in order to eliminate the possible surface defects in the aluminium sample. The pre-treatment begins by first, degreasing the foil using acetone or a similar solvent, then 3 different kinds of polishing have been used in our research group: Mechanical polishing, chemical polishing and electrochemical polishing.

3.2.1.Mechanical Polishing

This technique is provably the one that have the lowest cost. The main drawbacks of this procedure are the time required and the fact that the surfaces can present a lot of scratches easily. So the control of the resulting surface is low. It consists of using an abrasive material to refine the aluminium surface.

3.2.2. Chemical Polishing

Chemical polishing of aluminium samples is an alternative to the electrochemical polishing in order to avoid the requirement of the complex electrochemical cell. Additionally it eludes the hazards related with perchloric acid. The procedure consist of immersing the aluminium

substrate in a mixture of 15 parts of nitric acid 68% wt and 85 parts of phosphoric acid 85% wt for 5 minutes. This immersion is followed by neutralization of the sample in 1M sodium hydroxide for 20 minutes. This procedure results in a roughness comparable to that of electrochemical polishing without the need of power supplies or the dangerous perchloric acid.

3.2.3. Electrochemical Polishing

Electrochemically polishing (electropolishing) is the most known process for polishing aluminium foils. Between it's advantages we can say it is fast and really effective. The result is a mirror-like finish. Several electrolytes are available for electropolishing but the most popular an the one that we use in our research facilities is 1:4 v:v mixture of perchloric acid in ethanol. Even that this technique has a big disadvantage that is the hazardousness of the perchloric acid ($HClO_4$). This acid is stronger than sulphuric or nitric and is an strong oxidant, so it has to be handled with extreme caution. The preparation of the electropolishing mixture has to be performed under 0ºC as there is risk of explosion due to the heat that is generated during the mixture.

3.3.Electrochemical Anodization

As it was already explained in chapter 2 we can distinguish between two kinds of anodization: Mild anodization and Hard anodization. These main anodization types are divided depending on the anodization regime [1–3].

3.3.1. Mild Anodization

Mild anodizations (MA) are based on anodizations of aluminium foils under potentiostatic conditions and small potentials, more concretely under the breakdown potentials (27, 50 and 197 V for sulphuric, oxalic and phosphoric acids respectively) This anodization is providing an uniform oxide layer grow and a good control of the pore size and interpore distance by means of anodizing parameters. The two step anodization technique is used for obtaining suitable pore ordering in this case[4, 5]. The corresponding anodization voltages, electrolyte temperatures and concentrations are shown in **Table 3.1.** There is a direct linear relation between the Anodizing potential (Voltage) and the interpore distance (distance between pores) shown in **Figure 3.6**. The first anodization step is usually performed for 20-24 h in order to achieve the maximum hexagonal pore arrangement. Once the first anodization is finished, the alumina (Al_2O_3) film with disordered pores on the top and ordered pores at the bottom is dissolved by wet chemical etching in a mixture of phosphoric acid (H_3PO_4) 0,4M and chromic acid (H_2CrO_7) 0,2M in a volume ratio 1:1 at 70ºC. We named this procedure as "*orange solution process*" due to the characteristic colour of the described acid mixture. It last for two hours and it is possible to confirm the alumina dissolution visually or by using an electric tester. At this point hemispherical patterns are produced in the aluminium surface. Then the second anodization can be performed. This second anodization time will depend on the desired thickness of the alumina layer. This second step anodization is controlled by total charge instead of time because this way we have a better control over the layer length as it will be explained in section 3.3.3. MA is the anodizing typology that is used in academic

research (also in this work) due to the uniform pore size and interpore distance.

Table 3.1. Anodization parameters of the commonly used acid solutions (sulphuric, oxalic and phosphoric) in mild anodization processes: electrolyte concentration, anodization voltage, electrolyte temperature, interpore distance (D_{int}) and pore diameter (D_p).

Acid	Concentration	Voltage (V)	Temperature (ºC)	Interpore Distance (nm)	Pore Distance (nm)
H_2SO_4	0,3M	20	5	50	10-15
$H_2C_2O_4$	0,3M	40	5	100	20-30
H_3PO_4	1 wt %	195	-5	500	100-130

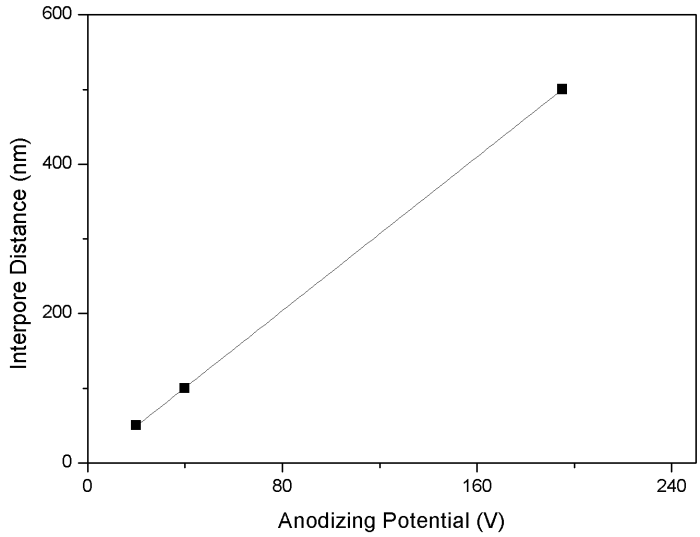

Figure 3.6. Correlation between interpore Distance and the anodizing Potential.

3.3.1.1. Sulphuric Acid Electrolyte

This anodization procedure is performed using 0,3M sulphuric acid (H_2SO_4) at 5ºC. the temperature is needed to keep constant during all the process. The voltage used for this electrolyte is 20 V. This anodization is performed using the two-step process. Then after the electropolishing the first anodization is performed for minimum 20 to 24 hours. After the first anodization the oxide layer is dissolved using the "*orange solution*" (explained in section 3.3.1). The oxide removal I followed by the second step anodization that is controlled by total charge instead of time [6, 7].

3.3.1.2. Oxalic Acid Electrolyte

This process is performed at 40 V using Oxalic acid ($H_2C_2O_4$) at 5 ºC. The two step anodization procedure is used in order to achieve an ordered pore array. After the electropolishing pre-treatment the first step anodization is performed for minimum 20 to 24 hours. Then the *orange solution* (see section 3.3.1) is used to remove the grown oxide. After that, the second step is performed using exactly the same parameters than the first step but it is controlled by total charge[8, 9, 2].

3.3.1.3. Phosphoric Acid Electrolyte

This Anodization has been also performed using the two step anodization procedure. The differential part of this anodization is that due to the high electric field (195 V), near the breakdown potential. First a protective layer anodized in a lower voltage is needed in order to avoid the local thickening, burning and cracking of the growing alumina layer. The phosphoric acid (H_3PO_4) concentration (electrolyte) used in this

anodization is 1% wt and 1:10 parts of ethanol are added to be able to kept the electrolyte under negative temperature values, concretely -5ºC. A first step anodization starting with a voltage of 175 V during 180 minutes is performed followed by a sequential increase of the voltage (also called ramp) for about 0,05 V/s until the voltage reaches the top potential limit of 195 V. All these parameters are summarized in **Table 3.1.** Then the anodization is kept in this value over minimum 20 to 24 hours to obtain ordered pores at the bottom of the growing layer. Once those ordered pores have been obtained, the grown layer is removed using the *orange solution procedure* previously mentioned, and a second anodizing step is performed. The second step anodization is controlled by total charge instead of time as it is better to control the layer thickness by this parameter and is performed using the same parameters (voltage) as we have used in the first step.

3.3.2. Hard Anodization

As it has been already explained in chapter 2, Hard Anodization (HA) are the ones using voltages over the breakdown potentials. For every electrolyte (phosphoric, oxalic or sulphuric acids) there is a potential limit (named breakdown potential) above witch the anodization triggers to local thickening, burning and cracking of the growing oxide. These potential limits are 27, 50 and 197 V for sulphuric, oxalic and phosphoric acid respectively. According to the literature this break down of the anodic oxide occurs due to the local current flow and the resulting Joule heating [10–12]. It has been also observed that the higher ordering is found using potentials just under the breakdown value. The current density (J) in Hard Anodization process is one or two orders of magnitude higher than Mild Anodization (MA) [13]. The Joule's

heat is two to four orders of magnitude bigger than the MA. That means that this heat have to be appropriately dissipated otherwise the growing anodic oxide will suffer a breakdown [14].

For all this reasons the Nanoporous Anodic Alumina formed by this HA in industrial procedures is not suitable for research due to the non-uniform pores and local brakdowns in the anodic oxide.

3.3.3. Calibration Pore Growth

It has been mentioned, mild anodization is providing uniform layers grow. For this reason it can be thought that a calibration curve can be elucidated using cross-section images and the time needed to grow them (**Figure 3.7**).

Actually, this calibration curve can show a good approximation but it has several drawbacks:

The images of the sample cross-section need to be taken perpendicularly and without defects otherwise error measurements can be obtained.

This calibration curve will only be reliable when the anodization parameters (voltage, electrolyte composition and temperature) are the same and constant through all the experiments. That means that, it is needed a new calibration curve for every electrolyte specie or concentration. And a new calibration is required if the voltage or temperature is altered.

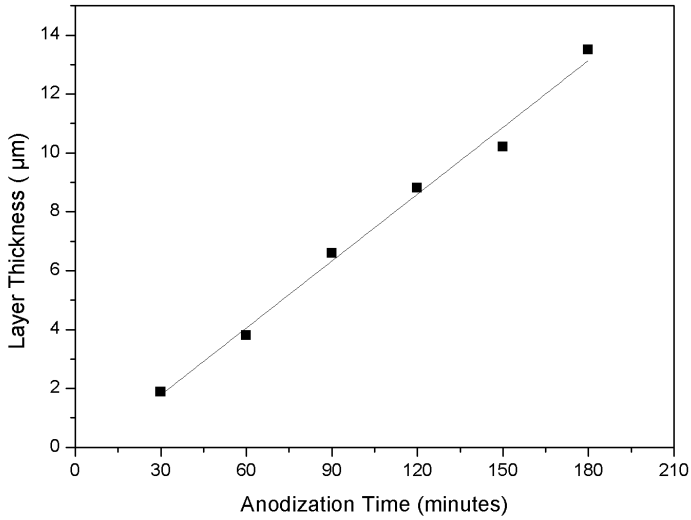

Figure 3.7. Calibration curve relating the anodization time (t) and layer thickness (L) for an oxalic acid anodization.

The equation relating the Anodization time and layer thickness (fitting) in the given example (**figure 3.7.**) is the one presented in (**equation 3.1**):

$$L = (0{,}075t) - 0{,}49 \qquad (3.1)$$

Where L is the Layer Thickness in nanometers and t is the anodization time in minutes.

For all the reasons presented a total electrical current charge (Q) calibration have been performed to better estimate the growing layer thickness. This total charge calibration is based on the fact that the anodization of aluminium is mainly governed by the migration of ionic

species to the respective electrodes, and the resulting current developed in the electrochemical cell during the anodization process is directly proportional to the amount of alumina generated. For that reason, the calibration using the total charge is independent of the voltage, electrolyte composition and temperature, because the total charge passed through the electrodes is telling the amount of Nanoporous Anodic Alumina created regardless the anodization parameters. For this reason calibrations using the total charge are the ones used to control the layer length of the growing oxide in our research facilities [2]. A calibration example is shown in **figure 3.8.**

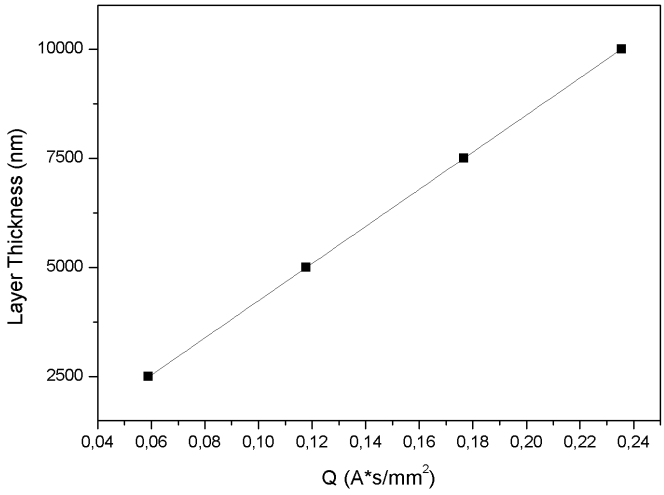

Figure 3.8. Graph showing the calibration (linear relation) between Q (total charge) and the oxide layer thickness.

The expression to relate the total electrical current charge (Q) and the layer thickness is the following equation:

$$Q = \frac{L+10{,}877}{42509*Z} \quad (3.2)$$

Where Q is the total charge in Coulombs (C) or Amperes per second (A*s), L is the layer thickness in (nm) and Z is the area of the sample anodized in millimetres squared (mm^2).

Once the calibration is performed a system is used to calculate the total electrical current charge of the anodization process (current passed through the system) in real time. Then the process (anodization) is stopped when the target value of Q is reached.

3.4.Post-treatments

3.4.1. Pore Widening

The most common technique to achieve different porosities in the already anodized Nanoporous Anodic Alumina is by wet chemical etching in phosphoric acid [15]. This post-treatment allows good control over pore diameter and is easily calibrated by image analysis of SEM top images. In addition it allows the increase of the pore diameter without interfering on the interpore distance. It consists on immersing the anodized samples into a phosphoric acid solution of 5% wt concentration at 35ºC during a controlled period of time. This acid will dissolve the pore aluminium oxide walls. **Figure 3.9** is showing images took for different pore widening times in samples anodized using phosphoric acid.

It has been proven that the voltage applied during the anodization will affect the pore diameter. This is because low voltages

are generating smaller interpore distances and thinner pore walls [16]. As a result of this reduction, the porosity will be rapidly increased by the pore widening post-treatment, compared to pores with larger walls (higher voltages) [17]. In addition, the anodization voltage also has a direct relation with the electrolyte anions (impurities) added in the oxide layer. It was proven by comparing samples anodized in Mild (MA) and Hard (HA) anodization conditions [13]. Actually, the incorporation of acid anions occurs via inwards migrations under an electric field during the anodization. The amount of incorporated acid anions and their spatial distribution in the nanoporous anodic alumina depend on the type and concentration of electrolytes, anodizing potential, current density and temperature. This incorporated electrolyte anions influence the chemical, optical and mechanical properties of the aluminium oxide [14].

The pore wall exhibits a duplex structure in terms of chemical composition mentioned in chapter 1. The outer oxide layer next to the pores is contaminated with electrolyte anions and the inner oxide is pure with a anion gradient separating them. This duplex nature of the pore wall oxide can be evidenced by pore widening experiments: different pore-widening/dissolution rates can be found with an inflexion point (**Figure 3.10**) showing where the composition of the pore wall is changing [18].

Hence, the electrolyte concentration, anodizing potential, current density and temperature have a direct relation on the impurities in the oxide and those impurities on the pore widening rate. That means, that

pore-widening rate depends on the anodization parameters, for example smaller voltages gives bigger dissolution rates.

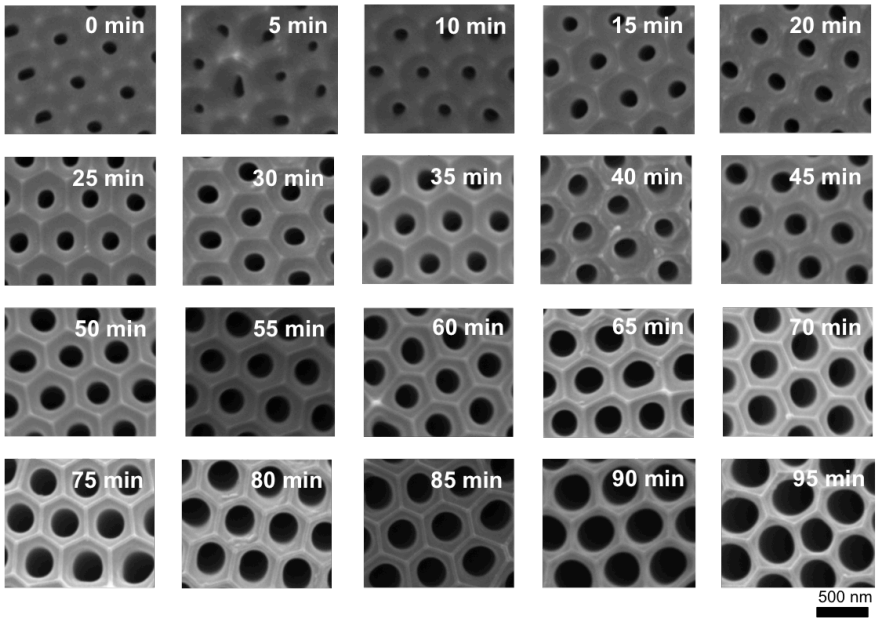

Figure 3.9. Pore widening sequence on samples produced by anodization using phosphoric acid. Time written in every photo is showing the pore widening times for every sample.

3.4.2. Pore Opening

Once strait, uniform and parallel nanochanels can be appreciated the pore opening procedure can be performed. These nanochanels are truncated at the end by an hemispherical cap of dense non-porous alumina layer (the barrier layer). To obtain nanoporous anodic alumina membranes (open by both sides) this barrier layer can be removed by several techniques. The most widely used method to remove the oxide barrier layer from the pore bottom tips involves the dissolution of the Al substrate, that is remaining in the bottom of the sample, in a

mixture of $CuCl_2$-HCl (saturated) and 68% HNO_3. Once the Al_2O_3 (barrier layer) is reached, a phosphoric acid solution of 5% wt at 35ºC can be used to dissolve the Al_2O_3. The NAA is settled on the top of the acid surface, with the bottom part (barrier layer) facing down and in contact with the acid. The etching time will depend on the thickness of the oxide barrier layer and therefore on the anodization conditions (see chapter 2). This wet chemical etching tecknique is very irregular since the pore opening is non-uniform and the etching rate is difficult to control. In addition the pore diameter enlarges slightly because the acid solution penetrates into the pores. For this reason other methods like reactive-ion etching (RIE) are useful in order to achieve a uniform opened membrane [19].

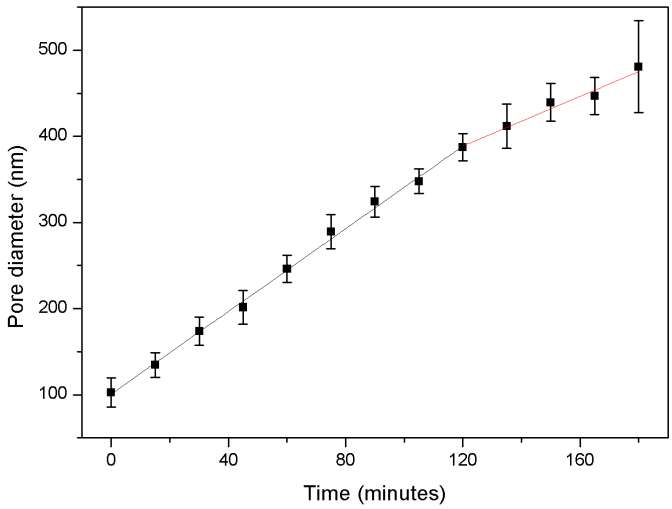

Figure 3.10. Pore widening calibration on phosphoric acid samples. An inflection point can be observed after 2 hours.

3.4.3. Annealing

Aluminium oxide pore walls prepared by electrochemical anodization are amorphous and contaminated with different amounts of anions derived from acid electrolyte. It has been proven that temperature treatment (annealing) can convert amorphous oxide membranes to polycrystalline [10, 8]. This crystallization gives resistance to the pore widening treatment. There is a relation between the temperature, the crystallization and the pore widening resistance. The higher the temperature the bigger the pore widening resistance.

3.5. New Pore Architectures

New pore architectures can be performed using both post-treatments presented in the last section and acid anodizations.

3.5.1. Normal Funnels-like Pores

Those samples can be done by sequential anodization and pore widening treatments [15]. An anodization for a determined layer length is done followed by pore widening procedure for a controlled time. Both processes should be calibrated before. Then another anodization can be performed resulting on samples with two different pore diameters. More layers with different pore longitudes can be made by alternating anodization and pore widening (**Figure 3.11**).

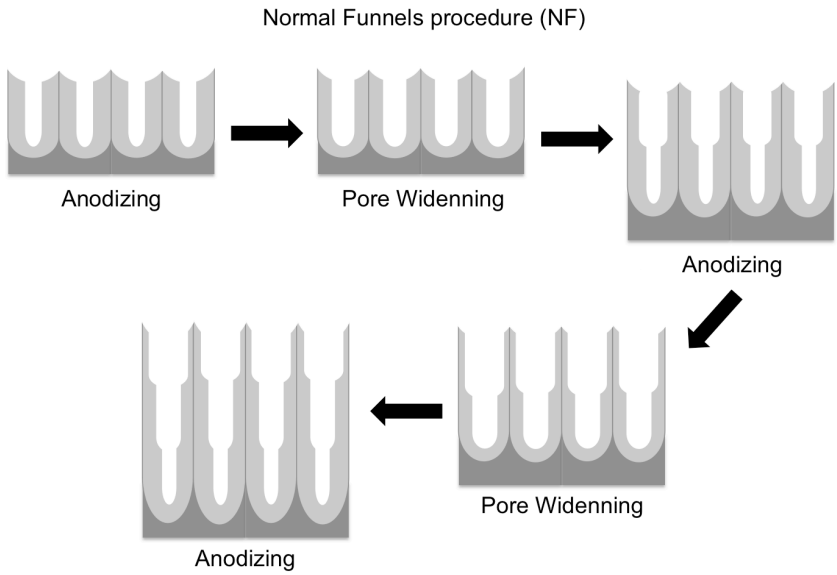

Figure 3.11. Schematics showing the Normal Funnels fabrication procedure.

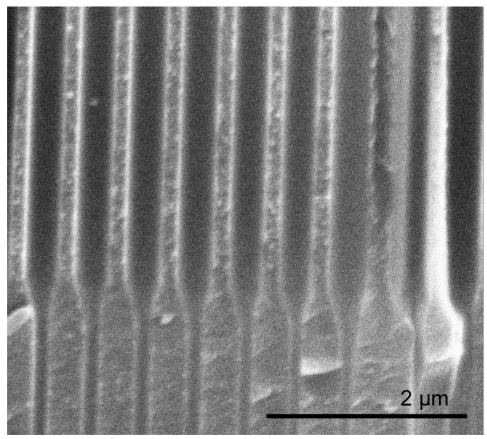

Figure 3.12. ESEM photo of Normal Funnel pores achieved using the described method.

3.5.2. Inverted Funnels-like Pores

Inverted nanoporous anodic alumina funnels are fabricated by an electrochemical approach based on the differential dissolution rate of nanoporous anodic alumina with the annealing temperature [20,21]. Then, alternating anodization with annealing and using pore widening at the end, inverted funnels can be performed (**Figure 3.12**).

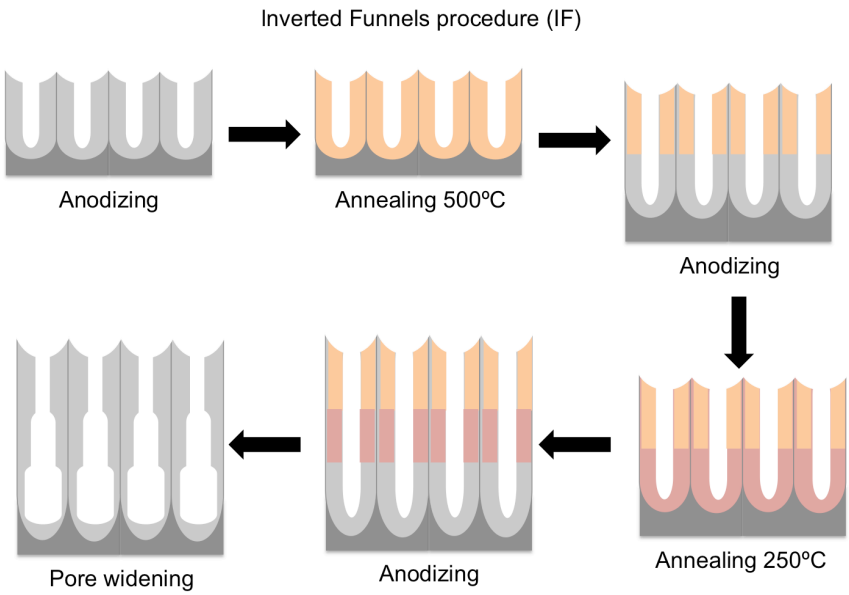

Figure 3.13. Schematics showing the Inverted funnels fabrication procedure.

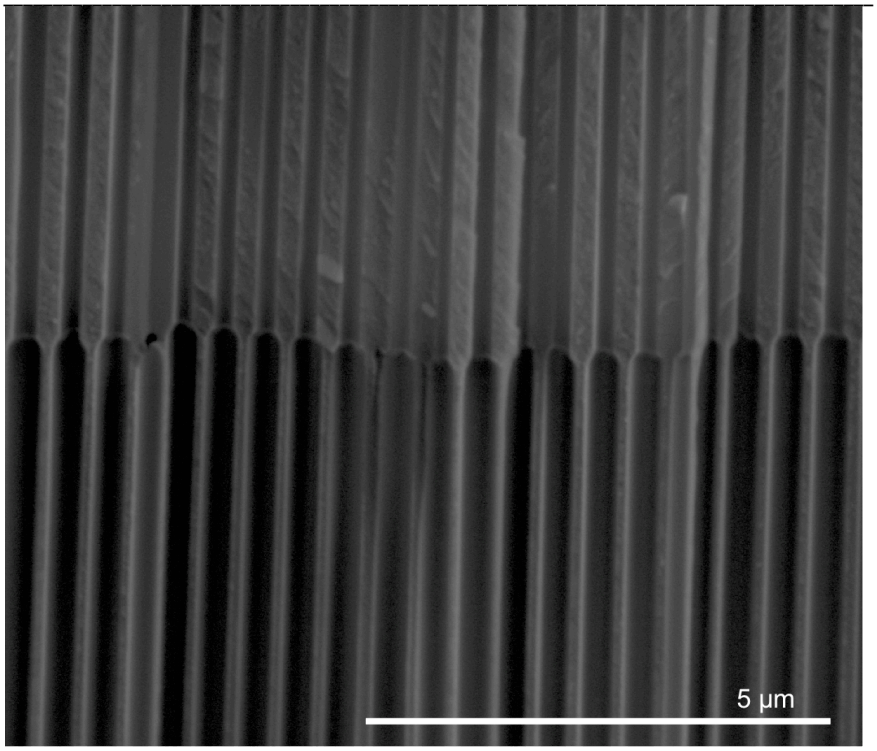

Figure 3.14. ESEM photo of Inverted funnel-like pores achieved using the already mentioned procedure.

3.6. Summary

This chapter has described the laboratory equipment for fabricating nanoporous anodic alumina and the detailed procedures that we use for this achievement. We have provided a complete explanation of the electrochemical cell, the software and the aluminium substrate. We also have reported the pre-treatments that can be performed before the electrochemical anodization. We also have exhaustively clarified the different typologies of anodizations we have performed. We also talked about the possible post-treatments that can be performed in the NAA in order to change its features. Finally we have carefully described the

funnels like pore architectures anodization method for both: normal funnels and inverted funnels.

3.7. References

1. Santos A, Vojkuvka L, Alba M, et al. (2012) Understanding and morphology control of pore modulations in nanoporous anodic alumina by discontinuous anodization. Phys Status Solidi a-Applications Mater Sci 209:2045–2048. doi: 10.1002/pssa.201228150
2. Santos A, Montero-moreno JM, Bachmann J, et al. (2011) Understanding Pore Rearrangement during Mild to Hard Transition in Bilayered Porous Anodic Alumina Membranes. ACS Appl Mater Interfaces 1925–1932. doi: 10.1021/am200139k
3. Santos A, Vojkuvka L, Alba M, et al. (2012) Understanding and morphology control of pore modulations in nanoporous anodic alumina by discontinuous anodization. Phys Status Solidi Appl Mater Sci 209:2045–2048. doi: 10.1002/pssa.201228150
4. Masuda H, Fukuda K (1995) Ordered Metal Nanohole Arrays Made by a Two-Step Replication of Honeycomb Structures of Anodic Alumina. Science (80-) 268:1466–1468. doi: 10.1126/science.268.5216.1466
5. Nielsch K, Choi J, Schwirn K, et al. (2002) Self-ordering Regimes of Porous Alumina: The 10 Porosity Rule. Nano Lett 2:677–680. doi: 10.1021/nl025537k
6. Santos A, Alba M, Rahman MM, et al. (2012) Structural tuning of photoluminescence in nanoporous anodic alumina by hard anodization in oxalic and malonic acids. Nanoscale Res Lett 7:228. doi: 10.1186/1556-276X-7-228

7. Takahashi H, Nagayama M (1978) The determination of the porosity of anodic oxide films on aluminium by the pore-filling method*. Corros Sci 18:911–925.
8. Marsal LF, Vojkuvka L, Formentin P, et al. (2009) Fabrication and optical characterization of nanoporous alumina films annealed at different temperatures. Opt Mater (Amst) 31:860–864. doi: 10.1016/j.optmat.2008.09.008
9. Zaraska L, Sulka GD, Jaskula M (2011) Anodic alumina membranes with defined pore diameters and thicknesses obtained by adjusting the anodizing duration and pore opening/widening time. J Solid State Electrochem 15:2427–2436. doi: 10.1007/s10008-011-1471-z
10. Lee W, Park S-JSS (2014) Porous anodic aluminum oxide: anodization and templated synthesis of functional nanostructures. Chem Rev 114:7487–7556. doi: 10.1021/cr500002z
11. Ikonopisov A, Girginov A, Machkova M (1977) Post-breakdown anodization of aluminum. Electrochim Acta 22:1283–1286.
12. Chu SZ, Wada K, Inoue S, et al. (2006) Large-Scale Fabrication of Ordered Nanoporous Alumina Films with Arbitrary Pore Intervals by Critical-Potential. 384–391. doi: 10.1149/1.2218822
13. Lee W, Ji R, Gösele U, Nielsch K (2006) Fast fabrication of long-range ordered porous alumina membranes by hard anodization. Nat Mater 5:741–747. doi: 10.1038/nmat1717
14. Losic D, Santos A (2015) Nanoporous Alumina : Fabrication, Structure, Properties and Applications. doi: 10.1007/978-3-319-20334-8
15. Santos A, Formentín P, Pallarès J, et al. (2011) Structural engineering of nanoporous anodic alumina funnels with high aspect ratio. J Electroanal Chem 655:73–78. doi: 10.1016/j.jelechem.2011.02.005

16. Shuoshuo C, Zhiyuan L, Xing H, Yi L (2009) Controlled growth of branched channels by a factor of 1 / O n anodizing voltage ? J Mater Chem 19:5717–5719. doi: 10.1039/b908815f
17. Rahman MM, Garcia-caurel E, Santos A, et al. (2012) Effect of the anodization voltage on the pore-widening rate of nanoporous anodic alumina. Nanoscale Res Lett 7:1–7. doi: 10.1186/1556-276X-7-474
18. Han H, Park SJ, Jang JS, et al. (2013) In situ determination of the pore opening point during wet-chemical etching of the barrier layer of porous anodic aluminum oxide: Nonuniform Impurity Distribution in Anodic Oxide. ACS Appl Mater Interfaces 5:3441–3448. doi: 10.1021/am400520d
19. Eckstein C, Xifré-pérez E, Porta-i-Batalla M, et al. (2016) Optical monitoring of capillary filling dynamics variation in nanoporous anodic alumina towards sensing applications. Langmuir 32:10467–10472. doi: 10.1021/acs.langmuir.6b02459
20. Santos A, Kumeria T, Wang Y, Losic D (2014) Insitu monitored engineering of inverted nanoporous anodic alumina funnels: on the precise generation of 3D optical nanostructures. Nanoscale 6:9991–9999. doi: 10.1039/c4nr01422g
21. Porta-i-Batalla M, Xifré-Pérez E, Eckstein C, et al. (2017) 3D nanoporous anodic alumina structures for sustained drug release. Nanomaterials 7:227. doi: 10.3390/nano7080227

UNIVERSITAT ROVIRA I VIRGILI
DEVELOPMENT OF NANOPOROUS ANODIC ALUMINA TECHNOLOGIES FOR DRUG DELIVERY
Maria Porta Batalla

Chapter 4

Drug Release based on Nanoporous Anodic Alumina with Layer-By-Layer Polyelectrolyte

UNIVERSITAT ROVIRA I VIRGILI
DEVELOPMENT OF NANOPOROUS ANODIC ALUMINA TECHNOLOGIES FOR DRUG DELIVERY
Maria Porta Batalla

Controlled drug delivery systems are an encouraging solution to some drug disadvantages such as reduced solubility, deprived biodistribution, tissue damage, fast breakdown of the drug, cytotoxicity or side effects. Self-ordered nanoporous anodic alumina is an auspicious material for drug delivery due to its biocompatibility, stability and controllable pore geometry. Its use in drug delivery applications has been explored in several fields, including: therapeutic devices for bone and dental tissue engineering, coronary stent implants and carriers for transplanted cells.

In this chapter we are presenting and analysing a stimuli-responsive drug-delivery system based on Nanoporous Anodic Alumina coated with layer by layer pH-responsive polyelectrolyte.

4.1.Introduction

Vast majority of the existing drugs are hydrophobic, that means they cannot dissolve in a fluid like blood. This diminishes their pharmacological efficacy. In addition, some bioactive agents such as proteins, nucleic acids or enzymes administered though oral or intravenous routes can be easily corrupted by metabolism or by enzymatic conditions and are unable to reach the desired sites in optimum conditions [1–3]. The expansion of the understanding about materials at the nanoscale may accelerate the development of drug delivery systems, especially in healing life-threatening conditions such as cancer and heart disease.

Nanoporous and nanotube carriers with their distinctive features such as low cost fabrication, controllable pore/nanotube structure, tailored surface chemistry, high surface area, high loading capability, chemical resistivity and mechanical rigidity, have affianced a special role in drug delivery technology. Drug release is a procedure in which a composite or a device releases a drug in a controlled way and is subjected to absorption, distribution, metabolism and excretion (ADME), finally becoming available for pharmacological action. To accomplish and preserve therapeutically effective plasma concentrations, several doses can be needed daily, which may cause substantial oscillations in plasma levels. Because of these oscillations in drug plasma levels, the drug concentration could fall below the minimum effective concentration or exceed the minimum toxic concentration. Such fluctuations result in unwanted side effects or absence of therapeutic profit to the patient.

Sustained-release and controlled-release drug delivery systems can diminish the undesired oscillations of drug levels, consequently reducing side effects while improving the therapeutic result of the drug. The terminologies sustained-release and controlled-release refer to two different kinds of drug delivery systems (DDS), although they are frequently used as indistinct terms:

Sustained-release dosage forms are systems that extend the duration of the action by decreasing the release of the drug, and its pharmacological action.

Controlled-release drug systems are more complex than just merely delaying the release rate and are designed to deliver the drug at specific release rate within a predetermined time period.

Advantages of controlled-release DDS involve delivery of a drug to the required site, preservation of drug levels within a desired range, diminished side effects, less administrations, and improved patient compliance.

The evolution of delivery systems leads to stimuli-responsive DDS. Whose behaviour can be dependent on the environment features where it is placed. Recently the pH-responsive controlled drug delivery systems have attracted significant attention, due to the acidic tumoral atmosphere of most cancers and the acidic environment of wounds [4]. In this chapter, we suggest a DDS that can be defined as sustained, controlled and stimuli-responsive release system due to its capabilities

to release the drug in a required rate and responding to pH changing incentives.

The DDS we suggest is created with nanoporous anodic alumina (NAA). It was not until 1990s that investigators discovered that highly ordered nanoporous arrangements can be achieved by correctly modifying anodization conditions involving electrolyte composition and concentration, temperature, as well as anodization voltage [5].

Several reports have been already presented in the drug delivery framework using porous materials [6–8]. Nanoporous anodic alumina is one of the most attractive materials for drug delivery applications since it is simple and low-cost fabrication. Regulating the anodizing voltage, time and electrolyte composition can easily control the pore size and depth. Additional outstanding properties of this material are the chemical and thermal stability, hardness, high surface and highly ordered pore structure [9, 10].

Specific applications of NAA are to rebuild or regenerate living tissues, deal with infections, and inflammation as consequence of surgical implantation or just for drug continuous administration [11].

Drug depots in human organism with controlled and retained release are capable to contribute in long-term treatments and, this way, improve quality of life. Moreover the development of those new and more efficient drug delivery systems resolve conventional drug therapy troubles related to limited drug solubility, lack of selectivity and unfavourable pharmacokinetics.

The organization of NAA can be defined at a close-packed hexagonal and perpendicular orientated array of columnar cells, each containing a central pore. Changing the anodization conditions we can control the size and interval of the pores. The drug discharge or release from porous materials is based on molecular diffusion from the pores, and it is mainly directed by the pore dimensions [12]. Therefore, adjustment of pore diameter and pore depth has also been considered a common strategy to control drug release.

In this chapter, NAA scaffolds with pore diameters about 130 nm and pore depth of 15 μm were used as model porous material. In order to perform a controlled drug release, a pH stimuli-responsive polyelectrolyte LbL assembly has been used to coat the porous scaffolds. Doxorubicin (DOX), a strong antineoplasic agent against a extensive range of human tumors, was selected as a model drug to accomplish the tests. The polyelectrolyte multilayer on the surface avoids the premature release of the drug and allows the use of the total enhanced surface in the NAA samples. The effect of pH in the drug release kinetics has been reviewed and examined as well as the effect of the polyelectrolyte bilayer number.

4.2. Methodology

4.2.1. Nanoporous Alumina Anodization

Well-arranged nanoporous anodic alumina was produced by the two-step anodization method (**Figure 4.1**) [13–15].

Aluminium substrates were degreased in acetone and ethanol to remove organic impurities. They were then subsequently electropolished (**Figure 4.1A**) in a mixed solvent of perchloric acid and ethanol (1:3) at a constant applied voltage of 20V for 6 minutes. Then in order to suppress breakdown effects and to enable uniform oxide film growth at high voltage (195V in phosphoric acid) a protective layer at lower voltages (175 V in phosphoric acid) for 180 minutes was performed. In order to have a more precise control of the anodization process in this work, the voltage and current of the anodization process were monitored and recorded by DSM (SM 300-5) SourceMeter, controlled by a home-built computer program based on LabView.

Once this pre-anodization at 175 V was performed, a ramp of 0,05 V/s was used to reach the hard anodization voltage (195 V) throughout 24 hours. The voltage was augmented in a linear manner, so that the current will not increase too fast in order to avoid overheating of the electrolyte and the subsequent oxide breakdown.

After the ramping process is done, the program maintains the target voltage at the same time it is observed that the anodization current falls naturally down to a stable level, which is an indication of inception of stable anodization. This first anodization produces an alumina scaffold that is ordered at the bottom but presents disordered features at the top part of the pores (**Figure 4.1B**).

Then, after this first step, the porous alumina grown on the aluminium surface was removed by a wet chemical etching in a mixture

of phosphoric acid (0,4 M) and chromic acid (0,2 M) (1:1 volume ratio) at 70ºC (**Figure 4.1C)** leaving a highly periodic structure of nano-concavities which forms the initiation sites for the formation of pores in the second anodization step [16–19].

At that time a second anodization was performed under the same experimental conditions (195 V) as in the first step in order to obtain ordered nanoporous alumina. The second step anodization was applied until pores with 15 μm depth were obtained (**Figure 4.1D**).

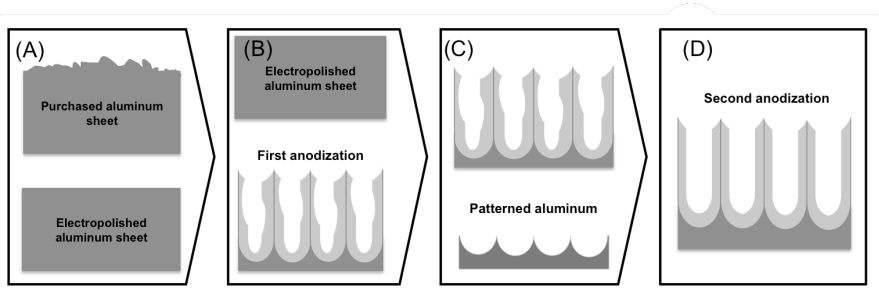

Figure 4.1. Schematic representation of the alumina pores formation during the anodization process. A) The electopolishing procedure creates a plane surface. B) The first anodization produces a disordered NAA wall. C) Dissolution of the alumina wall creates an ordered pattern in the aluminium sheet. D) The second anodization on the patterned aluminium creates a perfect ordered NAA.

4.2.2. Polyelectrolytes Assembly

For the purpose of covering the nanopore walls with polyelectrolyte layers, nanoporous anodic alumina was first coated with 3-aminopropyl triethoxysilane (APTES). The positively charged APTES substrates would allow negatively charged polyelectrolytes to be

attached to the pore walls (**Figure 4.2A**). For LbL deposition, the NAA substrates were dipped consecutively into negative charged solution of poly(styrenesulfonate) (PSS, 1 mg/ml in 5 mM CaCl2 in deionized water) (**Figure 4.2B**), and positive charged solution of poly(allylamine hydrocloride) (PAH, 1 mg/ml in 5 mM CaCl2 in deionized water)(**Figure 4.2C**), alternating rinsing with deionized water between each immersion. Dipping times in polyelectrolyte solutions were 30 minutes and the washing step in deionized water lasted for 10 min [20]. All the steps were repeated for 2, 5 and 8 times for obtaining 2 bilayers, 5 bilayers and 8 bilayers respectively.

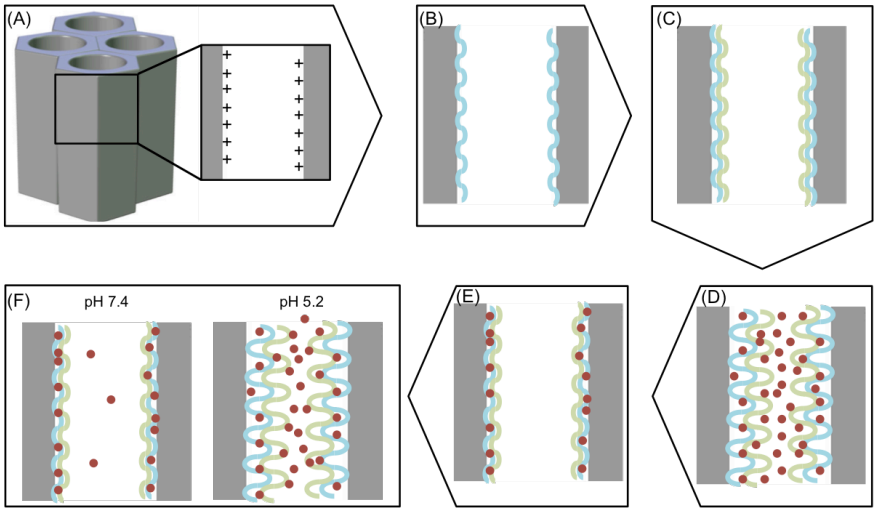

Figure 4.2. Schematic representation of the polyelectrolyte layer-by-layer deposition procedure. B) PSS deposition by immersing the APTES treated surface. C) PAH deposition by immersing the PSS covered substrate. D) DOX loading in the swollen PEM film at pH 2.0 E) DOX confinement due to the PEM layer contraction at pH 8.0 F) DOX releases at different pH media.

4.2.3. Drug Loading

Positively charged doxorubicin (DOX) was chosen as a model drug. DOX is a potent anti-tumoral agent that is widely employed for the purpose of the cancer therapy with good fluorescence characteristics [21].

Layer by layer (LbL) NAA samples were dipped in 1 mg/ml DOX solution at pH 2 in the dark at room temperature overnight (**Figure 4.2D**). Then the DOX solution was adjusted to pH 8 and the samples were stirred 2 hours in the dark (**Figure 4.2E**). Subsequently, samples were washed with deionized water adjusted at pH 8.

At pH 2, the increased permeability of the polyelectrolytes film facilitates the incorporation of DOX inside the PSS/PAH multilayers. Then the modification of pH at 8 causes the contraction of the polyelectrolytes and the drug molecule becomes trapped inside the polyelectrolyte film. The following washing will remove any nontrapped DOX molecule.

4.2.4. Drug release

Samples under analysis were immersed in phosphate buffered saline (PBS) at pH 7.4 and sodium acetate buffer at pH 5.2 (**Figure 4.2F**). Samples were immersed in 0.5 ml of the corresponding medium and this medium was renewed at every measurement.

Release characteristics depending on the number of polyelectrolyte layers and on the pH of the release medium were observed.

Release trials consisted of monitoring the diffusion of doxorubicin (DOX) as a function of time after the encapsulation within the polyelectrolytes coating. For this reason fluorescence of the buffers solutions were measured at regular time intervals.

We toked the photoluminescence measurements on a fluorescence spectrophotometer with a Xe lamp used as the excitation light source at room temperature and with an excitation wavelength of 480 nm. A calibration curve to relate the photoluminescence values and the DOX concentration was also needed.

Drug release was monitored by drug photoluminescence over 7200 minutes (120 hours) in 2 different pH buffer mediums: pH 5.2 and pH 7.4. Once we reached 2880 minutes (48 hours) samples immersed in pH 7.4 medium were changed to pH 5.2 medium.

Intensities of the fluorescent peaks were converted to the corresponding concentrations using the already mentiones calibration curve. Release rates are reported as $\mu g/cm^2$ vs. time.

4.3. Results and Discussion

Figure 4.3 shows Environmental Scanning Electron Microscopy (ESEM) images of one of the fabricated NAA samples. **Figure 4.4** shows an schematic drawing of the porous structure. The morphologies of the NAA substrates were characterized by Environmental Scanning Electron Microscopy (ESEM FEI Quanta 600, Hillsboro, OR, USA).

The top surface view in **Figure 4.3A** reveals a good ordering in a honeycomb structure of the pores in the short range, with good pore distribution. At the same time, the cross-section image in **Figure 4.3B** demonstrates straight and parallel growth of the pores.

Image examination results in estimated average pore diameter (D_p) value of 130 nm, layer length (L) of 15 μm and interpore distance (D_{int}) of 480 nm. The schematic drawing in **Figure 4.4** illustrates the definition of these magnitudes.

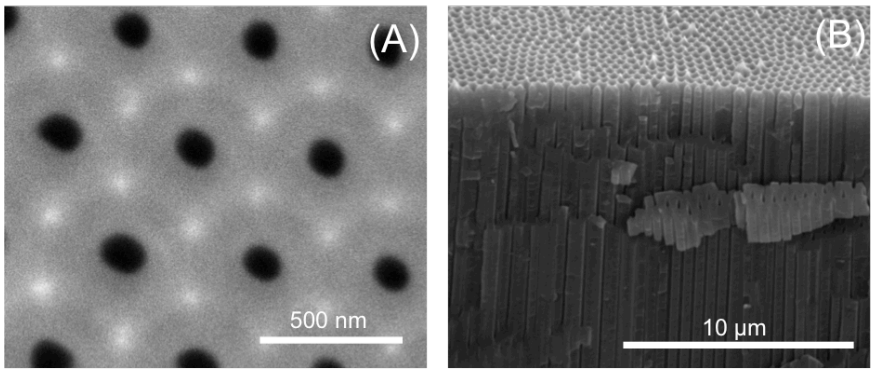

Figure 4.3. A)Top-view ESEM image of NAA. B) Cross-sectional SEM image of imprint NAA

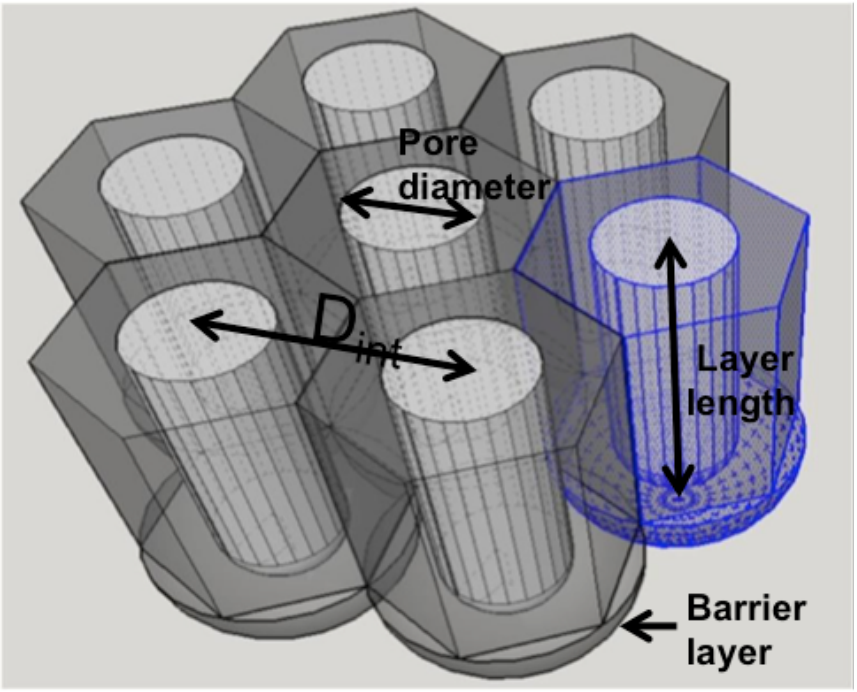

Figure 4.4. Schematic representation of the alumina pores forming a close-packed hexagonal and perpendicular orientated array of columnar cells.

Figure 4.5 shows ESEM images of the top surface of a NAA sample after different stages in the PSS/PAH deposition, in order to validate/check the successful deposition of the polyelectrolyte multilayer.

Figure 4.5A corresponds to an as-produced sample (without any polyelectrolyte layer). **Figure 4.5B** corresponds to a sample after the deposition of two polyelectrolytes bilayer. And finally **Figure 4.5C** corresponds to a sample after the deposition of 8 polyelectrolytes

bilayer. A statistical estimation of pore diameters using image-processing techniques was carried out. The images do not show a perceptible change in pore diameter

Figure 4.6 show the pore size distribution for non treated samples (**figure 4.6.A**), with two bilayers deposition (**figure 4.6.B**) and with eight bilayers deposition (**figure 4.6.C**). Mean values and standard deviation for pore measurements are shown in **table 4.1**.

This statistical estimation results in an average pore radius of 131-130 nm for the samples without polyelectrolyte layers and the samples with polyelectrolyte respectively with a standard deviation of 12 nm. It can be confirmed in **Figures 4.6A-C**.

The only indication from the pictures that the surface is being appropriately modified is that the image contrast increases with the number of bilayers. Hence, it can be assumed that there is a polyelectrolyte layer recovering the sample surface.

In order to check satisfactory infiltration and polyelectrolyte coating in the inner pore surfaces, we imaged a cross-section of the nanopores before and after coating with polyelectrolytes and we obtained the Energy Dispersive X-ray Spectroscopy (EDX) spectra shown in **Figures 4.7A** and **4.7B**.

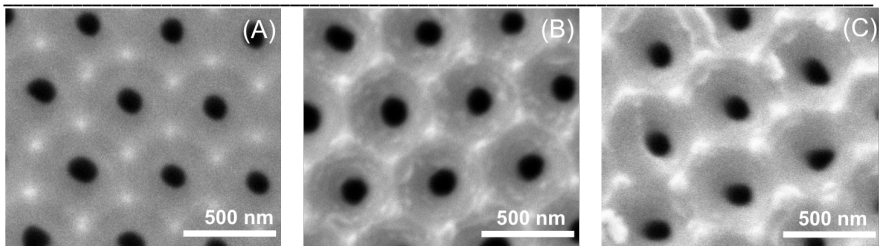

Figure 4.5. Environmental Scanning Electron Microscope images of the top views, A) without polyelectrolyte coat B) whit 2 polyelectrolyte bilayers C) with 8 polyelectrolyte bilayers.

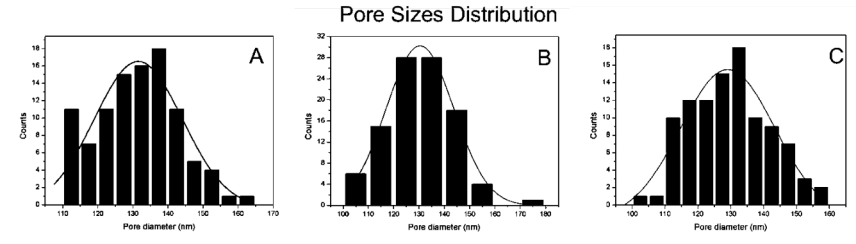

Figure 4.6. Shows the pore diameter distribution for different number of bilayers: A) 0 bilayers B) 2 bilayers C) 8 bilayers

Table 4.1. shows mean pore diameter for samples without polyelectrolyte bilayers, with 2 polyelectrolyte bilayers and with 8 polyelectrolyte bilayers.

	Mean pore diameter (nm)	Standard deviation
0 bilayers	131	11,30
2 bilayers	130	12,70
8 bilayers	130	11,93

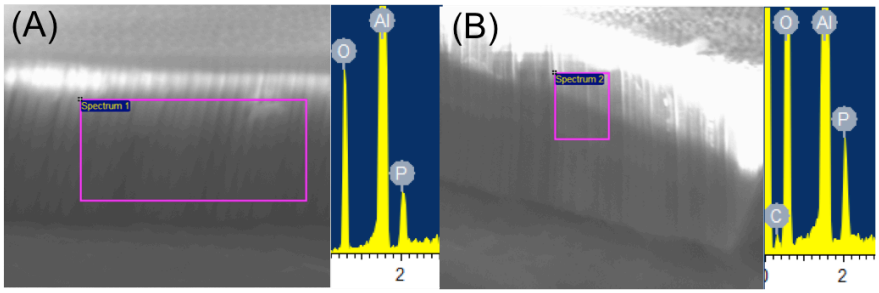

Figure 4.7. Correspond to the EDX measurements for cross-section samples without polyelectrolyte coating (A) and with polyelectrolyte coating (B).

Thanks to this technique (EDX) we can assume that no pore obstruction occurred during the LbL self-assembly.

The use of multivalent salt such as $CaCl_2$ contributes to the construction of the polyelectrolyte coat inside the nanopore owing to a stronger polymer-chain contraction [22, 23]. The following Energy Dispersive X-ray Spectroscopy (EDX) analysis of those samples shows phosphoric and aluminum peaks due to the sample and electrolyte presence, and also an oxygen peak because of the presence of this element in the alumina sample (Al_2O_3). However a carbon peak only appeared on those samples with polyelectrolytes (**Figure 4.7B**). That peak could not be found in the alumina samples without polyelectrolyte treatment (**Figure 4.7A**). This statement confirms the successful deposition and incorporation of both polyelectrolytes and DOX into the pores.

Afterwards the DOX loading, samples were exposed to different pH media to assess the pH responsiveness and the impact of the number of polyelectrolyte bilayers. For this purpose a calibration curve relating the DOX concentration and the Photoluminescence obtained (PL) was firstly performed (**Figure 4.8**).

When samples are in contact with the aqueous medium, the polyelectrolyte multilayer swells to a certain extent, increasing its permeability and allowing the diffusion of the drug.

This swelling phenomenon of PAH/PSS films is generally associated to the difference in charge density of polyelectrolyte chains stimulated by a change in the pH medium. PAH is a weak polyelectrolyte whose amino groups become charged when the pH decreases, creating an increase in the osmotic pressure. Consequently, water molecules diffuse into the polyelectrolytes and the multilayer swells.

This phenomenon, together with the electrostatic repulsion between DOX and PAH/PSS multilayer, enables the diffusion of the drug in the medium [24].

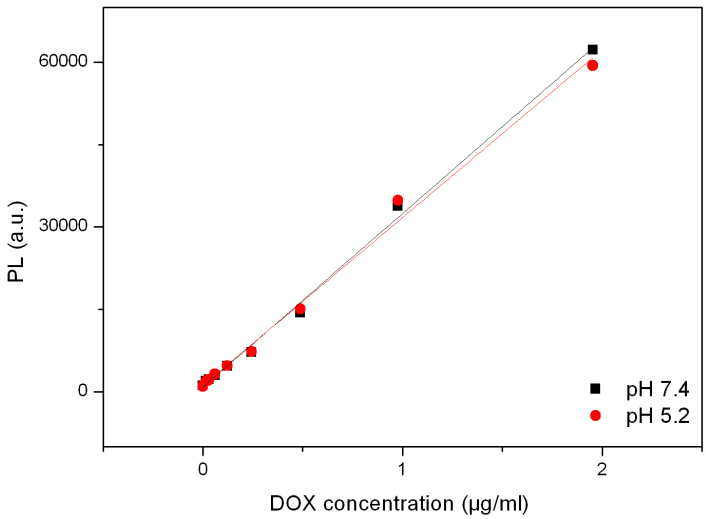

Figure 4.8. Calibration curve for different Doxorubicin concentrations and their Photoluminescence values.

Figure 4.9 compares the discharge profile of DOX from samples with different number of layers at pH 5.2 and pH 7.4 during a period of 3000 minutes. Two clusters of curves can bee seen: one group at pH 5.2 and another group at pH 7.4. Each group contains three different curves: 8 bilayers samples (circles), 5 bilayers samples (triangles) and 2 bilayers samples (squares).

Overall it can be accepted that there is a massive burst release in all curves (framed in the graph) within the first minutes. Once this first stage has occurred the release rate decrease causing a curve flattening.

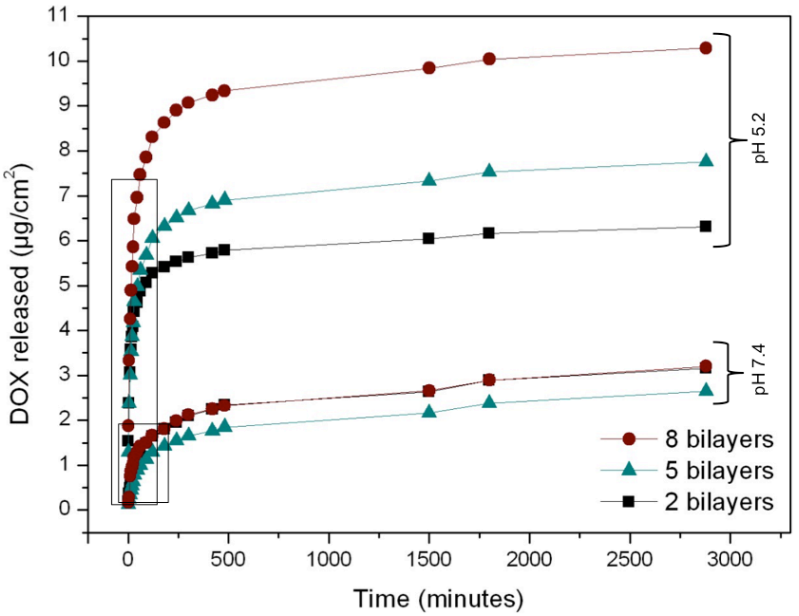

Figure 4.9. Doxorubicin (DOX) release profile for 3000 minutes at pH 5.2 and 7.4 for different numbers of polyelectrolyte bilayers and with the burst releases framed.

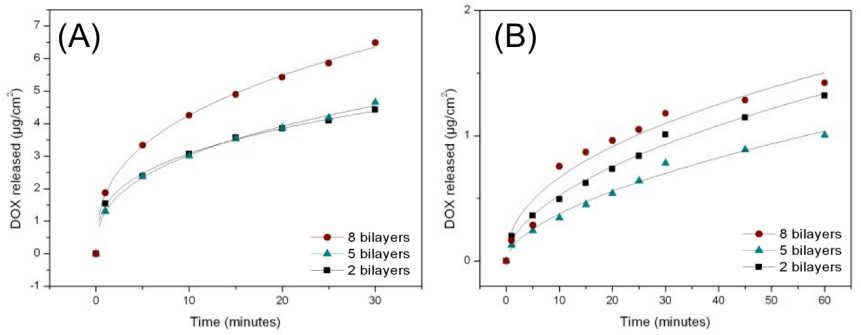

Figure 4.10 A) Nonlinear fitting for the burst release at pH 5.2. B) Nonlinear fitting for burst release at pH 7.4.

Figure 4.10A and **4.10B** shows a nearer look for the burst releases at pH 5.2 and 7.4 respectively. The data display that, as it was expected, burst release at pH 5.2 is faster than burst release at pH 7.4.

The results at pH 5.2 within the first 30 minutes (**Figure 4.10A**) show that the samples with 5 and 2 bilayers release nearly the same amount of drug, while for the 8 bilayer samples the release is 1.4 times bigger. After stabilization, at pH 5.2, the amount of released drug is bigger for bigger number of bilayers: samples with 8 bilayers release 1,32 times more drug than 5 bilayer samples and 1,63 times more than 2 bilayer samples.

Instead, at pH 7.4 the release dynamics is different: there is not a clear correspondence between the amount of released drug and the number of bilayers (**Figure 4.10B**), both in the burst and in the sustained release periods. These observed differences may occur due to the inhibition caused by the polyelectrolyte contraction.

Contemplating relative values, taking into account that 100% of the drug is the total amount of drug discharged at infinite time, the DOX released after 30 minutes for samples at pH 5.2 is between 4 and 5 times bigger than that at pH 7.4 (**Figure 4.11A**). This result is in accordance with the result in **figure 4.9**.

Besides the relative amount of released drug are not depending on bilayer number: 90% of the drug has been released during the first 24

hours at pH 5.2 while only 30-40% of the drug is released within first 24 hours at pH 7.4 (**Figure 4.11B**).

After that, release rate is reduced progressively until it shows a stabilized profile. It can be observed that at longer times the difference between relative released DOX at pH 7.4 and pH 5.2 is becoming lower. Since the release of the drug at pH 7.4 is slower, it is also more sustained during time. This is the reason why total amount of drug discharged at pH 5.2 and 7.4 are becoming nearer. **Figure 4.11C** shows a comparison between the total amounts of DOX at the finished release time for the different samples.

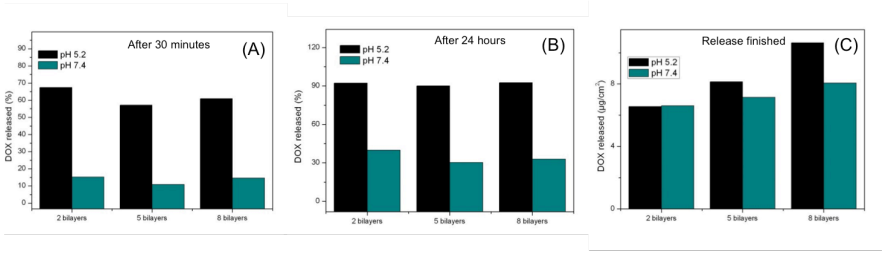

Figure 4.11. A) Percentage of the DOX released within the first 30 minutes at different pH and bilayer number. B) Percentage of the DOX released after 24 hours for different pH and bilayer number. C) Total DOX amount released for every different sample during the monitoring.

To continue with the experimentation, at minute 3000 samples immersed with medium at pH 7.4 were changed to pH 5.2 medium. This change in pH triggers another burst release really similar to the first burst release in samples at pH 5.2, which demonstrates that the DDS responds to pH modification. In **Figure 4.12** a general profile of the DOX release is shown in order to prove the responsiveness of the DDS to pH variation.

The quantity of drug released after the stabilization in the second burst release at pH 5.2 correlates with the number of bilayers. However, the absolute amount of DOX released in this second burst release is not reaching the same values of the first burst release at the same pH for all the samples.

Precisely for 2 bilayers, the second burst release (at pH 5.2) the DOX amount reaches the same value as for the previous release at pH 5.2. Contrarily, for 5 bilayers the total amount only reaches up to a 87,5% of the drug discharged in the previous experiment at pH 5.2. And for 8 bilayers this percentage is even lower (72,7%). These results can also be distinctively seen in **Figure 4.11C**.

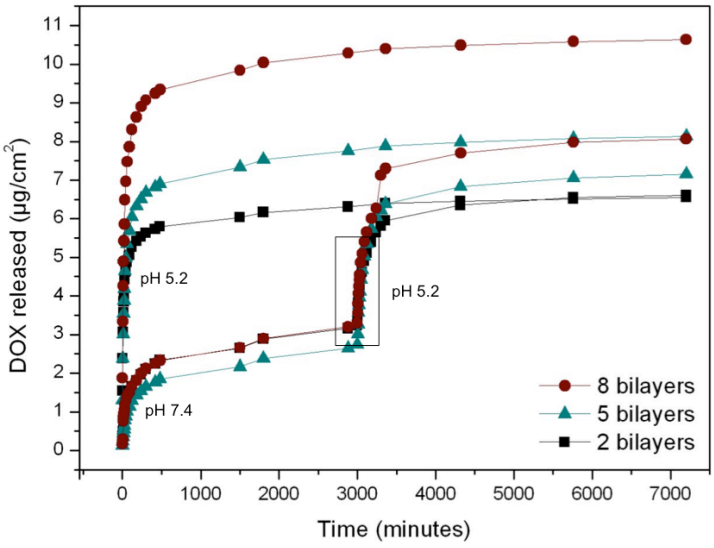

Figure 4.12. Complete release profiles of DOX from NAA coated with different polyelectrolyte bilayer numbers at pH 5.2 and 7.4. with the second burst release at pH 5.2 framed.

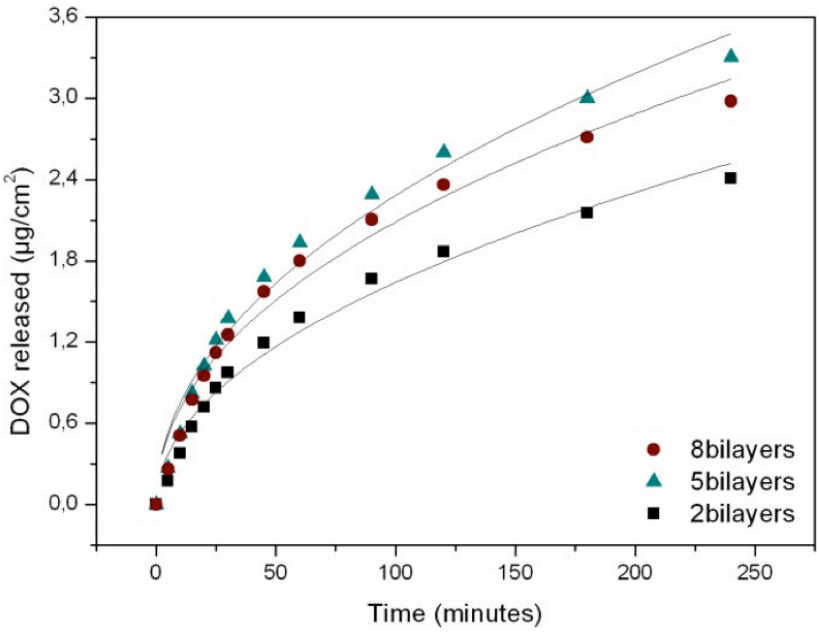

Figure 4.13. Nonlinear fitting for the second burst release at pH 5.2.

Figure 4.13 shows a exhaustive fitting for the second burst release at pH 5.2. In addition total amount of encapsulated DOX was also studied concluding that there is a proportionally direct relation between the polyelectrolyte number of bilayers and the amount of DOX loaded/released (**Figure 4.11C**).

This relation can be observed in both pH mediums, but becomes more obvious at pH 5.2 when DOX molecules can diffuse with fewer obstacles.

In order to present a quantitative analysis of the results during the early stage (burst release) we accomplished fitting studies of the curves by a adaptation of Higuchi and Ritger-Peppas models:

Higuchi model is an empirical model frequently used to define the release kinetics of drugs from insoluble porous materials [25, 26] It is well established and commonly used for modelling drug release from matrix systems [27, 28]. The Higuchi model is based on a square root of time-dependent process of Fickian diffusion [29, 30]. Fick's law of diffusion postulates the fundamentals for the description of solute transport from matrices [31].

Ritger-Peppas model (also known as Korsmeyer-Peppas) is used for fitting drug discharge from polymeric thin films, cylinders and spheres [32].

The equation we finally used is (**equation 4.1**):

$$M_t = M_{t_0}\left(\frac{t}{t_0}\right)^n \qquad (4.1)$$

Where M_t is the proportion of DOX released at a given time t, M_{t0} is the amount of released drug at the reference time t_0 (1 minute) t is time in minutes and n is a fitting parameter related to the release rate.

The adjustment process using a least squares method minimizes the differences between the experimental and theoretical values [33–35].

Several fittings using different time intervals were performed in order to be able to know the best option. **Table 4.2** is showing the R-squared values that were used to make the time selection. In this case 30 minutes was selected because the highest R-squared values were achieved within this interval.

The best fitting values for the equation parameters are shown in **Table 4.3**.

Table 4.2. shows different R-square for different fittings using different times.

		30 minutes	45 minutes	60 minutes	90 minutes	120 minutes
First Burst Release pH5.2	8 bilayers	0,99744	0,99351	0,99063	0,97674	0,97143
	5 bilayers	0,99716	0,99259	0,98948	0,97801	0,97505
	2 bilayers	0,99616	0,98601	0,97956	0,96166	0,95337

Table 4.3. Nonlinear fitting parameters for the different burst releases using the equation $M_t = M_{t_0}\left(\frac{t}{t_0}\right)^n$

		M_{t_0}	n	Release rate
First Burst Release pH5.2	8 bilayers	1,84 ± 0,05	0,36 ± 0,01	0,67
	5 bilayers	1,29 ± 0,04	0,37 ± 0,01	0,48
	2 bilayers	1,47 ± 0,05	0,32 ± 0,01	0,47
Burst Release pH7.4	8 bilayers	0,23 ± 0,04	0,45 ± 0,05	0,11
	5 bilayers	0,10 ± 0,01	0,57 ± 0,03	0,06
	2 bilayers	0,16 ± 0,01	0,52 ± 0,02	0,08
Second Burst Release pH5.2	8 bilayers	0,24 ± 0,03	0,47 ± 0,03	0,11
	5 bilayers	0,25 ± 0,03	0,48 ± 0,03	0,12
	2 bilayers	0,17 ± 0,02	0,49 ± 0,03	0,08

Data on **Table 4.3** is showing M_{t_0}, n and release rate witch has been obtained as the first derivative of the equation at time t_0 ($M_{t_0} \times n$).

Note that values of M_{t_0} for the first release at pH 5.2 are one order of magnitude higher that for the first release at pH 7.4, in good agreement with the behavior observed in Figure 5.

Furthermore, for pH 5.2, there is a clear difference between M_{t_0} for 8 bilayers on one hand, and M_{t_0} for 5 and 2 bilayers on the other. This result implies that the main contribution to the drug release at pH 5.2 is coming from the outer layers.

Instead, for pH 7.4, the difference between the M_{t_0} is much smaller, what leads to the conclusion that only the drug in the outermost layer is contributing to the release. These results are in good agreement with the influence of pH on the amount of released drug observed in Figure 5.

Regarding the value of n, it can be seen that the values for each pH are similar for the different number of bilayers. This indicates, that the release dynamics is influenced by pH but not by the number of polyelectrolyte bilayers.

It is also interesting to note that, for the second release at pH 5.2, the M_{t_0} and the release rate are wisely smaller than for the first release at pH 5.2. With this data, it can be concluded that, although the DDS is sensitive to pH variation, the first release at pH 7.4 modifies the dynamics of further release events triggered by such pH variation. We attribute this fact to the availability of DOX within the polyelectrolyte layers. As part of the drug, mainly from the outermost layer, has been already released at pH 7.4, the remaining drug from deeper layers finds it more difficult to diffuse into the medium.

4.4. Summary and Conclusions

Cylindrical NAA membranes covered with polyelectrolyte layers are presented as a stimuli-responsive pH-dependent drug delivery system (DDS).

The NAA structures were achieved using two-step anodization process that resulted in a highly uniform pore size and distribution. These structures are coated with a pH-responsive polyelectrolyte and successfully loaded with DOX to estimate the influence of pH and of the quantity of polyelectrolyte bilayers on the discharge dynamics.

Greater total amounts of released DOX were found in samples immersed in acidic medium, supporting the pH responsiveness of the DDS. The amount of discharged DOX in acidic medium is in correlation with the number of polyelectrolyte bilayers, although the increase in released drug does not scale linearly with the number of polyelectrolyte bilayers. This fact suggests that only the outer bilayers in the polyelectrolyte structure contribute to the release at this pH.

Contrarily, when release is accomplished at pH 7.4, the quantity of released drug does not depend on the number of polyelectrolyte layers, what leads to the conclusion that only the drug nearest to the medium is discharged.

The quantitative evaluation of the release curves also exposed that the release dynamics (related with the exponent n in the Ritger-Peppas model) depends strongly of the pH, but the number of polyelectrolyte layers has no impact in it.

If an abrupt change in pH is applied to the DDS, from neutral to acidic medium, a second burst release is triggered. This second burst release shows a different dynamics than the first release at pH 5.2. This

can be attributed to the reduced availability of drug in the outermost layers, after the first release at pH 7.4.

As a conclusion, results show that Nanoporous Anodic Alumina coated with Layer-by-Layer pH-responsive polyelectrolyte has potential applications in local drug delivery.

4.5. References

1. Sinn Aw M, Kurian M, Losic D (2014) Non-eroding drug-releasing implants with ordered nanoporous and nanotubular structures: concepts for controlling drug release. Biomater Sci 2:10–34. doi: 10.1039/C3BM60196J
2. Losic D, Simovic S (2009) Self-ordered nanopore and nanotube platforms for drug delivery applications. Expert Opin Drug Deliv 6:1363–1381. doi: 10.1517/17425240903300857
3. Fahr A, Liu X (2007) Drug delivery strategies for poorly water-soluble drugs. Expert Opin Drug Deliv 4:403–16. doi: 10.1517/17425247.4.4.403
4. Xu H, Zhang H, Wang D, et al. (2015) A facile route for rapid synthesis of hollow mesoporous silica nanoparticles as pH-responsive delivery carrier. J Colloid Interface Sci 451:101–107. doi: 10.1016/j.jcis.2015.03.057
5. Lin Y, Lin Q, Liu X, et al. (2015) A Highly Controllable Electrochemical Anodization Process to Fabricate Porous Anodic Aluminum Oxide Membranes. Nanoscale Res Lett 10:495. doi: 10.1186/s11671-015-1202-y

6. Kang H-J, Kim DJ, Park S-J, et al. (2007) Controlled drug release using nanoporous anodic aluminum oxide on stent. Thin Solid Films 515:5184–5187. doi: 10.1016/j.tsf.2006.10.029
7. Santos A, Ferré-Borrull J, Pallarès J, Marsal LF (2011) Hierarchical nanoporous anodic alumina templates by asymmetric two-step anodization. Phys Status Solidi Appl Mater Sci 208:668–674. doi: 10.1002/pssa.201026435
8. Santos A, Alba M, Rahman MM, et al. (2012) Structural tuning of photoluminescence in nanoporous anodic alumina by hard anodization in oxalic and malonic acids. Nanoscale Res Lett 7:228. doi: 10.1186/1556-276X-7-228
9. Xifre-Perez E, Guaita-Esteruelas S, Baranowska M, et al. (2015) In Vitro Biocompatibility of Surface-Modified Porous Alumina Particles for HepG2 Tumor Cells: Toward Early Diagnosis and Targeted Treatment. ACS Appl Mater Interfaces 7:18600–18608. doi: 10.1021/acsami.5b05016
10. Xifre-Perez E, Ferre-Borull J, Pallares J, Marsal LF (2015) Mesoporous alumina as a biomaterial for biomedical applications. Mesoporous Biomater 2:13–32. doi: 10.1515/mesbi-2015-0004
11. Vallet-regí M, Balas F, Manzano M (2007) Drug Confinement and Delivery in Ceramic Implants. Drug Metab Lett 1:37–40.
12. Simovic S, Losic D, Vasilev K (2010) Controlled drug release from porous materials by plasma polymer deposition. Chem Commun (Camb) 46:1317–9. doi: 10.1039/b919840g

13. Patermarakis G, Moussoutzanis K (1995) Electrochemical kinetic study on the growth of porous anodic oxide films on aluminium. Electrochim Acta 40:699–708. doi: 10.1016/0013-4686(94)00347-4
14. Marsal LF, Vojkuvka L, Formentin P, et al. (2009) Fabrication and optical characterization of nanoporous alumina films annealed at different temperatures. Opt Mater (Amst) 31:860–864. doi: 10.1016/j.optmat.2008.09.008
15. Vojkuvka L, Marsal LF, Ferré-Borrull J, et al. (2008) Self-ordered porous alumina membranes with large lattice constant fabricated by hard anodization. Superlattices Microstruct 44:577–582. doi: 10.1016/j.spmi.2007.10.005
16. Hernández-Eguía LP, Ferré-Borrull J, Macias G, et al. (2014) Engineering optical properties of gold-coated nanoporous anodic alumina for biosensing. Nanoscale Res Lett 9:414. doi: 10.1186/1556-276X-9-414
17. Santos A, Montero-moreno JM, Bachmann J, et al. (2011) Understanding Pore Rearrangement during Mild to Hard Transition in Bilayered Porous Anodic Alumina Membranes. ACS Appl Mater Interfaces 1925–1932. doi: 10.1021/am200139k
18. Masuda H, Fukuda K (1995) Ordered Metal Nanohole Arrays Made by a Two-Step Replication of Honeycomb Structures of Anodic Alumina. Science (80-) 268:1466–1468. doi: 10.1126/science.268.5216.1466
19. Jessensky O (1998) Self-Organized Formation of Hexagonal Pore Structures in Anodic Alumina. J Electrochem Soc 145:3735. doi: 10.1149/1.1838867

20. Bruening ML, Dotzauer DM, Jain P, et al. (2008) Creation of Functional Membranes Using Polyelectrolyte Multilayers and Polymer Brushes. Langmuir ACS J surfaces colloids 7663–7673. doi: 10.1021/la800179z
21. Motlagh NSH, Parvin P, Ghasemi F, Atyabi F (2016) Fluorescence properties of several chemotherapy drugs: doxorubicin, paclitaxel and bleomycin. Biomed Opt Express 7:2400. doi: 10.1364/BOE.7.002400
22. Cho Y, Lee W, Jhon YK, et al. (2010) Polymer nanotubules obtained by layer-by-layer deposition within AAO-membrane templates with sub-100-nm pore diameters. Small 6:2683–9. doi: 10.1002/smll.201001212
23. Alba M, Formentín P, Ferré-Borrull J, et al. (2014) pH-responsive drug delivery system based on hollow silicon dioxide micropillars coated with polyelectrolyte multilayers. Nanoscale Res Lett 9:411. doi: 10.1186/1556-276X-9-411
24. Biesheuvel PM, Mauser T, Sukhorukov GB, Möhwald H (2006) Micromechanical theory for pH-dependent polyelectrolyte multilayer capsule swelling. Macromolecules 39:8480–8486. doi: 10.1021/ma061350u
25. Higuchi T (1961) Rate of release of medicaments from ointment bases containing drugs in suspension. J Pharm Sci 50:874–875. doi: 10.1248/cpb.23.3288
26. Higuchi T (1963) Mechanism of Sustained-Action Medication. Theoretical Analysis of Rate of Release of Solid Drugs Dispersed in Solid Matrices. J Pharm Sci 52:1145–1149. doi: 10.1002/jps.2600521210

27. Desai SJ, Singh P, Simonelli AP, Higuchi WI (1966) Investigation of Factors Influencing Release of Solid Drug Dispersed in Inert Matrices III. J Pharm Sci 55:1230–1234. doi: 10.1002/jps.2600551113
28. McInnes SJ, Irani Y, Williams KA, Voelcker NH (2012) Controlled drug delivery from composites of nanostructured porous silicon and poly (l -lactide) R esearch A rticle. Nanomedicine 7:995–1016.
29. Iskakov RM, Kikuchi A, Okano T (2002) Time-programmed pulsatile release of dextran from calcium-alginate gel beads coated with carboxy-n-propylacrylamide copolymers. J Control Release 80:57–68. doi: 10.1016/S0168-3659(01)00551-X
30. Feng W, Zhou X, He C, et al. (2013) Polyelectrolyte multilayer functionalized mesoporous silica nanoparticles for pH-responsive drug delivery: layer thickness-dependent release profiles and biocompatibility. J Mater Chem B 1:5886. doi: 10.1039/c3tb21193b
31. Yao F, Weiyuan JK (2011) Drug Release Kinetics and Transport Mechanisms of Nondegradable and Degradable Polymeric Delivery Systems. Expert Opin Drug Deliv 7:429–444. doi: 10.1517/17425241003602259
32. Shoaib MH, Tazeen J, Merchant H a, Yousuf RI (2006) Evaluation of Drug Release Kinetics From Ibuprofen Matrix Tablets Using Hpmc. Pak J Pharm Sci 19:119–124.

33. Lin LY, Lee NS, Zhu J, et al. (2011) Tuning core vs. shell dimensions to adjust the performance of nanoscopic containers for the loading and release of doxorubicin. J Control Release 152:37–48. doi: 10.1016/j.jconrel.2011.01.009

34. Serra L, Doménech J, Peppas NA (2006) Drug transport mechanisms and release kinetics from molecularly designed poly(acrylic acid-g-ethylene glycol) hydrogels. Biomaterials 27:5440–51. doi: 10.1016/j.biomaterials.2006.06.011

35. Gultepe E, Nagesha D, Casse BDF, et al. (2010) Sustained drug release from non-eroding nanoporous templates. Small 6:213–216. doi: 10.1002/smll.200901736

UNIVERSITAT ROVIRA I VIRGILI
DEVELOPMENT OF NANOPOROUS ANODIC ALUMINA TECHNOLOGIES FOR DRUG DELIVERY
Maria Porta Batalla

Chapter 5:

3D Structures on Nanoporous Anodic Alumina for a Retained Drug Release

UNIVERSITAT ROVIRA I VIRGILI
DEVELOPMENT OF NANOPOROUS ANODIC ALUMINA TECHNOLOGIES FOR DRUG DELIVERY
Maria Porta Batalla

In this chapter we are trying to solve a society necessity using the Nanoporous Anodic Alumina (NAA) as a drug reservoir and retained release system. To place the reader in context we have to say that manufacture of three dimensional (3D) structures can be economically costly and complex; however, electrochemistry has become a key discipline for nanotechnology due to its inexpensive fabrication of nanostructured materials. Porous alumina fabricated by anodization is a well-known example. Due to their simplicity, low-cost and attractive properties, nanoporous anodic alumina is one of the most widely used nanomaterial for numerous Nano-technological applications. In this chapter we have used NAA as a drug reservoir with different release kinetics depending on the pore shape.

5.1. Introduction

Lately in our days NAA has attracted substantial attention for several applications like: template synthesis, molecular filtration, catalysis, sensing, electronics, photonics, energy storage and drug delivery. We are going to focus our attention in this last function. We know that some studies have been already performed in the drug delivery framework using porous materials [1–10].

Nanoporous anodic alumina (NAA) is one of the most attractive material for drug delivery applications since it's simple and low-cost fabrication, the pore size and depth can easily be controlled by regulating the anodizing voltage, time and electrolyte composite as it has been explained in chapter 2 [11]. Other remarkable properties of this material are the chemical and thermal stability, hardness, high surface and highly ordered pore structure.

Although drug release from nanoporous coatings has been studied, there is a lack of understanding of the release kinetics from these platforms and the dynamics governing them [12, 13]. Herein, our aim is to explain the release kinetics from nanoporous surfaces by a model. This model will be elucidated by mean of a systematic study of release profiles.

Drug depots in human body with controlled and retained release are able to improve quality of life and assist long-term treatments; in addition the development of those new and more efficient drug delivery systems solve conventional drug therapy problems related to limited

drug solubility, lack of selectivity and unfavourable pharmacokinetics[9, 14].

The structure of NAA can be described as a close-packed hexagonal and perpendicular orientated array of columnar cells, each containing a central pore. These pores are aimed to locate organic molecules like drugs (drug depots). The drug release from porous materials is based on molecular diffusion from the pores, and it is mainly governed by the pore dimensions. Therefore, adjustment of pore diameter (Dp) and pore depth has been considered an essential strategy to control drug release kinetics[15].

5.2. Experimental Section

5.2.1. Nanoporous Alumina Anodization

Ordered nanoporous anodic alumina (NAA) was prepared by the two-step anodization method. High purity (99.999%) aluminum plates were purchased from Goodfellow (Huntingdon, UK).

Perchloric acid was used for electropolishing and phosphoric acid was used for anoditzation. Both acids were purchased from Sigma-Aldrich Corporation (St Louis, USA).

Aluminum plates were degreased in acetone and ethanol to eliminate organic impurities. They were then subsequently electropolished in a mixed solvent of perchloric acid and ethanol (1 : 3) at a constant applied voltage of 20 V for 6 minutes.

To suppress breakdown effects and to enable uniform oxide film growth at high voltage (195 V in phosphoric acid) a protective layer at lower voltage (174 V also in phosphoric acid) was performed for 180 min. After this pre-anodization, a ramp of 0,05V/s was used to reach the hard voltage (195V) during 20 hours [2, 16].

The two-step anodization procedure was used in order to achieve suitable pore ordering. For this reason, after the first anodization (first step), the disordered porous alumina grown on the aluminum surface was removed by a wet chemical etching in a mixture of phosphoric acid (0,4M) and chromic acid (0,2M) (1:1 volume ratio) at 70ºC [17]. The second anodization step was performed under the same experimental conditions (194V) as they were used in the first step in order to obtain ordered nanoporous alumina.

The layer length or pore depth was controlled by the total charge that is going through the electrodes because it has a direct relation with the amount of Nanoporous Anodic Alumina created.

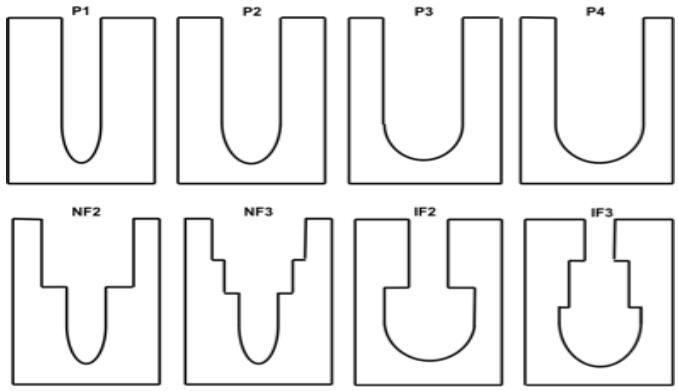

Figure 5.1. Schematic illustration of the different pore shapes. The name of every pore shape is written in the upper part.

5.2.1.1. Nanoporous Anodic Alumina Funnels

Normal Funnels (NF) samples are performed alternating anodization process and pore widening process [18]. Depending on the number of layers the samples were named NF2 (Normal Funnels of 2 layers) or NF3 (Normal Funnels of 3 layers) (**Figure 5.1**).

NF2 were performed with a second anodization (after the first step that is removed using the wet chemical etching) for 15μm of layer length. After that, a pore widening for 90 minutes was performed, and finally another anodization for 15μm was done. This way NF2 samples has a first layer with a larger diameter due to the pore widening procedure [19], and a second layer with the natural electrochemical pore diameter.

NF3 samples were achieved with a second anodization (after the first step anodization already dissolved) for 10μm layer length, then a

pore widening for 45 minutes, another anodization for 10µm (the third one), another pore widening for 45 minutes, and a final anodization (the fourth) for 10µm (**Figures 5.2, 5.3A**). NF3 samples has a first layer of 10 µm length with 90 minutes of pore widening process (45+45 min), a second layer of 10 µm with 45 minutes of pore widening, and a third layer of 10 µm with no pore widening procedure.

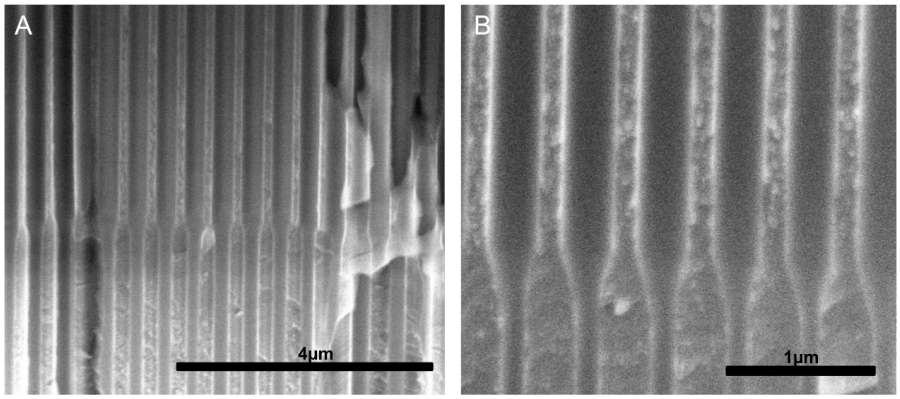

Figure 5.2. Cross section ESEM images of Normal Funnels A) NF2 at 30000 magnifications B) NF2 at 50000 magnifications

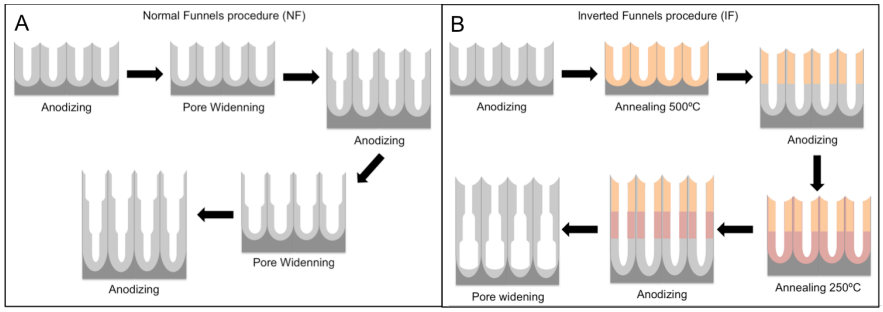

Figure 5.3. Schematics of the funnels procedures. A) Schematics of the normal funnels procedure. B) Schematics of the inverted funnels procedure.

In order to achieve the Inverted Funnels (IF) structures, a thermal treatment to change the amorphous crystallographic phase of the alumina to gamma crystallographic phase was used. The temperatures treatments were 250ºC and 500ºC (**Figure 5.3B**). Actually, other temperatures can be used. We chose those temperatures arbitrary.

As normal funnels, inverted funnels were named IF2 (Inverted Funnels 2 layers) or IF3 (Inverted Funnels 3 layers) depending on the number of layers (**Figure 5.1**).

IF2 were performed starting with a pore anodization using the two step process. Once we had 15 μm of layer length anodized a temperature treatment at 500ºC was realized. After that, another anodization about 15μm whas performed. And finally a pore widening for 2 hours was realised (**Figure 5.4**).

This whole methodology produced samples with two different layers. The upper layer had narrower pores thanks to the temperature treatment that reduces the pore widening rate. The layer in the lower part (next to the aluminium) had widener pores because there was no temperature treatment in this region.

IF3 were performed with a second anodization (after the first step a removed) for 10μm. After that, a 500ºC temperature treatment was realized. Another anodization (the third one) for 10μm was completed. Then another temperature treatment, this time at 250ºC was done. And finally a last anodization (the fourth) for 10μm was made.

After all that procedure, we did pore widening etching for 2 hours (**Figure 5.5**).

This way, IF3 had 3 different layers of 10 μm each: an upper one that was treated with 500ºC, and for that reason had the narrower pores, a middle one, that received a 250ºC treatment causing a middle pore diameter. And the layer in the bottom that did not received any temperature treatment reason why had the wider pores.

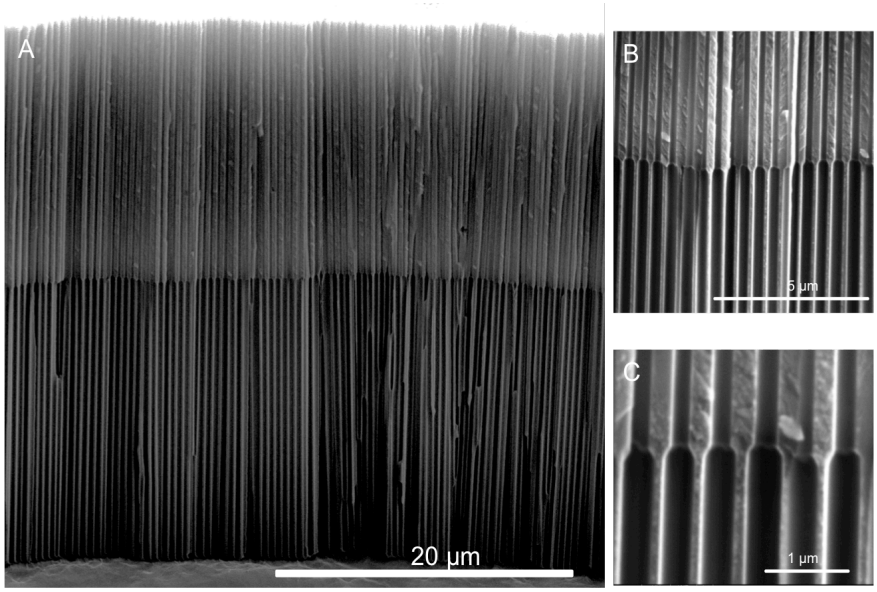

Figure 5.4. Cross section ESEM image of the two layered inverted funnels sample at different magnifications for IF2 samples. A) capture of the entire bilayer at 4000 magnifications. B) Capture of the IF2 samples at 15000 magnifications. C) Detail of the pore transition at 40000 magnifications.

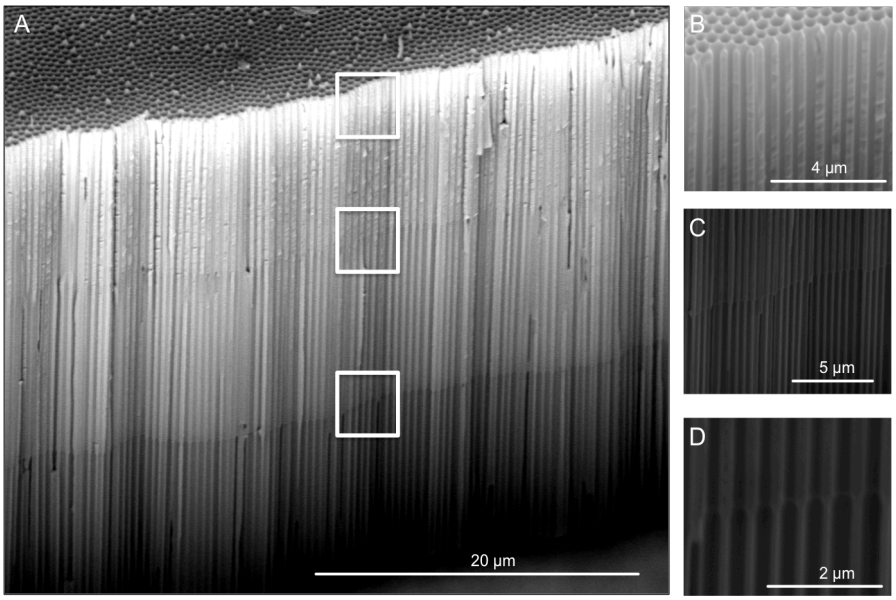

Figure 5.5. Cross section ESEM image of the three layered inverted funnels samples (IF3). B-D) Correspond to magnifications of the framed areas in image A from the top to the bottom.

Samples were characterized by Environmental Scanning Electron Microscopy (ESEM). Furthermore a calibration study for the wet etching pore opening process was performed both with 500ºC of temperature treatment and without temperature treatment. For this reason ESEM images of samples etched at different times were performed. The interval chosen between the images was 15 minutes (**Figure 5.6**). Pores were measured using Image-J software (freely available at http://www.nih.gov).

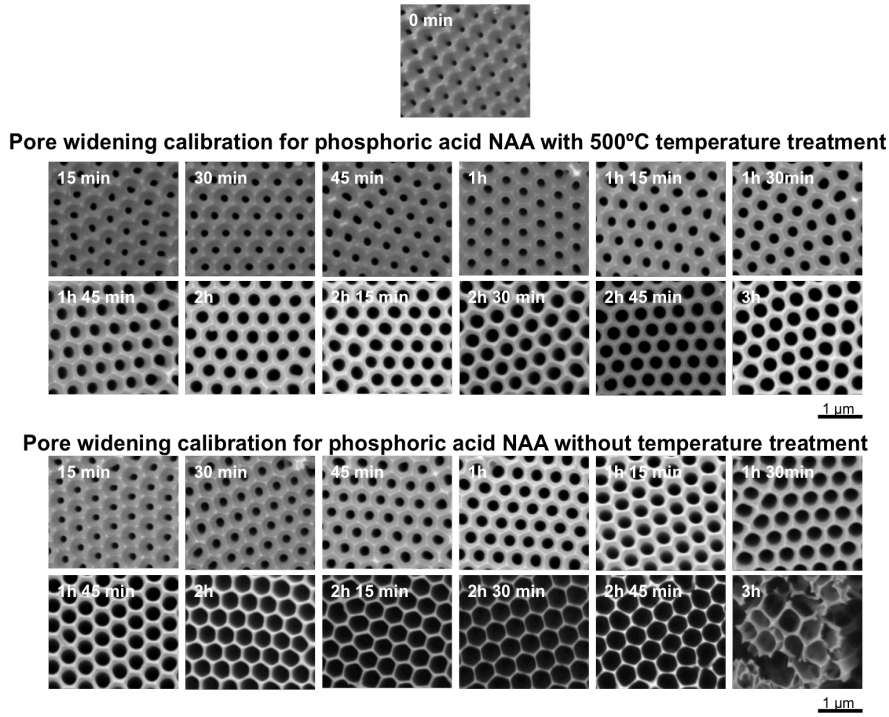

Figure 5.6. Time lapse for pore widening samples at different times with temperature treatment and without treatment.

5.2.2. Drug Loading and Release Studies

Doxorubicin (DOX) which is a self-fluorescent drug was selected as a model drug. DOX solution at 1mg/ml concentration was loaded into the templates for the release studies. The suspension was stirred over night in the dark with the samples immersed. The release studies were performed in vitro using phosphate-buffered saline (PBS), which is commonly employed to simulate in vivo conditions for drug release. Dox was measured directly in the release medium. This design is critical to understand the release kinetics, since it allows the collection of fast and

frequent data over time. One of the advantages of the in situ measurement setup used in these experiments is that it is possible to collect release data frequently, which helps in understanding the short-term burst effect.

Drug release was measured by drug photoluminescence. The photoluminescence measurements were taken on a fluorescence spectrophotometer from Photon Technology International Inc. (Birmingham, NJ, USA) with a Xe lamp used as the excitation light source at room temperature and an excitation wavelength (λex) of 480 nm and emission wavelength of 590 nm.

5.3. Results and Discussion

Regular or Normal Funnels (NF) were successfully achieved. **Figure 5.2** shows ESEM cross-section pictures of the sample NF2, at two different magnifications. **Figure 5.2A** shows the transition from an etched region (top) to a non-etched region (bottom), while **figure 5.2B** shows a close-up photo. The pictures demonstrate a straight growth of the pores, without discontinuities (occluded pores) despite the interruption in the anodization process between the two regions. The transition between the two regions is smooth and shows a conical shape.

Inverted Funnels (**IF**) were also successfully achieved. **Figure 5.4A** shows a general image of **IF2** samples. In this image we can observe a linear disposition of the pores, as well as a clear transition from thin pores to thick pores. **Figures 5.4B and 5.4C** shows magnifications of sample IF2 where the conic structure of the transition from thin to thick can be observed. At the same time looking at those images we can

assume that the crystallization of the aluminum oxide by the temperature treatment at 500ºC was correctly performed.

Figure 5.5A shows a general image of IF3 samples. In this image we can observe a linear disposition of the pores, as well as a clear transition from thin pores to thick pores. The different layers length could also be measured by this image. **Figures 5.5B,C and D** shows the magnified zones squared in the general photo. As mentioned above the same conic structure could be observed in IF3 samples. With this result, we demonstrate that the annealing at the intermediate temperature of 250º results in an intermediate etching rate.

Samples treated by pore opening etching during different times spaced 15 minutes between them where investigated using ESEM. Two different groups (without temperature treatment and 500ºC) were performed in order to calibrate the different pore opening rates on both groups.

On **figure 5.6** it can be observed that the samples with temperature treatment have a lower pore opening rate than those without the treatment. Moreover, it is noticeable that for samples without temperature treatment the alumina matrix becomes completely destroyed due to the dissolution of the pore walls at 3 hours of pore widening process.

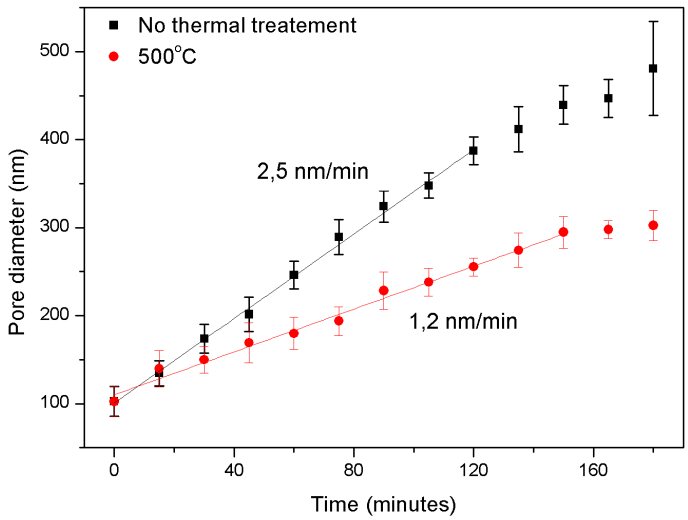

Figure 5.7. Calibration curve for the pore widening treatment where the pore diameter is related with the etching time for samples without temperature treatment (black squares) and samples with 500ºC of temperature treatment (red circles). The dissolution rate in nm/min has been calculated by lineal fitting of the graphs.

Variations of pore diameter (D_p) measurements can be seen in **figure 5.7** where differences between the non-treated samples and the temperature treated ones are revealed. This phenomenon is driven by the change in the crystallographic phase of the alumina and consequently the stability. More concretely, the annealing is what induces the change in the crystallographic phase in the alumina.

Pore diameters for non-treated samples etched for 3 hours have reached the Interpore Distance (D_{int}). That means that the whole NAA is dissolved for the wet chemical pore opening procedure in this time.

Nevertheless we could observe that the oxide matrix structure started to become damaged in some little areas after 2 hours and 30 minutes of pore widening process. For this reason 2 hours was chosen as the maximum etching time, for being sure that the matrix is not damaged.

Looking to the evolution of pore diameter as a function of time upon wet-chemical etching of porous NAA (**figure 5.7**), it was found that the wet etching pore opening rate is decreasing in time on both treated and non-treated samples. In accordance with the literature [18, 19] an inflection point can be found. This inflection corresponds to an interface separating two different compositions of the oxide matrix: an outer (closer to the pore) layer with a given concentration of anions from the electrolyte, and a relatively more pure inner layer (see chemical composition section in chapter 2) . The anion contaminated layer is easily removed by the etching treatment meanwhile the more pure alumina is more resistant to the pore widening procedure. Those inflection points have been found in 120 minutes for the non-treated samples and 150 minutes for those samples with temperature treatment.

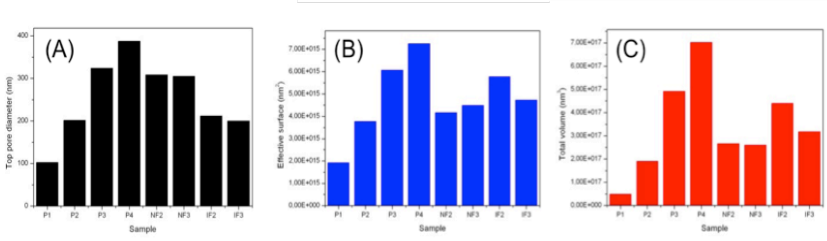

Figure 5.8. A) Graph showing the top pore diameter for every sample shape. B) Graph displaying the effective surface for every sample shape. C) Graph presenting the total volume of the sample for every different sample shape.

Table 5.1. Shows the measurements for different pore typologies

Sample	Pore Widening Time (minutes)	Top pore diameter (nm)	Middle pore diameter (nm)	Bottom pore diameter (nm)	Top height (μm)	Middle height (μm)	Bottom height (μm)
P1	0	102	-	-	30	-	-
P2	45	201	-	-	30	-	-
P3	90	324	-	-	30	-	-
P4	120	387	-	-	30	-	-
NF2	90	308	-	137	15	-	15
NF3	45+45	304	198	105	11	12	12
IF2	120	211	-	358	15	-	16
IF3	120	200	260	317	9	9	9

Table 5.2. Show calculations for sample surface and total pore volume for every pore structure typology.

Sample	Effective surface (nm^2)	Total volume (nm^3)
P1	1,914E+15	4,9071E+16
P2	3,766E+15	1,8991E+17
P3	6,063E+15	4,9184E+17
P4	7,247E+15	7,0229E+17
NF2	4,163E+15	2,6614E+17
NF3	4,4859E+15	2,6025E+17
IF2	5,769E+15	4,4012E+17
IF3	4,7296E+15	3,1742E+17

Table 5.1 shows the average measurements of top pore diameters, middle pore diameters, bottom pore diameters, layer length, the effective surface and the total volume, for every type of sample. Notice that the top pore diameter is directly related to pore widening time. This way, as samples SP1, SP2, SP3 and SP4 were exposed to pore widening treatment in increasing intervals of time, the pore diameters (directly related to the etching time) are also showing growing lengths as it can be clearly observed in **Figure 5.8A**.

It can be also observed that Normal Funnels structures (NF2 and NF3) show similar top pore diameter than P3 samples (around 300 nm), and the same occurs between Inverted Funnels (IF2 and IF3) and P2 (their top pore diameter measures around 200 nm).

The total layer length of the samples (in sum in the case of the layered samples) is 30 μm to be able to compare the results between them. The effective surface area is clearly related with the pore diameter (Dp) in the case of straight pores, but is not so in the case of layered samples (**Figure 5.8B and 5.9A**).

The total volumes for every sample type are presented in **Table 5.2** and also represented in **Figure 5.8C and 5.9B.** When those samples are presented in terms of total amout of drug versus the surface area or volume, samples are ordered in a linear way as it can be seen in **Figure 5.9**.

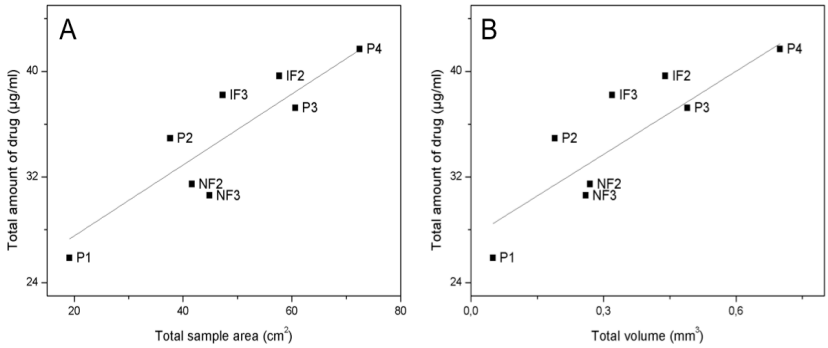

Figure 5.9. A) Graph relating the total amount of drug and the total sample area. B) Graph relating the total amount of drug and the total volume calculated for every sample shape.

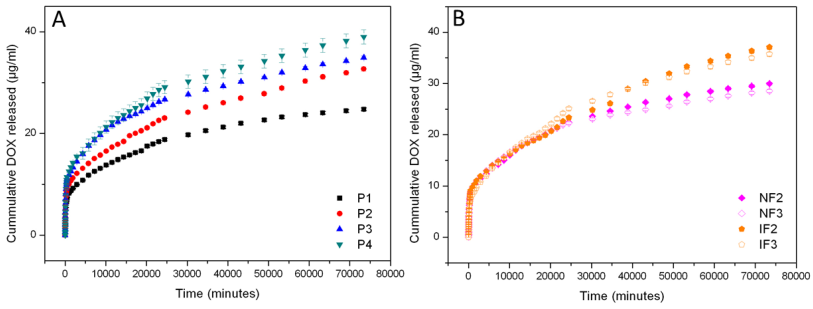

Figure 5.10. Graphs showing the cumulative drug release of different sample shapes in minutes. A) Release from regular pores. B) Release from Normal Funnels (NF2, NF3) in pink and release from Inverted Funnels (IF2, IF3) in orange.

In **figure 5.10** a general release profile is shown for straight pores (**Figure 5.10A**) and for the funnels (**Figure 5.10B**). We can observe a burst release within the first minutes, and then the release rate is decreasing slowly. **Figure 5.10A** shows the complete release for straight pore samples, where it can be clearly observe a direct relation between the pore diameter (Dp), the DOX total amount and the release tax. In **figure 5.10B** we can observe Normal Funnels (NF) and Inverted Funnels (IF) complete release. On this case it can be clearly appreciate that the release rate of the Inverted Funnels is maintained for longer time than Normal Funnels samples.

In order to identify the release constant we used Origin software to find the equation witch best describes the drug liberation. A variation of the Higuchi equation follows:

$$M_t = M_0 + K\sqrt{t} \qquad \textbf{(5.1)}$$

Were M_t is the cumulative release at time t, M_0 is the intercept value when time is zero and k is the release constant [20, 13, 15, 21–23].

To identify the release rate mechanism and model the drug transport in the NAA nanotube systems for the first 480 minutes (8 hours), we made the hypothesis that the release data obtained could be fitted using **equation 5.1** and the results are given in **Figure 5.11** where the cumulative DOX release was plotted versus the square root of time during the burst release [24-26]. A near perfect linear fit was observed for every different pore shape, demonstrating that the drug kinetics approximately follow the square root of time relationship.

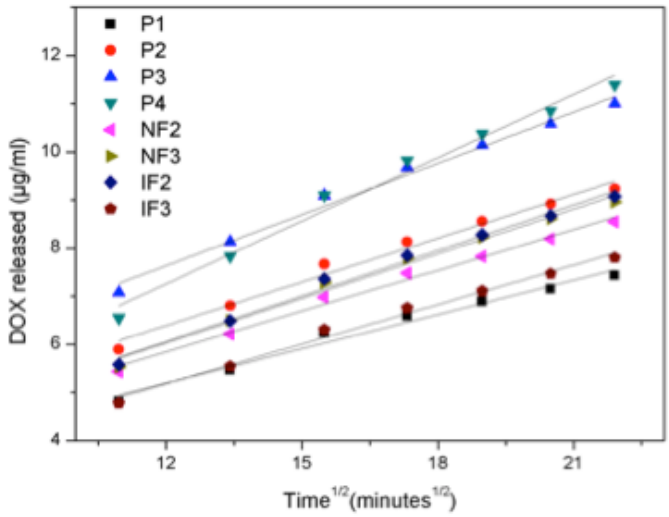

Figure 5.11. Fitting of the release data within the first minutes (Burst release) using Higuchi equation (equation 5.1).

Table 5.3 shows the different fitting parameters for every different pore shape. It can be also observed that the release rate or slope in the linear fittings (K) is directly correlated with the pore diameter **Figure 5.12**. This way a linear relation has been found to relate the pore diameter and the release rate for the first minutes (burst release) following the next equation:

$$K = 0{,}168 + 6{,}46 * 10^{-4} * D_p \qquad \textbf{(5.2)}$$

Were K is the release constant in (µg/ml)/minute and D_p is the pore diameter in nanometers.

Table 5.3. Data from the Higuchi equation fitting within the first minutes

Sample name	Intercept (M_0)	Slope (k)
P1	2,34 ± 0,26	0,24 ± 0,02
P2	2,75 ± 0,29	0,30 ± 0,02
P3	3,38 ± 0,29	0,35 ± 0,02
P4	2,01 ± 0,43	0,44 ± 0,02
NF2	2,45 ± 0,21	0,28 ± 0,01
NF3	2,31 ± 0,25	0,31 ± 0,01
IF2	2,28 ± 0,25	0,32 ± 0,01
IF3	1,89 ± 0,20	0,27 ± 0,01

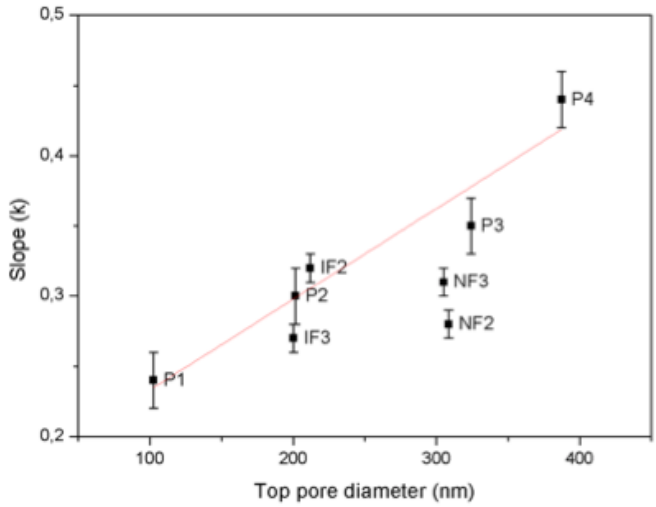

Figure 5.12. Fitting graph showing the relation between the slope or release constant and the top pore diameter, also expressed in **equation 5.2.**

To continue with the identification of the release mechanism model we used the Korsmeyer-Peppas (**equation 5.3**) for the long time release (from day 2 to day 63). **Figure 5.13** shows the data from the complete release fitted from 24 hours

$$M_t = M_{t0}\left(\frac{t}{t_0}\right)^n \quad \textbf{(5.3)}$$

Where M_t is the proportion of drug released at given time t, M_{t0} is the amount of drug released at the reference time t_0 (1day), t is time in days and n is the release parameter related to the release rate.

Data in **Table 5.4** is showing M_{t0}, n and the release rate that has been obtained as the first derivative of the equation (**equation 5.3**) at time t_0 (1day).

It can also be observed a relation of the release rates and the pore diameter on the regular pores (**Figure 5.14**). The release rate values from the Inverted Funnels (IF) is over the linear fitting from the Regular Funnels meanwhile the Normal Funnels values are under the linear fittings.

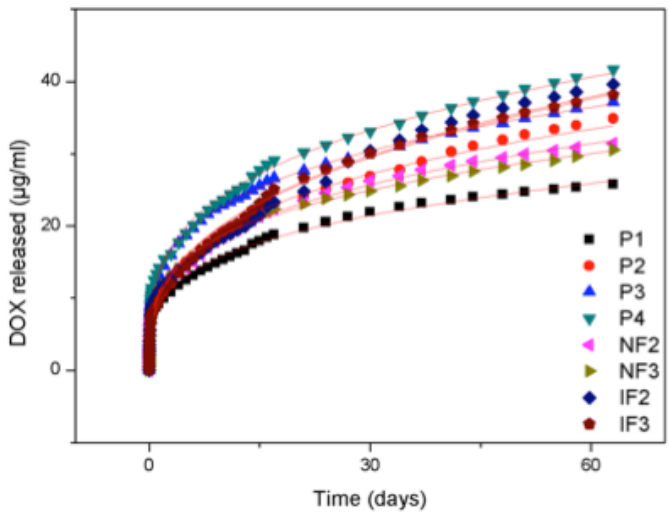

Figure 5.13. Graph showing the fitting using the Korsmeyer-Peppas **equation 5.3** and the data from the late release.

Table 5.4. Data extracted from the Korsmeyer-Peppas fitting ($M_t=M_{to}*(t/t_o)^n$)

Sample name	M_{to}	n	Release Rate	Adj. R-Square
P1	8,43 ± 0,14	0,27 ± 0,01	2,31	0,99
P2	9,93 ± 0,21	0,30 ± 0,001	2,94	0,99
P3	12,49 ± 0,17	0,26 ± 0,00	3,27	0,99
P4	12,55 ± 0,22	0,28 ± 0,01	3,60	0,99
NF2	9,70 ± 0,16	0,29 ± 0,00	2,78	0,99
NF3	10,14 ± 0,15	0,27 ± 0,00	2,69	0,99
IF2	9,00 ± 0,33	0,35 ± 0,01	3,16	0,98
IF3	8,91 ± 0,18	0,35 ± 0,01	3,13	0,99

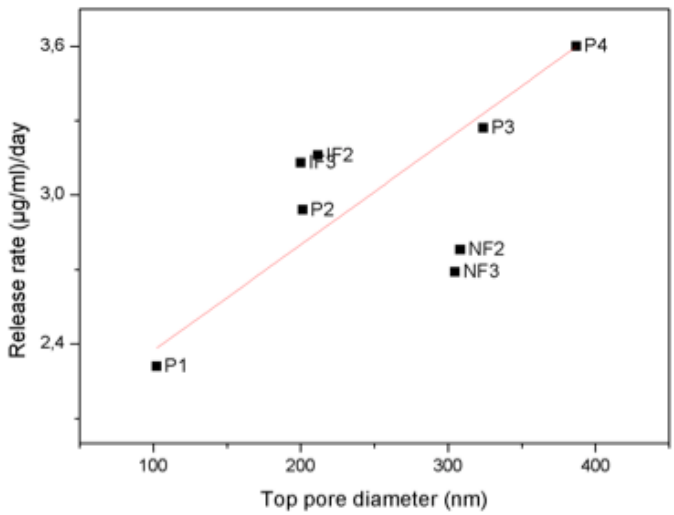

Figure 5.14. Graph showing the relation between the Release rate obtained in the late release using the Korsmeyer-Peppas **equation 5.3** and the top pore diameter.

We also calculated the release rate of this samples through the first derivative of the **equation 5.3**, they are shown in **Table 5.4**. Those release rates were also related with the top pore diameter for the regular pore shape (**Figure 5.14**) but in this case Inverted Funnels samples release rates are above the linear fitting meanwhile the Normal Funnels values are under the Regular tendency. We also calculated the equation for the regular pore shape tendencies relating the release rate and the top pore diameter for long release data (**Equation 5.4)**

$$Release\ rate = 1{,}95 + 0{,}004D_p \qquad \textbf{(5.4)}$$

Were D_p is the top pore diameter.

5.4. Summary and Conclusions

The effect of the alumina solubility due to different temperature crystallization was investigated using ESEM. NAA samples treated with temperature presented lower solubility rate. On the basis of this referred difference of the pore opening rate due to different crystallization, different porous shapes were performed in order to study the best structure for drug release.

The quantitative dynamics of the release has been studied in two different regimes: A short-term release and a long-term release. During the short-term release (8 hours) regular pores samples keep a direct linear relation between the pore diameter and the release constant (K). This relation has been described by the Higuchi model (**equation 5.1**). At the same time both Normal and Inverted Funnels samples show a lower release constant (K) during the bust release than the regular pores (**Figure 5.12**).

For the long-term release, the data has been fitted by the Korsmeyer-Peppas model (**equation 5.3**). In this case we used the release rate in order to compare the different behaviours. We also found a linear relation with the top pore diameter in the case of regular pores, but release rates in Inverted funnels where higher than the tendency, and the Normal Funnels values were lower than the tendency. Those results reveal that the Inverted Funnels structures retain inside the pores a higher quantity of drug than the Normal Funnels or the regular pores with the same volume, area or top pore diameter. This retention allows this pore structure to release the active molecule in a sustained way.

The results obtained demonstrate that this 3D pore structures satisfy all the requirements that ensures an efficient drug therapy.

5.5. References

1. Losic D, Simovic S (2009) Self-ordered nanopore and nanotube platforms for drug delivery applications. Expert Opin Drug Deliv 6:1363–1381. doi: 10.1517/17425240903300857
2. Porta-i-Batalla M, Eckstein C, Xifré-Pérez E, et al. (2016) Sustained, Controlled and Stimuli-Responsive Drug Release Systems Based on Nanoporous Anodic Alumina with Layer-by-Layer Polyelectrolyte. Nanoscale Res Lett 11:372. doi: 10.1186/s11671-016-1585-4
3. Jeon G, Yang SY, Kim JK (2012) Functional nanoporous membranes for drug delivery. J Mater Chem 22:14814. doi: 10.1039/c2jm32430j
4. Gultepe E, Nagesha D, Sridhar S, Amiji M (2010) Nanoporous inorganic membranes or coatings for sustained drug delivery in implantable devices. Adv Drug Deliv Rev 62:305–15. doi: 10.1016/j.addr.2009.11.003
5. Kang H-J, Kim DJ, Park S-J, et al. (2007) Controlled drug release using nanoporous anodic aluminum oxide on stent. Thin Solid Films 515:5184–5187. doi: 10.1016/j.tsf.2006.10.029
6. Santos A, Ferré-Borrull J, Pallarès J, Marsal LF (2011) Hierarchical nanoporous anodic alumina templates by asymmetric two-step anodization. Phys Status Solidi Appl Mater Sci 208:668–674. doi: 10.1002/pssa.201026435
7. Santos A, Alba M, Rahman MM, et al. (2012) Structural tuning of photoluminescence in nanoporous anodic alumina by hard anodization in oxalic and malonic acids. Nanoscale Res Lett 7:228. doi: 10.1186/1556-276X-7-228

8. Großberger S, Fey T, Lee G (2016) Vacuum-Induced Surface Freezing to Produce Monoliths of Aligned Porous Alumina. 1–14. doi: 10.3390/ma9120983
9. Xifre-Perez E, Guaita-Esteruelas S, Baranowska M, et al. (2015) In Vitro Biocompatibility of Surface-Modified Porous Alumina Particles for HepG2 Tumor Cells: Toward Early Diagnosis and Targeted Treatment. ACS Appl Mater Interfaces 7:18600–18608. doi: 10.1021/acsami.5b05016
10. Allen TM, Cullis PR (2004) Drug delivery systems: entering the mainstream. Science 303:1818–22. doi: 10.1126/science.1095833
11. Lin Y, Lin Q, Liu X, et al. (2015) A Highly Controllable Electrochemical Anodization Process to Fabricate Porous Anodic Aluminum Oxide Membranes. Nanoscale Res Lett 10:495. doi: 10.1186/s11671-015-1202-y
12. Fu Y, Kao WJ (2010) Drug release kinetics and transport mechanisms of non-degradable and degradable polymeric delivery systems. Expert Opin Drug Deliv 7:429–44. doi: 10.1517/17425241003602259
13. Sinn Aw M, Kurian M, Losic D (2014) Non-eroding drug-releasing implants with ordered nanoporous and nanotubular structures: concepts for controlling drug release. Biomater Sci 2:10–34. doi: 10.1039/C3BM60196J
14. Ribes À, Xifré -Pérez E, Aznar E, et al. (2016) Molecular gated nanoporous anodic alumina for the detection of cocaine. Sci Rep 6:38649. doi: 10.1038/srep38649
15. McInnes SJ, Irani Y, Williams KA, Voelcker NH (2012) Controlled drug delivery from composites of nanostructured porous silicon and poly (l -lactide) R esearch A rticle. Nanomedicine 7:995–1016.

16. Wang D, Zhang L, Lee W, et al. (2013) Novel three-dimensional nanoporous alumina as a template for hierarchical TiO2 nanotube arrays. Small 9:1025–1029. doi: 10.1002/smll.201201784
17. Santos A, Vojkuvka L, Alba M, et al. (2012) Understanding and morphology control of pore modulations in nanoporous anodic alumina by discontinuous anodization. Phys Status Solidi a-Applications Mater Sci 209:2045–2048. doi: 10.1002/pssa.201228150
18. Losic D, Santos A (2015) Nanoporous Alumina : Fabrication, Structure, Properties and Applications. doi: 10.1007/978-3-319-20334-8
19. Han H, Park SJ, Jang JS, et al. (2013) In situ determination of the pore opening point during wet-chemical etching of the barrier layer of porous anodic aluminum oxide: Nonuniform Impurity Distribution in Anodic Oxide. ACS Appl Mater Interfaces 5:3441–3448. doi: 10.1021/am400520d
20. Gultepe E, Nagesha D, Casse BDF, et al. (2010) Sustained drug release from non-eroding nanoporous templates. Small 6:213–216. doi: 10.1002/smll.200901736
21. Yao F, Weiyuan JK (2011) Drug Release Kinetics and Transport Mechanisms of Nondegradable and Degradable Polymeric Delivery Systems. Expert Opin Drug Deliv 7:429–444. doi: 10.1517/17425241003602259
22. Costa P, Sousa Lobo JM (2001) Modeling and comparison of dissolution profiles. Eur J Pharm Sci 13:123–133. doi: 10.1016/S0928-0987(01)00095-1
23. Singhvi G, Singh M (2011) In-vitro drug release characterization models. Int J Pharm Stud Res II:77–84.

24. Noh K, Brammer KS, Choi C, et al. (2011) A New Nano-Platform for Drug Release via Nanotubular Aluminum Oxide. J Biomater Nanobiotechnol 2:226–233. doi: 10.4236/jbnb.2011.23028
25. Suvakanta D, Murthy PN, Nath L, Prasanta C (2010) Kinetic Modeling on Drug Release from Controlled Drug Delivery Systems. Polish Pharm Soc 67:217–223.
26. Porta-i-Batalla M, Xifré-Pérez E, Eckstein C, et al. (2017) 3D nanoporous anodic alumina structures for sustained drug release. Nanomaterials 7:227. doi: 10.3390/nano7080227

Chapter 6:

Silicon Particles for Drug Delivery

UNIVERSITAT ROVIRA I VIRGILI
DEVELOPMENT OF NANOPOROUS ANODIC ALUMINA TECHNOLOGIES FOR DRUG DELIVERY
Maria Porta Batalla

Porous silicon is an strong competitor for Nanoporous anodic alumina and a good alternative for aplications in which the degradation of the biomaterial presents an advantage. Porous silicon has emerged as a very powerful material in terms of medical applications due to its demonstrated biocompatibility. Its unique features like controllable pore size and malleable surface chemistry make porous silicon a really promising material.

This chapter presents a fundamental overview of porous silicon focusing to mesoporous silicon for drug delivery applications and also a sol-gel mesoporous nanoparticles achievement.

6.1. Fundamentals for Silicon Nanotechnology

The marriage between Uhlir and Turner were working in Bell laboratories when they accidentally discovered porous Silicon in the mid 1950s [1]. They found out that the silicon wafer didn't dissolve uniformly under certain conditions, but it presented really small holes instead. As this was not a desired result they report the result and forgot about it.

Twenty years later the discovery took importance due to it's applicability to spectroscopic studies. The surface area is increased which was thought to be useful as a model of the crystalline silicon used for infrared spectroscopy, as a precursor to produce thick silicon layers and as an electrical insulator in capacitance-based chemical sensors [2–5].

In 1990s Ulrich Goesele at Duke University found quantum confinement effects in the absorption spectrum of porous silicon, and Leigh Canham at the Defense Research Agency in England reported efficient bright red-orange photoluminescence from the material [6, 7]. At the same time phase, the singularity of the features of the material: large surface area, controllable pore size and compatibility with conventional silicon microfabrication technologies inspired research into applications far outside optoelectronics such as: sensing or biomedicine [8–11].

Overwhelming majority of published research articles about porous silicon is based on the porosification of silicon by electrochemical etching. This porous silicon is generated by etching crystalline silicon in

aqueous or non-aqueous electrolytes containing hydrofluoric acid. The final pore morphology, thickness, density and specific area vary in a wide range depending on the anodization conditions (electrolyte composition, current density and time of current applied) and the properties of the silicon (doping, resistivity and orientation). Hence, varying these parameters the structural features can be modified [12]. But porous sol-gel silicon can be also achieved using chemical precursors.

6.2. Electrochemical Etching

In the electrochemical reaction of silicon, two electrodes are needed like in the aluminium one. The first supplies electrons to the silicon (the cathode) and the other removes electrons from the solution (the anode). In the case of porous silicon formation, the silicon wafer acts as the anode, and the chemical being oxidized is the silicon itself. This is the reaction we are interested on, electrochemists refer to the silicon electrode as the "working electrode". The cathode is constructed by a hydrofluoric acid resistant platinum wire, and it is called the "counter-electrode". The reaction that is happening in the cathode is essentially the reduction of photons to hydrogen gas. Once the current is flowing between the cathode and the anode the pores are growing in the top part of the wafer. See Figure 6.1. The cathode and the anode are separated by few millimetres to several centimetres inside the electrolyte solution.

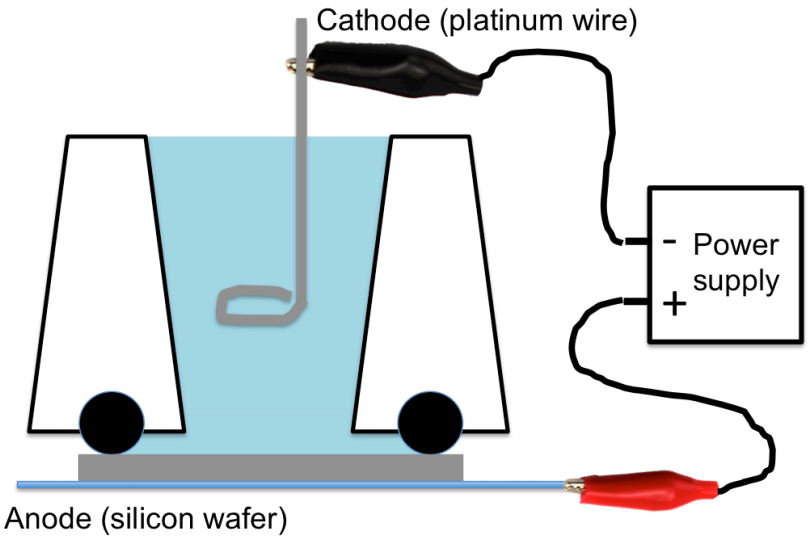

Figure 6.1. Schemeatics of the cell anodization used for the fabrication of porous silicon layers.

Silicon is thermodynamically unstable in air or water, therefore it reacts spontaneously to form an oxide layer. The oxide can be nonstoichiometric and hydrated to various degrees, though the simple empirical formula is silicon dioxide (SiO_2). Thus, preparation of porous silicon require an additive in the solution to dissolve the oxide and allow electrochemical oxidation to continue. The Si-F bond is the only bond stronger than Si-O, so in presence of aqueous HF, SiO_2 spontaneously dissolves (**equation 6.1**).

$$SiO_2 + 6HF \rightarrow SiF_6^{2-} + 2H^+ + 2H_2O \qquad (6.1)$$

6.2.1. Electrochemical Reactions in the Silicon Etching System

Figure 6.2 is showing the current-potential curve for silicon in HF electrolyte. There is an initial increase in the current where the porous silicon formation is performed, a transition region and finally the electropolishing regime.

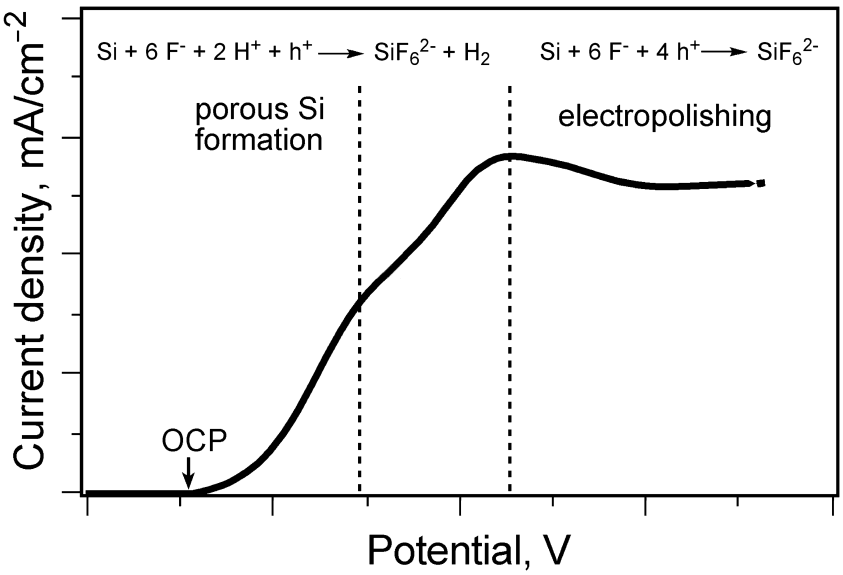

Figure 6.2. Graph showing current density versus potential generalities for electrochemical etching of silicon. Different regimes can be differentiated for porous silicon formation and electropolishing procedure. This figure have been adapted from reference [12].

To bring the corrosion to the silicon, positive current have to go through the silicon electrode. The simplest reaction happening in the anodic dissolution of silicon in fluoridic solutions is the 4-electron oxidation, presented in **equation 6.2.** Here we use holes in the silicon valence band as the oxidizing equivalents. This equation is written as a half-reaction. The electrons given by the Si at the anode must be balanced by a reduction (half-reaction) that consumes electrons at the cathode, usually water to hydrogen gas. This reaction produce silicon hexafluoride ions that are really stable dianions and are highly soluble in water.

Anode (working electrode)

$$Si + 6F^- + 4h^+ \rightarrow SiF_6^{2-} \qquad (6.2)$$

This reaction is predominant when the dissolution of silicon is occurring under electropolishing conditions and no porous silicon is being formed. It takes place at more positive electron potentials, in the right part in **figure 6.2**.

First time Uhlirs prepared porous silicon [1], they saw bubbles rising from the silicon wafer (**Figure 6.3**). The bubbles coming from the platinum wire (cathode) are hydrogen coming from the water electrolysis reaction.

Figure 6.3. Image of an electrochemical etching of silicon in the current regime where porous silicon is formed. Hidrogen gas bubbles can be observed in the solution. This image was taken in Sailor's lab in University of California San Diego.

The reaction occurring at low applied potentials is the 2-electron process. The 2-electron oxidation equations are presented in two steps: **equation 6.3** and **equation 6.4**. The pore formation is directed by the half-reaction presented in **equation 6.5**. Holes in the silicon valence band are used as the oxidizing equivalents.

$$\text{Electrochemical step: } Si + 2F^- + 2h^+ \rightarrow [SiF_2] \quad (6.3)$$

$$\text{Chemical step: } [SiF_2] + 4F^- + 2H^+ \rightarrow SiF_6^{2-} + H_2 \quad (6.4)$$

$$\text{Net: } Si + 6F^- + 2H^+ + 2h^+ \rightarrow SiF_6^{2-} + H_2 \quad (6.5)$$

Actually, the resulting pore morphology does depend on the type of silicon electrode, its doping level, and process conditions.

6.2.2 Mechanisms of Pore Formation

Although many details of the porous silicon construction still stay unclear, some statements can be made. In the pore formation, Si dissolution competes with oxidation and subsequent dissolution of the oxide. That means that the electrolyte has to be able to dissolve silicon dioxide (SiO_2). Another requirement for the pore formation are the electric holes since the reaction is started by hole capture at the surface[13]. In addition the current must be kept between zero and the electropolishing current.

As well as the alumina porosification, the initiation of the pore grow in silicon dioxide could begin at micro-cavities, structural defects, mechanically strained areas, or local perturbations [14, 15]. Then the dissolution is happening preferentially at the pore bottoms, where the curvature of the surface is largest, the intensity of the electric field is higher and enough holes are available. Therefore, the etching of porous silicon proceeds in depth to all directions that follow the anodic current paths inside silicon. The pore walls become passivated, so the dissolution only occurs at the porous silicon/crystalline silicon interface.

In addition, when pores encounter each other the current flow is redirected, this way further etching is obstructed. So, the porosity remains constant and what that is constantly growing is the layer thickness of the porous silicon. A wide range of pore geometries and morphologies are available by modifying the electrochemical parameters and the characteristics of the silicon wafers. Like in the alumina, according to IUPAC nomenclature for porous materials, pores under 2

nanometers are called microporous. The pores between 2 and 50 nanometers are called mesoporous. And we use macroporous for pores larger than 50 nanometers [16].

In **table 6.1** different pore category, type of silicon, size of the pores, morphology of the pores and the pore formation mechanisms are shown.

Table 6.1. Relation between pore category, silicon type, size of pores range, morphology and the pore formation mechanism.

Pore category	Silicon type	Pore Size range	Morphology	Mechanism
Microporous	p	2 nm	Sponge	Crystallographic face selectivity/ Enhanced electric field/ quantum confinement
Mesoporous	p^+, p^{++}, n^+	2-50nm	Branchy	Enhanced electric field
Macroporous	n^+, p^+, n, p	50nm-100µm	Tubular	Space-charge limited/ Minority carrier collection/ Thermionic effect

When a silicon wafer is immersed in a HF solution, the oxide dissolves and the surface becomes terminated with hydrogen [17].

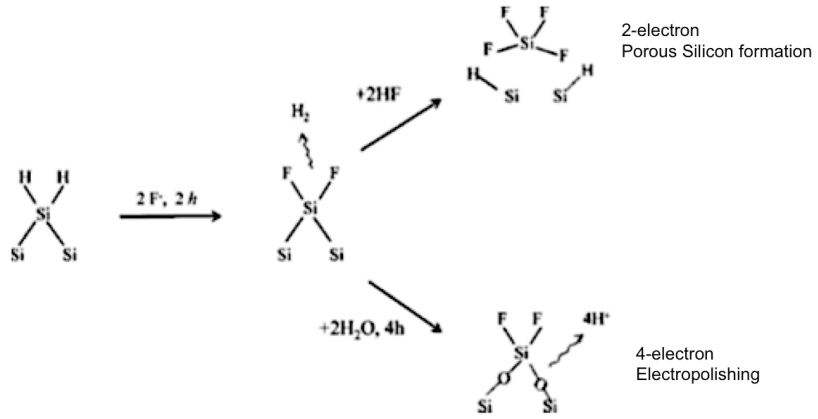

Figure 6.4. Two different reaction pathways for the dissolution mechanism of crystalline silicon in hydrofluoric acid solutions. Scheme adapted from reference [18]**.**

The dissolution of the Si atoms involves first the replacement of a surface hydrogen atom with a fluoride ion F^- with a result of a neutralized Si-F bonding. Once the Si-F bond is established another F^- ion can attack and bond generating H_2 and injecting 1 electron into the electrode. Then the silicon bonds between the silicon atoms are weak due to the high electronegativity of fluorine, so those bones can be broken by reacting with HF in a 2-electron oxidation process (**Figure 6.4**). The reaction product is SiF_4. The remaining surface silicon atoms are again hydrogenated [18].

Weak bonds between silicon atoms, once the F^- ions have been incorporated, can also be broken by H_2O. The resulting Si-O-Si bonds are not stable in HF. Si-O bonds are dissolved by F^- and Si-O are only formed when the diffusion of F^- to the silicon surface is slower than the delivery

rate of valence band holes. This is the case of the electropolishing conditions, which occurs when large current density is applied or when the concentration of HF is low.

6.3. Biocompatibility of SiO_2

Biomaterials have been a research topic in expansion for several decades. For this reason the term biocompatibility has evolved with this research. By 1970s the idea of biocompatibility was that nothing toxic could leach out of these materials. By 1980s this definition started to shift and in 1986 in a U.K conference the term biocompatibility was given a definition: "the ability of a material to perform with an appropriate host response in a specific situation" [19, 20].

Silicon dioxide have been accepted as "Generally Recognized as safe" (GRAS) by the Food and Drug Administration (FDA) [21]. Actually Silicates have been employed as dietary supplements, dental fillers, implants and contact lenses [22, 23]. The biocompatibility of SiO_2 for biomedical applications is definitely a consequence of the ability to eliminate the products of the material dissolution. Orthosilicic acid $Si(OH)_4$ is the most common soluble form of silicon acid compounds [24, 25]. Orthosilicic acid is a small molecule that is not presenting any toxicity, and this is also the usual form of silicon in the body. Some studies have demonstrated that silicon acids does not accumulate in the human body, but it is a nutrient for optimum bone health [26]. However these silicon oxides can be toxic in high doses because the precipitation of the silicate ion in the kidneys that lead to renal failure.

6.4. Optimization of Protein Loading and Release Based on Porous Silicon Particle Size and Porosity for Oral Administration.

6.4.1. Introduction

Oral administration is considered to be the most suitable and comfortable method of delivering drugs because it removes the drawbacks of frequent injections, physical stress, and troubles in handling proteins. Oral administration of proteins and peptides is limited due to their propensity to degrade in the harsh conditions present in the stomach (low pH, presence of photolytic enzymes).

Proteins and peptides have been employed as therapeutic agents for a long time. In recent times, the popularity of protein and peptide based therapeutic agents has increased due to recent advances in genomics and proteomics technology [27, 28]. However, efficient and site-specific delivery of these biological payloads is still a major challenge due to short half-lives, poor stability and immunogenicity. One of the main strategies to overcome it is loading the protein in a protective drug carrier.

Porous silicon is relevant as a drug delivery material because of its biocompatibility, biodegradability, high loading efficiency, and controllable drug release characteristic (hours to months) [29–31]. Porous silicon particles are proven to protect the sensitive cargo from degrading under areas with hostile conditions such as the stomach. Porous silicon particles are prepared by electrochemical etching of single crystal silicon wafer in hydrofluoric acid based electrolyte. This

preparation process allows precise control over the pore morphology, porosity and size of particles [12].

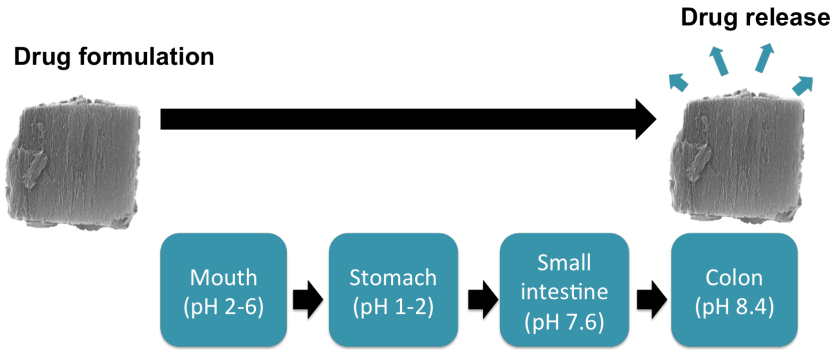

Figure 6.5. Schematics showing the pH changes that the drug will pass trough in the oral uptake.

6.4.2. Materials and Methods

The Porous Silicon (pSi) used in this study were prepared by electrochemical etch of single-crystal silicon wafers. The electrochemical method used to prepare pSi provides good control over particle size and pore size. Porous silicon particles with three different porosities and particles sizes have been prepared by changing the Hydrofluoric content of the electrolyte and the etching time detailed in **Table 6.2** in a perforation etch. A perforation etch consists of a low current etching with a periodic high current pulse resulting on porous film spaced by high porosity layers corresponding to the high current pulse [32]. This perforated layers lead to particles of controlled size due to the ultrasonic fracture of the porous silicon film by the high porosity area. Then, the duration of the normal etch will control the particle size.

Table 6.2. Summary of the electrolyte and etch conditions to obtain particles with desired pore diameter and particle size.

Sample name	Electrolyte (HF:EtOH, (v:v)	Current density for etching (mA/cm^2)	Current density for perforation (mA/cm^2)	Duration of etch (seconds)	Duration of perforation (seconds)	Repeats
A	3:1	50	200	1,85	0,315	500
B				20		50
C				50		10
D	3:2	80	300	7,2	0,5	50
E				72		10
F				180		5
G	1:1	50	200	10	0,5	50
H				100		10
I				240		5

Once the etching of the silicon porous layers have been performed different sonication times have been used for every particle size in order to break the films by the high porosity areas. Then the physical size and the distribution of sizes of the particles were determined by dynamic light scattering (DLS) for the small particles (500nm) and microscopic images for particles between 2-10μm.

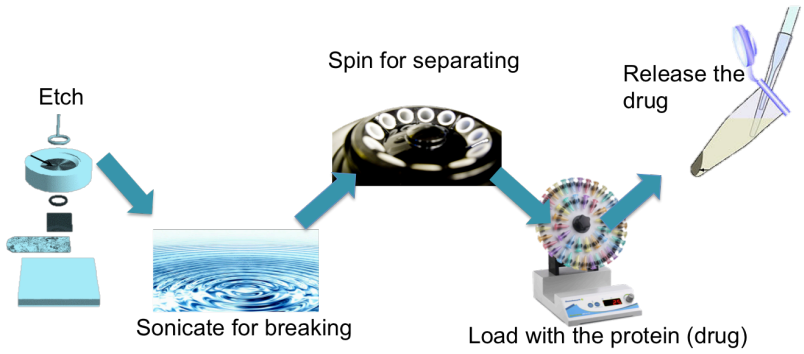

Figure 6.6. Scheme showing the steps for the experimental procedure followed.

To improve biocompatibility and protein loading the particles were oxidized by immersion in Tris Buffer Solution (TBS) for 30 minutes. Lysozyme (14KDa, isoelectric point = pH11) was selected as a test protein for this study. Lysozyme loading was performed onto pSi particles already sized by overnight incubation using TBS as the loading medium and setting them in a tube rotator (**Figure 6.6**).

The Lysozyme release was performed by exposing the loaded particles to harsh conditions such as Gastric fluid for the first 2 hours and PBS from the third hour up to 24 hours. All the experiments were performed by triplicate.

6.4.3. Results and Conclusions

Particle sizes and porosities desired (**table 6.3**) were successfully achieved using parameters in **table 6.2**.

Table 6.3. Summary of porosities and particles sizes values corresponding to every particle type.

Sample Name	Porosity	Particle Size
A	35%	500 nm
B		2 μm
C		10 μm
D	40%	500 nm
E		2 μm
F		10 μm
G	45%	500 nm
H		2 μm
I		10 μm

Release solutions were processed using a Micro BCA protein Assay Kit for the colorimetric detection and quantification of total protein. The resulting colourful solutions were read by absorbance. A calibration curve was also performed in order to relate known concentrations of Lysozyme protein and the absorbance value.

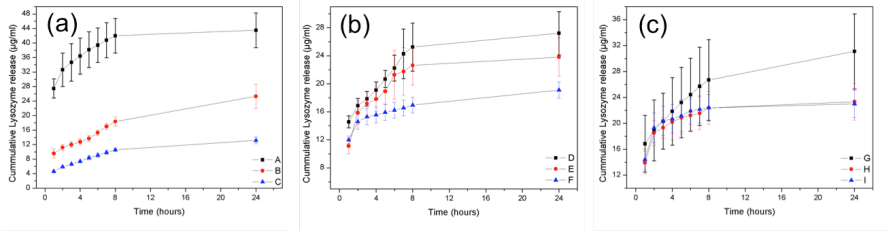

Figure 6.7. Graphs showing the release profile for every particle typology. A) Graph showing the lysozyme release for samples A,B and C. B) Graph showing release from samples D,E and F. C) Graph showing Lysozyme release from G,H and I.

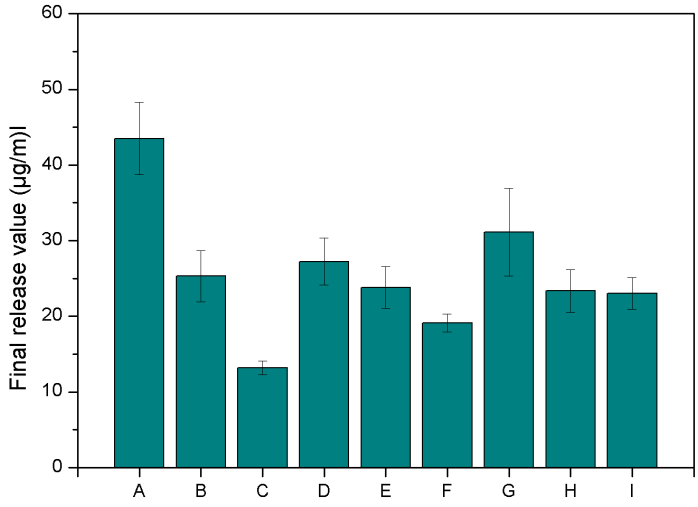

Figure 6.8. Graph showing the final release value for every particle type.

Particle sizes were successfully achieved and characterized by DLS and SEM. Results show differences between both porosities and particle sizes. In all cases small particles are able to carry and release more protein than the bigger ones. This phenomenon can be explained because

the smaller particles present more surface to absorve-desorve the protein. There are not very large differences regarding the porosity, even though bigger differences between particle sizes can be observed at lower porosities.

6.5. Sol-gel Hollow Mesoporous Nanoparticles for Drug Delivery

6.5.1. Introduction

In the past decade, mesoporous silica nanoparticles (MSNs) have attracted a lot of interest due to their excellent properties including high surface areas, large pore volumes, tuneable pore sizes and good biocompatibility [33–36].

Nowadays MSN are considered ideal drug delivery candidates because they could effectively deliver drugs to targeted sites in a controlled manner [37]. Compared with conventional MSN, hollow MSN (HMSN) exhibit unique advantages in mass diffusion and transportation thanks to their carrying capacity and mesoporous shell [38, 39]. In addition it has been reported that particles about 300 nm are retained inside tumoral tissue due to enhanced permeability and retention (EPR) effect. The aim of this study is to create hollow mesoporous silica nanoparticles (HMSNs) about 300 nm of diameter.

6.5.2. Materials and Methods

All the chemical reagents used in the experiments were obtained from commercial sources as guaranteed-grade reagents and used without further purification. Tetradecyltrimethyl-ammonium bromide (TTAB) (99%), triethanolamine (TEA) (99%) and tetraethoxysilane

(TEOS) (99%). TTAB was used as the structure-directing agent (SDA). Firstly 1.92g of TEOS and 14.3g of TEA were firstly mixed and heated in a sand bath at 90ºC for 1h under stirring conditions, it was named solution A. At the same time 0.7384g of TTAB was added into 21.7mL of distilled water by ultrasonication for 30 minutes at room temperature named as solution B. Subsequently, the solution B was rapidly added into the solution A. Then the mixture was stirred for 3h at room temperature. Afterwards, the products were collected by centrifugation, washed with water and ethanol several times, and dried overnight at 120ºC. Finally the TTAB and other organic components were removed by calcination in air at 550ºC for 5h to obtain the HMSNs.

6.5.3. Results and Conclusions

Hollow mesoporous nanoparticles formation has been achieved. Due to nanoparticles measurements using Transmission Electron Microscopy (TEM) imaging we are able to confirm that the diameter of the particles is about 300 nm.

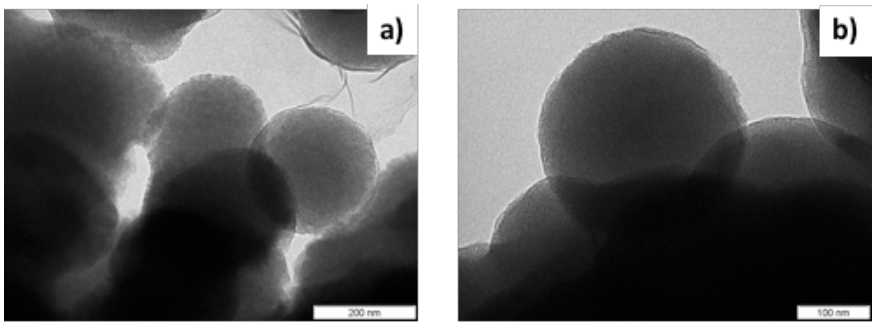

Figure 6.9. TEM images from hollow nanoparticles obtained by sol-gel procedure.

6.6. Summary

In this Chapter the history of nanoporous anodic alumina has been described. In addition an extensive silicon porous formation has been explained. Biocompatibility of Silicon dioxide has been treated. Optimization of protein loading on different porosities and sizes porous silicon particles has been also exposed with the conclusions already mentioned. Sol-gel hollow mesoporous hollow particles have also been achieved

6.7. References

1. Uhlir A (1956) Electrolytic Shaping of Germanium and Silicon. Bell Syst Tech J 35:333–347. doi: 10.1002/j.1538-7305.1956.tb02385.x
2. Gupta P, Dillon AC, Bracker AS, George SM (1991) FTIR studies of l-I , 0 and I & O decomposition silicon surfaces. Surf Sci 245:360–372.
3. Dillon AC, Robinson MB, Han MY, George SM (1992) Diethylsilane Decomposition on Silicon Surfaces Studied Using Transmission FTIR Spectroscopy. J Electrochem Soc 139:537–543.
4. Imai K (1981) A NEW DIELECTRIC ISOLATION METHOD USING POROUS SILICON. Solid State Electron 24:4–9.
5. Anderson RC, Muller RS, Tobias CW (1990) Investigations of Porous Silicon for Vapor Sensing. Sensors and Actuators 23:835–839.

6. Lehmann V, Gösele U (2013) Porous silicon formation : A quantum wire effect Porous silicon formation : A quantum. Appl Phys Lett. doi: 10.1063/1.104512
7. Canham LT (1990) Silicon quantum wire array fabrication by electrochemical and chemical dissolution of wafers Silicon quantum wire array fabrication by electrochemical and chemical dissolution of wafers. Appl Phys Lett 57:1046–1048. doi: 10.1063/1.103561
8. Lin VS, Lin VS, Motesharei K, et al. (1997) A Porous Silicon-Based Optical Interferometric Biosensor. Science (80-) 278:840–843. doi: 10.1126/science.278.5339.840
9. Arrand HF, Benson TM, Sewell P, et al. (1998) The Application of Porous Silicon to Optical Waveguiding Technology. IEEE J 4:975–982.
10. Coffer JL, Whitehead MA, Nagesha DK, et al. (2005) Porous silicon-based scaffolds for tissue engineering and other biomedical applications. Phys Status Solidi 1455:1451–1455. doi: 10.1002/pssa.200461134
11. Letant SE, Content S, Tan TT, et al. (2000) Integration of porous silicon chips in an electronic artificial nose. Sensors and Actuators 69:193–198.
12. Sailor MJ (2012) Porous Silicon in Practice: preparation, characterization and applications. John Wiley & Sons
13. Taylor P, Korotcenkov G, Cho BK, et al. (2010) Porosification : State of the Art. Crit Rev Solid State Mater Sci Silicon 35:153–260. doi: 10.1080/10408436.2010.495446

14. Zhang XG, Soc JE (1991) Mechanism of Pore Formation on n – Type Silicon Mechanism of Pore Formation on n-Type Silicon. J Electrochem Soc 138:3750–3756. doi: 10.1149/1.2085494
15. Corbett J w., Shereshevskii DI, Verner I V. (1995) Changes in the Creation of Point Defects Related to the Formation of Porous Silicon. Phisica Status Solidi 147:81–89.
16. Rouquerol J, Avnir D, Everett DH, et al. (1994) Guidelines for the Characterization of Porous Solids. Stud Surf Sci Catal 87:1–9.
17. Chabal YJ, Higashi GS, Raghavachari K, Burrows VA (1989) Infrared spectroscopy of Si (111) and Si (100) surfaces after HF treatment : Hydrogen termination and surface morphology. J Vac Sci Technol A 7:2104–2109. doi: 10.1116/1.575980
18. Zhang XG, Soc JE, C-c P, Zhang XG (2004) Morphology and Formation Mechanisms of Porous Silicon service. J Electrochem Soc 151:69–80. doi: 10.1149/1.1632477
19. Mertz BL (2013) What Is Biocompatibility IEEE Pulse 14–15.
20. Williams DF (1989) A model for biocompatibility. J Biomed Eng 11:185–191.
21. Select Committee on GRAS Substances (SCOGS) Opinion : Silicates. Food Drug Adm 3–5.
22. Dyck K Van, Cauwenbergh R Van, Robberecht H, Deelstra H (1999) Bioavailability of silicon from food and food supplements. Fresenius J 363:541–544.
23. Braley S (1970) The Chemistry and Properties of the Medical-Grade Silicones. J Macromol Sci Part A - Chem Pure Appl Chem 4:529–544.

24. Chiappini C, Tasciotti E, Fakhoury JR, et al. (2011) Tailored porous silicon microparticles: fabrication and properties. ChemPhisChem 11:1029–1035. doi: 10.1002/cphc.200900914.Tailored
25. Anderson SHC, Elliott H, Wallis DJ, et al. (2003) Dissolution of different forms of partially porous silicon wafers under simulated physiological conditions. Phisica Status Solidi 335:331–335.
26. Henstock JR, Canham LT, Anderson SI (2014) Silicon: the evolution of its use in biomaterials. ACTA Biomater 11:17–26. doi: 10.1016/j.actbio.2014.09.025
27. Lu Y, Yang J, Sega E (2006) Issues Related to Targeted Delivery of Proteins and Peptides. AAPS J 8:466–478.
28. Pisal DS, Kosloski MP, Balu-Iyer S V. (2011) DELIVERY OF THERAPEUTIC PROTEINS. J Pharm Sci 99:2557–2575. doi: 10.1002/jps.22054.DELIVERY
29. Wu C, Hu Y, Miller M, et al. (2015) Protection and Delivery of Anthelmintic Protein Cry5B to Nematodes Using Mesoporous Silicon Particles. ACS Nano 9:6158–6167.
30. Andrew JS, Wu EC, Chen MY (2010) Sustained Release of a Monoclonal Antibody from Electrochemically Prepared Mesoporous Silicon Oxide. Adv Funct Mater 20:4168–4174. doi: 10.1002/adfm.201000907.Sustained
31. Schwartz MP, Yu C, Alvarez SD, et al. (2007) Using an oxidized porous silicon interferometer for determination of relative protein binding affinity through non-covalent capture probe immobilization. Phisica Status Solidi 204:1444–1448. doi: 10.1002/pssa.200674380

32. Qin Z, Joo J, Gu L, Sailor MJ (2014) Size Control of Porous Silicon Nanoparticles by Electrochemical Perforation Etching. Part Part Syst Charact 31:252–256. doi: 10.1002/ppsc.201300244
33. Slowing II, Trewyn BG, Lin VS (2007) Mesoporous Silica Nanoparticles for Intracellular Delivery of Membrane-Impermeable Proteins. J Am Chem Soc 8845–8849.
34. Liu J, Jiang X, Ashley C, Brinker CJ (2009) Electrostatically Mediated Liposome Fusion and Lipid Exchange with a Nanoparticle-Supported Bilayer for Control of Surface Charge , Drug Containment , and Delivery. JAm Chem Soc Comun 131:7567–7569.
35. Andersson J, Rosenholm J, Areva S, Lindén M (2004) Influences of material characteristics on ibuprofen drug loading and release profiles from ordered micro- and mesoporous silica matrices. Chem Mater 16:4160–4167. doi: 10.1021/cm0401490
36. Liu J, Stace-naughton A, Jiang X, Brinker CJ (2009) Porous Nanoparticle Supported Lipid Bilayers (Protocells) as Delivery Vehicles. JAm Chem Soc Comun 131:1354–1355.
37. Xu L, He J (2012) Antifogging and Antire fl ection Coatings Fabricated by Integrating Solid and Mesoporous Silica Nanoparticles without Any Post- Treatments. Appl Mater Interfaces 4:3293–3299.
38. Carta D, Casula MF, Bullita S, et al. (2014) Direct sol – gel synthesis of doped cubic mesoporous SBA-16 monoliths. MICROPOROUS MESOPOROUS Mater 194:157–166. doi: 10.1016/j.micromeso.2014.03.032

39. Li P, Cao C, Chen Z, et al. (2012) Core – shell structured mesoporous silica as acid – base bifunctional catalyst with designated diffusion path for cascade reaction sequences w. Chem Commun (Camb) 48:10541–10543. doi: 10.1039/c2cc35718f

UNIVERSITAT ROVIRA I VIRGILI
DEVELOPMENT OF NANOPOROUS ANODIC ALUMINA TECHNOLOGIES FOR DRUG DELIVERY
Maria Porta Batalla

Chapter 7

Summary and Conclusions

UNIVERSITAT ROVIRA I VIRGILI
DEVELOPMENT OF NANOPOROUS ANODIC ALUMINA TECHNOLOGIES FOR DRUG DELIVERY
Maria Porta Batalla

In this Ph.D. thesis it has been presented the possibility to use Nanostructured semiconductors like aluminium oxide or silicon as a nanostructured material for the development of drug delivery systems.

Chapter 2 is presenting fundamentals for Nanoporous Anodic Alumina passing through history, basis of nanoporous anodic alumina formation and the anodizing parameters.

Chapter 3 has presented the set up for NAA fabrication. Several techniques have been discussed such as two-step anodization using different electrolites. The calibration curves for the precise manufacture of NAA layer thickness and pore widening in phosphoric acid were shown. Finally characterization has been presented showing the basic effects of structural parameters such as thickness and porosity.

Chapter 4 has shown all the work made with NAA covered with Layer-by-layer polyelectrolyte with pH stimuli-responsive features. After a brief introduction of the state of the art, the methodology for the NAA fabrication and layer-by-layer polyelectrolyte deposition is presented. Moreover pore sizes are presented and samples characterized. Drug release measurements were taken for different pH release medium, showing pH-dependent differenecies. Fittings for these release curves are presented showing quantitative analysis according to mathematical models. The conclusions from this analysis showed that the release dynamics strongly depends on the pH of the medium. Moreover if an abrupt change in pH is applied from neutral to acidic medium a second burst release is trigged. This Nanoporous Anodic Alumina coated with

layer-by-layer polyelectrolyte has potential applications as a drug delivery device.

In chapter 5 an innovative NAA is presented as a controlled drug release system. Funnel-like structure and inverted funnel-like structures were obtained using the two-step anodization technique and they were compared with regular pores. This study takes profit of the differences on pore widening rates after temperature treatment of the NAA to create the different structures. With this technology the purpose of the study was to find the best structure for drug release. The quantitative dynamics of the release has been studied using two different regimes: a bust release and a late release. The release dynamics have been fitted using mathematical models in order to compare them objectively. As a conclusion we found a linear relation between the top pore diameters in the case of regular pores. In the case of the funnels the release rate are pore-volume dependant.

Chapter 6 introduces Silicon technology for drug delivery systems. Fundamentals for Porous Silicon Nanotechnology have been presented for both electrochemical etching and sol-gel methodology. Particles using both methods were achieved and characterized. Finally, particles of different size and porosity were used for engineering a drug delivery system for the colon administration, using a protein as a drug that should be protected from the harmful gastrointestinal environment. As conclusions smaller particles are able to carry and release higher amounts of protein compared to the bigger ones, due to the enhanced surface to absorb and desorb the protein.

All the data presented in this work has the potential to develop drug delivery devices. By appropriately applying the suggestions arising from the results presented, long, controlled and stimuli-responsive drug release can be achieved. However this work just focused on the drug release of the drugs using model drugs in order to perform prove of concept. The methods herein presented open the door for the improvement of a sort of drug delivery systems. Altogether, technology, characterization and applications presented in this thesis are rather encouraging and will provide a starting point for developing innovative smart systems that will find application in the industry.

UNIVERSITAT ROVIRA I VIRGILI
DEVELOPMENT OF NANOPOROUS ANODIC ALUMINA TECHNOLOGIES FOR DRUG DELIVERY
Maria Porta Batalla

UNIVERSITAT ROVIRA I VIRGILI
DEVELOPMENT OF NANOPOROUS ANODIC ALUMINA TECHNOLOGIES FOR DRUG DELIVERY
Maria Porta Batalla

UNIVERSITAT ROVIRA I VIRGILI
DEVELOPMENT OF NANOPOROUS ANODIC ALUMINA TECHNOLOGIES FOR DRUG DELIVERY
Maria Porta Batalla

UNIVERSITAT ROVIRA I VIRGILI
DEVELOPMENT OF NANOPOROUS ANODIC ALUMINA TECHNOLOGIES FOR DRUG DELIVERY
Maria Porta Batalla

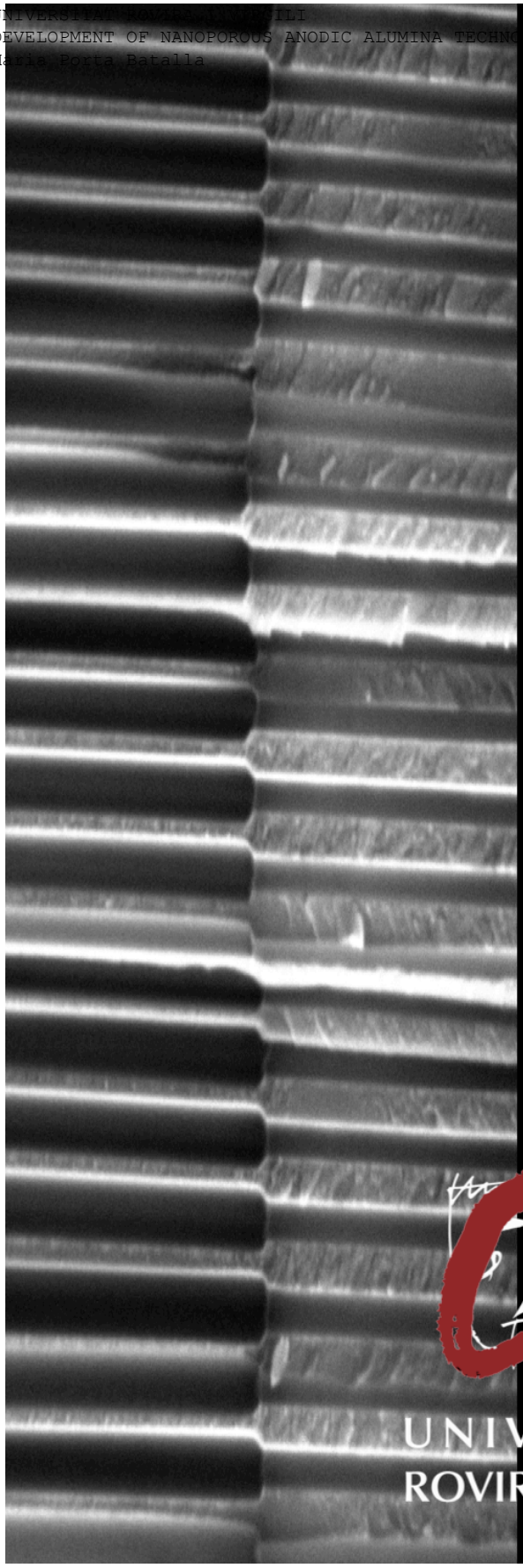

UNIVERSITAT
ROVIRA i VIRGILI